

**UCLA**

**UCLA Electronic Theses and Dissertations**

**Title**

Synthesis and Derivatization of Stimuli Responsive Mesoporous Silica Nanoparticles and Biomedical Drug Delivery Application

**Permalink**

<https://escholarship.org/uc/item/3nk5h85w>

**Author**

Li, Zilu

**Publication Date**

2015

Peer reviewed|Thesis/dissertation

UNIVERSITY OF CALIFORNIA

Los Angeles

Synthesis and Derivatization of Stimuli Responsive Mesoporous Silica Nanoparticles  
and Biomedical Drug Delivery Applications

A dissertation submitted in partial satisfaction of  
the requirement for the degree Doctor of  
Philosophy in Materials Science and Engineering

By

Zilu Li

2015



## ABSTRACT OF THE DISSERTATION

### Synthesis and Derivatization of Stimuli Responsive Mesoporous Silica Nanoparticles and Biomedical Drug Delivery Applications

By

Zilu Li

Doctor of Philosophy in Materials Science and Engineering

University of California, Los Angeles, 2015

Professor Bruce S. Dunn, Chair

This thesis involves synthesis, derivatization and biomedical applications of mesoporous silica nanoparticles (MSNs) and  $\text{Fe}_3\text{O}_4@\text{SiO}_2$  core/shell nanoparticles. Chapter 1 introduces the development of MSNs including the mesopore formation mechanism, synthesis conditions and their capability to act as stimuli responsive drug delivery platforms. In chapter 2, the synthesis optimization of different kinds of particles and their surface derivatization are introduced. Chapters 3 & 4 give specific examples of successful optimization and *in vitro* and *in vivo* applications of MSNs derivatized with pH-sensitive nanovalves and disulfide snap-tops for delivering the antibiotic moxifloxacin. It is shown that a high release capacity is necessary to reach a

high efficacy ratio compared with free drug. Chapter 5 discusses the uptake and release capacities of  $\text{Fe}_3\text{O}_4@\text{SiO}_2$  core/shell nanoparticles when modified with pH-sensitive nanovalves, and its thermally stimulated cargo release behavior when the surrounding temperature increases or an oscillating magnetic field is applied. In Chapter 6, successful distribution of  $\text{Fe}_3\text{O}_4@\text{SiO}_2$  core/shell nanoparticles in biofilms and on-command release of cargo inside biofilms are shown. Overall, these chapters demonstrate the successful modification of both the outer and interior pore surfaces of MSNs, and their capability to act as biocompatible controlled release platforms that are more effective in killing pathogens than an equivalent amount of free drug.

The dissertation of Zilu Li is approved.

Jeffrey I. Zink

Yu Huang

Bruce S. Dunn, Committee Chair

University of California, Los Angeles

2015

## TABLE OF CONTENTS

ACKNOWLEDGEMENTS	viii
VITA	x
<b>Chapter 1 Mesoporous Silica Nanoparticles (MSNs) as Drug Delivery Vehicles</b>	
1.1 Introduction	2
1.2 Figures	10
1.3 References	12
<b>Chapter 2 Synthesis, Characterization and Derivatization of Nanoparticle for theranostics</b>	
2.1 Introduction	17
2.2 Experimental Section	26
2.3 Figures	34
2.4 References	47
<b>Chapter 3 Mesoporous Silica Nanoparticles with pH–Sensitive Nanovalves for Delivery of Moxifloxacin Provide Improved Treatment of Lethal Pneumonic Tularemia</b>	
3.1 Abstract	51
3.2 Introduction	51
3.3 Results and Discussion	54
3.4 Conclusions	69
3.5 Experimental Section	70
3.6 Figures and Tables	77

3.7 References	90
----------------	----

**Chapter 4 Redox-Triggered Release of Moxifloxacin from Mesoporous Silica Nanoparticles Functionalized with Disulfide Snap-Tops Enhances Efficacy Against Pneumonic Tularemia in Mice**

4.1 Abstract	97
4.2 Introduction	98
4.3 Results and Discussion	101
4.4 Conclusions	113
4.5 Experimental Section	117
4.6 Figures and Tables	124
4.7 References	138

**Chapter 5 Measurement of Uptake and Release Capacities of Fe<sub>3</sub>O<sub>4</sub>@SiO<sub>2</sub> Mesoporous Silica Nanoparticles Modified with pH-Sensitive Nanovalve and its thermally triggered release test**

5.1 Abstract	149
5.2 Introduction	149
5.3 Results and Discussion	151
5.4 Conclusions	158
5.5 Experimental Section	159
5.6 Figures and Tables	164
5.7 References	171

**Chapter 6 Application of Fe<sub>3</sub>O<sub>4</sub>@SiO<sub>2</sub> Mesoporous Silica Nanoparticles in Drug**



## **Delivery to Biofilms**

6.1 Abstract	175
6.2 Introduction	175
6.3 Results and Discussion	177
6.4 Conclusions	181
6.5 Experimental Section	182
6.6 Figures	186
6.7 References	192

## ACKNOWLEDGEMENTS

It is impossible to complete my doctoral degree without many people's help. First I would like to acknowledge my advisor, Professor Jeffrey I. Zink. I want to thank him for offering me the opportunity to learn and study in a world-class lab at UCLA, helping me build up a scientific thinking style when dealing with all kinds with difficulties, and giving me the kind guidance on publishing and presenting research results. In his group I also learnt how to collaborate with excellent researchers from all over the world with various backgrounds. He is not only an amazing scientist who kindly discusses with his students and patiently explains his ideas, but also a considerate mentor who cares about the future development of his students. I also would like to thank Professor Bruce S. Dunn for being my advisor in the department of Materials Science and Engineering and giving me suggestions on being a Ph.D. candidate. I would like to thank Professor Yang Yang and Professor Yu Huang for serving on my dissertation committee.

Next I would like to thank my colleagues and friends in the Zink group. I would like to thank Dr. Courtney R. Thomas for instructing me on the first project and teaching me synthesis skills when I firstly joined the group. I would like to thank Dr. Min Xue and Dr. Derrick Tarn for helping and training me on various experimental instruments, and most importantly their hardworking and scientific rigorous attitudes toward research significantly affected me through my whole Ph.D. life. I would like to thank Dr. Angela Hwang, Dr. Yen-Ting (Janie) Chen, Dr. Juyao (Ivy) Dong, Dr. Philippe Saint-Cricq Riviere, Dr. Bastian Rühle, and Dr. Wen-Yen Huang for giving

me lots of meaningful suggestions and spending their time discussing with my about projects and research problems. I appreciate their efforts in setting up, developing and maintaining the group equipments, from which I also learnt a lot. I also would like to thank Ruining Wang, Chia-Jung Yu, Sheba Plamthottam and Daniel Pazo for being good colleagues and friends over my Ph.D. life.

I would like to acknowledge our generous collaborators Professor Marcus Horwitz, Dr. Daniel Clemens and Dr. Bai-Yu Lee, without whom the research results involving infectious disease wouldn't be complete and successful. Moreover, I gained a lot experience on presentation and scientific writing from working with them. I respect them as very hardworking and knowledgeable scientists. I would like to thank Professor Fuyuhiko Tamanoi and Dr. Jie Lu for their collaboration on a number of *in vitro* studies. I would like to thank Professor Dino Di Carlo, Dr. Westbrook Weaver, Dr. Coleman Murray and Keegan Owsley for their collaboration on the biofilm project. I also would like to thank Dr. Chong Hyun Chang and Dr. Zhaoxia Ji in Peofessor Andre Nel's lab for their help on using instruments such as dynamic light scattering and inductively couple plasma optical emission spectroscopy.

Last but not least, I would like to thank my family and friends who are supporting me all the time. I would like to thank Qing Zhang for accompanying me going through the whole Ph.D. life. And I also would like to thank Bo Wen, Sen Li and Song Liu for being close friends and leaving me lots of good memories after we arrived in the United States. I am very grateful for having my parents and friends and I cannot say enough thank you to them.

## VITA

2010

B.S. Chemistry

Tsinghua University

Beijing, China

2012-2013

Teaching Assistant

Department of Chemistry and Biochemistry

University of California, Los Angeles

Los Angeles, California

2012-2015

Research Assistant

Zink Research Group

## Chapter 1

### Mesoporous Silica Nanoparticle (MSNs) as Drug Delivery Vehicles

## **1.1. Introduction**

### **1.1.1. Mesoporous Silica Nanoparticles (MSNs)**

Mesoporous materials are defined as inorganic solids with pore diameters between 20 and 500 Å. Ordered mesoporous silica materials are synthesized through interaction between silica sources such as tetraethyl orthosilicate (TEOS), tetramethyl orthosilicate (TMOS), etc. and structure directing agents including cationic/anionic surfactants and polymers, in either acidic or basic media. Examples of these types of materials include MCM-41, MCM-48, SBA-15, etc. and their morphologies can be mesoporous thin films, monoliths, particles, rods and so on synthesized with different methods. By means of utilizing different surfactants, reaction pH and temperature, the mesopore size and materials morphology can be successfully tuned. For example, the pore size of SBA-15 can be tuned up to 30 nm by using triblock polymer pluronic P123.<sup>1-5</sup> We are particularly interested in MCM-41 type mesoporous silica nanoparticle (MSNs) due to their appropriate size and intrinsic properties to act as drug delivery vehicle. MCM-41 type particle possesses ordered 2D hexagonally packed mesopores about 2.2 nm diameter and high surface areas greater than 1000 m<sup>2</sup>g<sup>-1</sup>. The best-known was firstly reported by Mobil Research and Development Corporation in 1992.<sup>6, 7</sup> From then on, a lot studies have been undertaken on its physical and chemical properties, mesostructure formation mechanism, morphology and size control as well as application in drug delivery and release as nano carrier. The MCM-41 material was initially developed as catalyst and catalyst supports due to its high surface area and relative stable framework. Gradually researchers found its

great potential as therapeutics nanocarrier, because MSNs has excellent biocompatibility, nano-meter size for bio-distribution and accumulation in cancer tissues as well as high surfaces area which can be modified with various functional groups to change its surface properties, including positive/negative charges, hydrophilicity/hydrophobicity, dispersibility in different solvent media and so on. Additionally, we have developed mechanized MSNs with its surfaces functionalized with nanomachines, and in this way we realized the idea of applying MSNs as anticancer/antibiotics nano carrier and on-demand controlled release system to the pathological sites and release drugs upon specific internal stimuli, such as pH, reducing chemicals, enzymes, or external stimuli including light, magnetic field etc.<sup>8</sup>

### **1.1.2. Mesostructure formation mechanism**

Silica source can be inorganic silicate (fumed silica, sodium silicate) or organosilane (TMOS, TEOS) and the latter one was utilized in the synthesis of mesoporous silica nanoparticles. We used the cationic surfactant alkyltrimethylammonium halide (cetyltrimethylammonium bromide (CTAB)) as structure directing agent, and sodium hydroxide as catalyst. When Mobil researchers first reported the synthesis and characteristic of MCM-41, they proposed the mechanism as “liquid crystal templating”. The mesostructure is dependent on the concentration of surfactant and the length of its hydrophobic group. Two possible pathways were suggested as shown in Figure 1.<sup>9</sup> In the first pathway hexagonal lyotropic liquid crystals formed first and then silicate would condense around them, while in the second pathway 2-D hexagonal structure is affected by silicate precursor.

Pathway 2 is understood as cooperative self-assembly process to form the mesostructure, which is mediated by the silicate species. The main difference between these two pathways is whether or not addition of the silicon precursor has influence on the formation of hexagonally packed micelle arrays.

In 1995, A. Firouzi et al. proposed the idea of “silicatropic liquid crystal” mechanism, and they showed that organic molecules self-assemble themselves into silicatropic liquid crystals in the presence of multiply charged silicate oligomers.<sup>10</sup> The formation of silicatropic liquid crystals happened when the surfactant concentration was much lower than CMC. Figure 2. shows the silicatropic liquid crystal formation process. There is ion exchange between surfactant and silica sources and D4R (double four-ring,  $[\text{Si}_8\text{O}_{20}]^{8-}$ ) silicate anions preferentially interact with positively charged ammonium head group of the surfactant. Another reason for this cooperative organization is that the D4R anions and ammonium cations have similar projected area.

In addition, Firouzi et al. also investigated the silicate-surfactant mesophase by means of X-ray diffraction, which supported the cooperative self-assembly mechanism. They made use of neutron scattering and the results showed that the surfactant in solution firstly formed isotropic spherical or cylindrical micelles. Ordered inorganic-organic hexagonal structure formed upon addition of a silica source, which was revealed by XRD with a narrow scattering pattern. They also showed the influence of reactant concentrations on the morphology of final silica materials.



Electrostatic interaction is also playing an important role in the silicatropic liquid crystal formation process. The silica precursor is usually assigned as I and surfactant assigned as S. The known isoelectric point of silica is  $\text{pH} \approx 2$ , so the interaction between silicate and surfactant in pathway 2 can be represented in the form of  $\text{S}^+\text{I}^-$  complex. Moreover, if the reaction takes place in acidic solution, there will be a positively charged silica  $\text{I}^+$  and negatively charged halide counteranion  $\text{X}^-$  as  $\text{S}^+\text{X}^-\text{I}^+$  system. Moreover, positively charged metal ions can be introduced as  $\text{S}^-\text{M}^+\text{I}^-$  to synthesize doped M41S mesoporous materials.

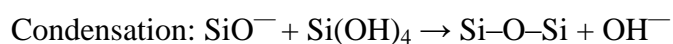
### **1.1.3. Synthesis of Mesoporous Silica Nanoparticles (MSNs)**

Due to the isoelectric point of silica at pH 2, the hydrolysis and condensation pH can be divided into three regions:  $\text{pH} < 2$ ,  $2 < \text{pH} < 7$  and  $\text{pH} > 7$ . In terms of SBA-15 with ordered pores up to 30 nm, the big pore formation only happens at pH 1-2. In acid-catalyzed hydrolysis, the alkoxide group is protonated and becomes electrophilic which is attacked by a water molecule. A transition state formed and a hydroxyl group is attached to the silicon by inversion of the silicon tetrahedron. In acid-catalyzed condensation, a protonated silanol group becomes electrophilic and is attacked by a silicate. At pH 2-7 there is no silica gel formed or amorphous silica. When  $\text{pH} > 7$ , the solubility of silicate and condensation rate is higher than that in acidic solution. Particle can grow to hundreds of nanometers dependent on the temperature.

The synthesis of mesoporous silica nanoparticles (MSNs) is based on interaction between surfactant and silica source through sol-gel process in basic water-ethanol solution. In base-catalyzed hydrolysis, hydroxyl anion attacks the silicon and replaces

the OR group by inversion of the silicon tetrahedron. In base-catalyzed condensation, a nucleophilic deprotonated silanol group attacks a neutral silicate as shown.<sup>11</sup>

In Base:



In 1997, Grün et al.<sup>12</sup> came up with the method of synthesizing micrometer- and submicrometer- size spheres of ordered mesoporous oxide MCM-41, modified from Stöber's synthesis method.<sup>13</sup> The reaction took place in ammonium hydroxide water/ethanol solution at room temperature. And in 2001, Cai. et al.<sup>14</sup> synthesized 110 nm diameter MSNs using low concentration of CTAB in sodium hydroxide solution, proposing that self-assembly silicate micelles in strong base solution facilitate the formation of nanospheres. In 2004, Suzuki et al. synthesized MSNs with diameters of 20-50 nm using a double surfactant system.<sup>15</sup>

In a typical synthesis of MCM-41 type MSNs that were synthesized and used for the research I this thesis, tetraethylorthosilicate (TEOS) was employed as silica precursor and added to heated sodium hydroxide aqueous solution as catalyst, containing cetyltrimethylammonium bromide (CTAB) surfactant template as structure directing agent. After hydrolysis and condensation in the sol-gel process, the MSNs formed in the aqueous solution and aged for two hours. The surfactant CTAB was extracted by refluxing particles in acidic methanol/ethanol solution or ammonium nitrate methanol/ethanol solution by making use of ion exchange. The particle morphology, 2D hexagonal mesopores structure, pore size, and surface area were

characterized by Transmission Electron Microscopy (TEM), X-ray diffraction (XRD) and N<sub>2</sub> absorption/desorption measurement.

#### **1.1.4. Controlled Release System and Biological Application**

As shown in Figure 3, MSNs can be modified with various materials and methods to realize different functionalities: 1. The inner space can be embedded with magnetic nanocrystals to induce hyperthermia and magnetic resonance imaging;<sup>16</sup> 2. The particle surface can be conjugated with fluorescent molecule for *in vitro* and *in vivo* fluorescence imaging; 3. Polymers (PEI/PEG)<sup>17</sup> or lipid bilayers are coated surrounding the MSNs to decrease the particle aggregation and improve their stability in solutions; 4. Nanomachines are developed to trap the cargo inside the pores and open only upon certain stimuli; 5. Targeting ligands are attached on the particle surface to selectively bind to the receptor on the cell membrane, which is overexpressed in cancer tissues.<sup>18</sup>

To apply MSNs as an effective delivery and release system, we need to consider not only the nano-carrier, but also the properties and structures of cargo molecules. In terms of the drug molecules, they can be generally divided into two categories: hydrophilic and hydrophobic. Successful MSNs bio-applications as a delivery system for hydrophobic anticancer drugs have been reported.<sup>19</sup> Some important anticancer drugs have very low solubility in aqueous media and cannot be effectively administered through the intravenous route. Loading hydrophobic molecules is relatively straightforward and does not need a complex trap system because the drug solubility in aqueous media is so low that they barely escape from the MSNs when

administered through the intravenous route *in vivo*. And the drugs will be released in hydrophobic regions of the cell compartment as proved by *in vitro* study. Incorporation of hydrophobic drugs into MSNs overcomes the solubility and dispensability issue and improves the effective concentration in pathological sites. Therefore MSNs have advantageous pore structures and chemical properties to load and release hydrophobic drugs.

In term of the delivering hydrophilic drugs, we need to employ a “nanomachine” system to trap the cargo inside mesopores to prevent pre-mature release, which are specified as “nanovlave” and “snap-top” described in chapter 3 and 4. The nanomachine can open at target sites upon external or internal stimulation, including pH, reducing chemical, light, external oscillating magnetic field etc.<sup>16, 20-22</sup> When assembling the nanomachnies onto MSNs, the surfaces are derivatized with organic stalks, and after loading the cargo a bulky cyclic molecule is used as a cap to encircle the stalk through hydrophobic-hydrophobic interaction. Upon the internal or external stimuli, there will be stalk conformational change, which leads to decrease of its binding affinity with the cap. Besides, we can also modify the inner mesopores of MSNs and one example is the “nanoimpeller” design. An azobenzene molecule exhibits trans-cis isomerization upon activation by specific wavelength light. This conformational movement helps impel the cargo out of the mesopores.

Besides the superiority of storing and release of drugs, MSNs also show biocompatibility and effective uptake by cells. There is no cytotoxicity observed for 100 nm MSNs when the concentration is lower than 100  $\mu\text{g/mL}$ . MSNs have been

widely applied as anti-cancer drug delivery systems due to an important property: enhanced permeability and retention (EPR) effect. It was first discovered by Yasuhiro Matsumura and Hiroshi Maeda<sup>23</sup> in 1986. They found that macromolecules accumulate much more in tumor tissues than other normal tissues. This is due to the special structure of tumor cell system, which has leaky vasculature and lacks effective lymphatics drainage. The endothelial cells of blood vessel walls are poorly aligned with fenestrations or gaps among cells, which help enhance the retention of nanocarriers among tumor cells as well as extravasate endothelial cell boundaries. At the same time, surrounding healthy cells are not affected. Nanocarriers will have long circulation time and blood half-life due to EPR effect. Moreover, the particles are taken up by cells through endocytosis, in which the particles are engulfed by the cell membrane and formed the endosomes. When the endosomes fuse with acidic lysosomes, the particles end up staying in acid environment (pH ~4.5). Some anticancer therapeutics such as doxorubicin (DOX) are cell membrane permeable and thus will not be blocked by the endosome when release in its acidic compartment. Nevertheless, endosome escape is required when loading membrane impermeable therapeutics such as hydrophilic drugs, DNA etc. And several methods have been proposed to facilitate endosome escape, such as surface modification with groups that can be protonated such as amines (“proton sponge effect”), using photosensitizer to generate reactive oxygen species to rupture and so on.<sup>24</sup>

## 1.2. Figures

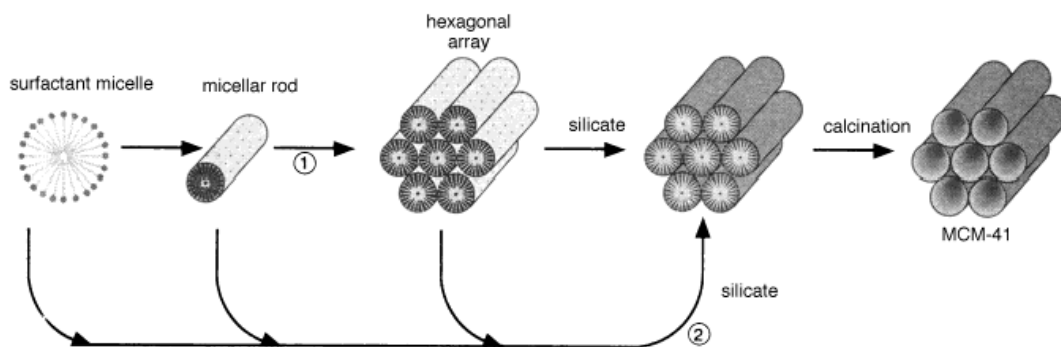


Figure 1. Two pathways of mesostructure formation<sup>9</sup>

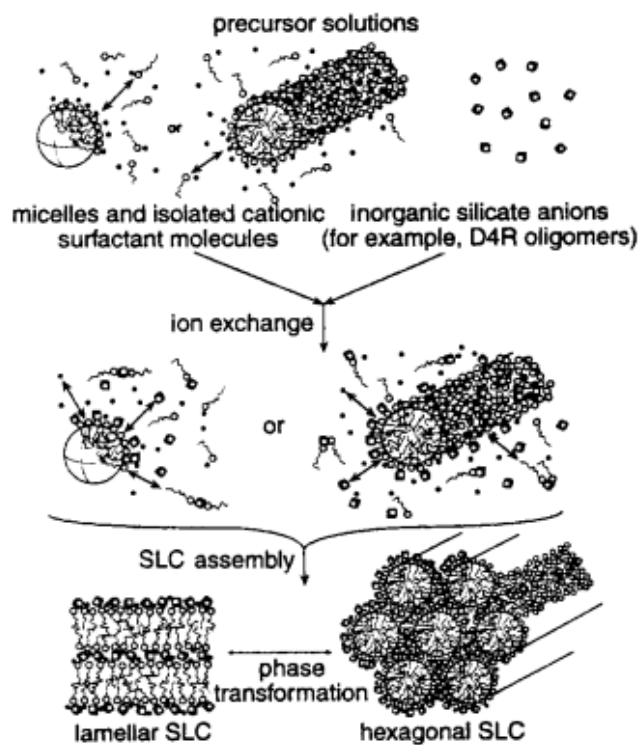


Figure 2. Silicatropic liquid crystal mechanism<sup>10</sup>

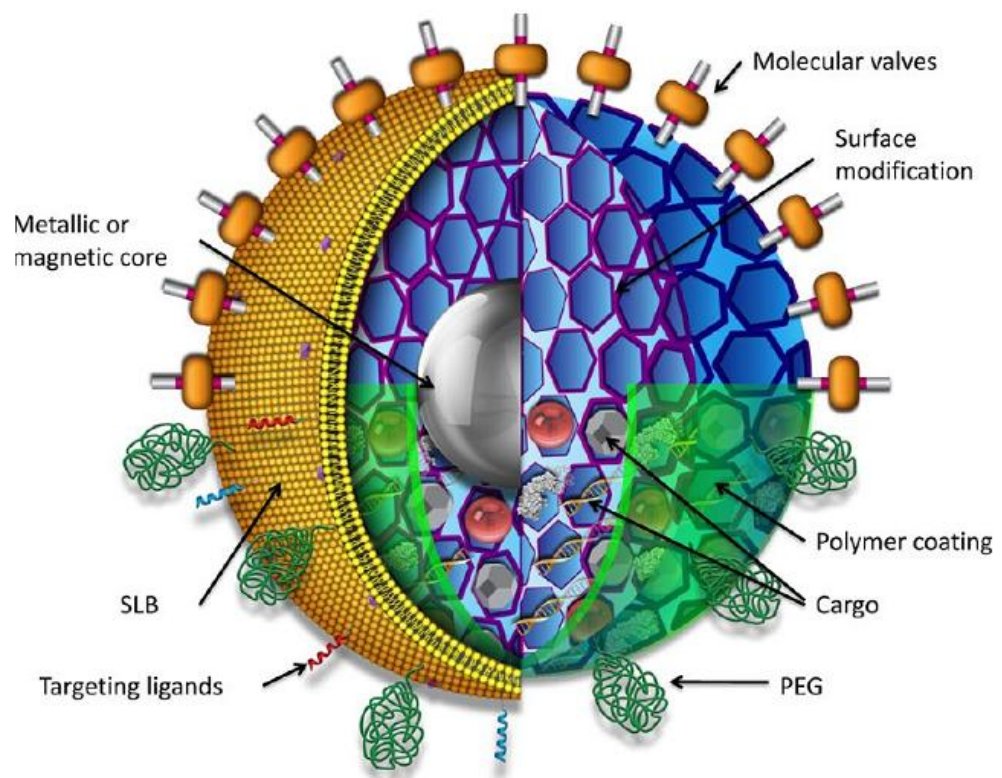


Figure 3. MSNs can be modified from inner to outer space by various designed system to realize drug delivery and targeted uptake by cells<sup>18</sup>

### 1.3. References

1. Huirache-Acuna, R.; Nava, R.; Peza-Ledesma, C. L.; Lara-Romero, J.; Alonso-Nunez, G.; Pawelec, B.; Rivera-Munoz, E. M. SBA-15 Mesoporous Silica as Catalytic Support for Hydrodesulfurization Catalysts-Review. *Materials* 2013, 6, 4139-4167.
2. Wan, Y.; Zhao, D. Y. On the controllable soft-templating approach to mesoporous silicates. *Chem Rev* 2007, 107, 2821-2860.
3. Yang, H. F.; Lu, Q. Y.; Gao, F.; Shi, Q. H.; Yan, Y.; Zhang, F. Q.; Xie, S. H.; Tu, B.; Zhao, D. Y. One-step synthesis of highly ordered mesoporous silica monoliths with metal oxide nanocrystals in their channels. *Adv Funct Mater* 2005, 15, 1377-1384.
4. Dai, P.; Wang, Y. X.; Wu, M. Z.; Xu, Z. M. Optical and magnetic properties of gamma-Fe<sub>2</sub>O<sub>3</sub> nanoparticles encapsulated in SBA-15 fabricated by double solvent technique. *Micro Nano Lett* 2012, 7, 219-222.
5. Kruk, M.; Jaroniec, M.; Ko, C. H.; Ryoo, R. Characterization of the porous structure of SBA-15. *Chem Mater* 2000, 12, 1961-1968.
6. Kresge, C. T.; Leonowicz, M. E.; Roth, W. J.; Vartuli, J. C.; Beck, J. S. Ordered Mesoporous Molecular-Sieves Synthesized by a Liquid-Crystal Template Mechanism. *Nature* 1992, 359, 710-712.
7. Beck, J. S.; Vartuli, J. C.; Roth, W. J.; Leonowicz, M. E.; Kresge, C. T.; Schmitt, K. D.; Chu, C. T. W.; Olson, D. H.; Sheppard, E. W.; Mccullen, S. B.; Higgins, J. B.; Schlenker, J. L. A New Family of Mesoporous Molecular-Sieves Prepared with



- Liquid-Crystal Templates. *J Am Chem Soc* 1992, 114, 10834-10843.
8. Li, Z. X.; Barnes, J. C.; Bosoy, A.; Stoddart, J. F.; Zink, J. I. Mesoporous silica nanoparticles in biomedical applications. *Chem Soc Rev* 2012, 41, 2590-2605.
  9. Ying, J. Y.; Mehnert, C. P.; Wong, M. S. Synthesis and applications of supramolecular-templated mesoporous materials. *Angew Chem Int Edit* 1999, 38, 56-77.
  10. Firouzi, A.; Kumar, D.; Bull, L. M.; Besier, T.; Sieger, P.; Huo, Q.; Walker, S. A.; Zasadzinski, J. A.; Glinka, C.; Nicol, J.; Margolese, D.; Stucky, G. D.; Chmelka, B. F. Cooperative Organization of Inorganic-Surfactant and Biomimetic Assemblies. *Science* 1995, 267, 1138-1143.
  11. Brinker, C. J.; Scherer, G. W. *Sol-gel science: the physics and chemistry of sol-gel processing*. Academic press: 2013, 130-150.
  12. Grun, M.; Lauer, I.; Unger, K. K. The synthesis of micrometer- and submicrometer-size spheres of ordered mesoporous oxide MCM-41. *Adv Mater* 1997, 9, 254-&.
  13. Stober, W.; Fink, A.; Bohn, E. Controlled Growth of Monodisperse Silica Spheres in Micron Size Range. *J Colloid Interf Sci* 1968, 26, 62-&.
  14. Cai, Q.; Luo, Z. S.; Pang, W. Q.; Fan, Y. W.; Chen, X. H.; Cui, F. Z. Dilute solution routes to various controllable morphologies of MCM-41 silica with a basic medium. *Chem Mater* 2001, 13, 258-263.
  15. Suzuki, K.; Ikari, K.; Imai, H. Synthesis of silica nanoparticles having a well-ordered mesostructure using a double surfactant system. *J Am Chem Soc* 2004,

126, 462-463.

16. Thomas, C. R.; Ferris, D. P.; Lee, J. H.; Choi, E.; Cho, M. H.; Kim, E. S.; Stoddart, J. F.; Shin, J. S.; Cheon, J.; Zink, J. I. Noninvasive Remote-Controlled Release of Drug Molecules in Vitro Using Magnetic Actuation of Mechanized Nanoparticles. *J Am Chem Soc* 2010, 132, 10623-10625.

17. Meng, H.; Xue, M.; Xia, T.; Ji, Z. X.; Tarn, D. Y.; Zink, J. I.; Nel, A. E. Use of Size and a Copolymer Design Feature To Improve the Biodistribution and the Enhanced Permeability and Retention Effect of Doxorubicin-Loaded Mesoporous Silica Nanoparticles in a Murine Xenograft Tumor Model. *Acs Nano* 2011, 5, 4131-4144.

18. Tarn, D.; Ashley, C. E.; Xue, M.; Carnes, E. C.; Zink, J. I.; Brinker, C. J. Mesoporous Silica Nanoparticle Nanocarriers: Biofunctionality and Biocompatibility. *Accounts Chem Res* 2013, 46, 792-801.

19. Lu, J.; Liong, M.; Zink, J. I.; Tamanoi, F. Mesoporous silica nanoparticles as a delivery system for hydrophobic anticancer drugs. *Small* 2007, 3, 1341-1346.

20. Meng, H. A.; Xue, M.; Xia, T. A.; Zhao, Y. L.; Tamanoi, F.; Stoddart, J. F.; Zink, J. I.; Nel, A. E. Autonomous in Vitro Anticancer Drug Release from Mesoporous Silica Nanoparticles by pH-Sensitive Nanovalves. *J Am Chem Soc* 2010, 132, 12690-12697.

21. Lu, J.; Choi, E.; Tamanoi, F.; Zink, J. I. Light-activated nanoimpeller-controlled drug release in cancer cells. *Small* 2008, 4, 421-426.

22. Ferris, D. P.; Zhao, Y. L.; Khashab, N. M.; Khatib, H. A.; Stoddart, J. F.; Zink, J. I. Light-Operated Mechanized Nanoparticles. *J Am Chem Soc* 2009, 131, 1686-+.

23. Matsumura, Y.; Maeda, H. A New Concept for Macromolecular Therapeutics in Cancer-Chemotherapy - Mechanism of Tumoritropic Accumulation of Proteins and the Antitumor Agent Smancs. *Cancer Res* 1986, 46, 6387-6392.
24. Argyo, C.; Weiss, V.; Brauchle, C.; Bein, T. Multifunctional Mesoporous Silica Nanoparticles as a Universal Platform for Drug Delivery. *Chem Mater* 2014, 26, 435-451.

## Chapter 2

Synthesis, Characterization and Derivatization of Nanoparticle for theranostics

## **2.1. Introduction**

### **2.1.1. MSNs synthesis optimization**

The MCM-41 formation mechanism has been studied for a long time and explained as a result of interaction between charged surfactant micelles and silicates, as well as hydrolysis and condensation under certain pH. In terms of the experiment's procedure, the constant temperature, stirring speed and reaction pH all influence the shape and morphology of synthesized MCM-41 particles. When all the parameters are controlled accurately we can get particles with about 100 nm diameter and 2D hexagonal porous structure observed under TEM.<sup>1, 2</sup> Figure 2.1 (a) and (b) are unsuccessful MCM-41 particles synthesized when (a) pH is lower than typical value of 12, and (b) temperature is unstable during reaction. Generally speaking, in acidic solution condensation rate is slower than hydrolysis rate and in base solution the other way around. The reaction temperature affects the hydrolysis and condensation rate as well as the nucleation process. Figure 2.1 (c) shows successfully synthesized MCM-41 by utilizing cetyltrimethylammonium bromide (CTAB) as structure directing agent, and tetraethyl orthosilicate (TEOS) as silica source in basic aqueous solution. These particles have uniform size distribution and typical mesoporous structure. It is also observed that there are crosslink among part of the particles, and to solve this problem we find that adding ethyl acetate help reduce the crosslink between particles and improve the uniform size distribution as shown in Figure 2.1 (d). Moreover, the hydrodynamic size of MCM-41 synthesized from the method without ethyl acetate measured by DLS usually shows 200 nm diameter, while the particles

synthesized with the modified procedure shows around 100 nm diameter.<sup>3</sup>

We also synthesized 50 nm MSNs making use of a double surfactant method.<sup>4</sup> Besides cetyltrimethylammonium bromide (CTAB), a polymer pluronic F 127 was added to the aqueous solution which prevents the particle from growing bigger in the aging process. Figure 2.2 shows the morphology and porous structure of the 50 nm MSNs. A worm-like mesoporous structure was observed, which has a different loading capability from that of the 2D hexagonal structure. The smaller size MSN significantly improve the enhanced permeability and retention (EPR) effect when coated with polyethylene and polyethylene glycol as reported by our group.<sup>5</sup> It is also shown that 50 nm particles have a higher uptake by macrophages than 100 nm particles in Figure 2.11.

### **2.1.2. Fe<sub>3</sub>O<sub>4</sub>@SiO<sub>2</sub> core/shell nanoparticle synthesis optimization**

We synthesized Fe<sub>3</sub>O<sub>4</sub>@SiO<sub>2</sub> core/shell nanoparticle to make use of the magnetic core for targeting and thermally triggered release. It is known that magnetic nanocrystals can generate heat under an oscillating magnetic field. In a traditional Fe<sub>3</sub>O<sub>4</sub>@SiO<sub>2</sub> synthesis, 10 nm iron oxide nanocrystal was transferred into CTAB aqueous solution, mixed with base solution at 80 °C and followed by adding TEOS.<sup>6</sup> Particles synthesized by this method have a wide size distribution and a significant percentage of particles have multicores inside the silica shell. We want to synthesize Fe<sub>3</sub>O<sub>4</sub>@SiO<sub>2</sub> with only one core in each particle to make sure all the particles increase to the same temperature and response to the oscillating magnetic field in the same manner. We adjusted the pH slightly higher or lower to improve the particle quality as

shown in Figure 2.3. Different amounts of NaOH solution was added into the reaction, and the  $\text{Fe}_3\text{O}_4@\text{SiO}_2$  particle became more uniform when a small amount of base was added. This result indicates a relation between reaction pH and  $\text{Fe}_3\text{O}_4@\text{SiO}_2$  size distribution. Lower pH can decrease the condensation rate and increase hydrolysis rate. We also observed a lot of free silica without  $\text{Fe}_3\text{O}_4$  core.

After trying various methods and conditions, we found that the method reported by Hyeon is most repeatable and as-synthesized particles exhibit single  $\text{Fe}_3\text{O}_4$  core in each particles with very narrow size distribution.<sup>3</sup> The modified method decreases the reaction temperature to 70 °C and extends the reaction time from 2 hours to 3 hour to allow sufficient time for particle aging. Moreover, an additional reagent ethyl acetate, is mixed with the aqueous solution, which lowers the reaction pH so that both the condensation and hydrolysis rate change. Moreover, the particle size can be tuned by adjusting the  $\text{Fe}_3\text{O}_4/\text{TEOS}$  ratio. Figure 2.4 shows particles from 80 nm to 50 nm synthesized by using different amount of  $\text{Fe}_3\text{O}_4$  mixed with constant amount of TESO. This can be explained as the more  $\text{Fe}_3\text{O}_4$  cores, the larger the number of particles and the thinner the mesoporous silica shells. These particles all incorporate a 10 nm  $\text{Fe}_3\text{O}_4$  core. We also tried 20 nm  $\text{Fe}_3\text{O}_4$  using the same method and got uniformly distributed particles without crosslink as shown in Figure 2.5. We also observed that the mesoporous structure in these  $\text{Fe}_3\text{O}_4@\text{SiO}_2$  core/shell nanoparticle is radial instead of 2D hexagonal, which will influence the uptake and release capacity which will be introduced in Chapter 5.

### **2.1.3. Derivative MSNs with different charges**

MCM-41 exhibits a zeta potential of about  $-10$  mV due to deprotonation of surface silanol groups in neutral water. Phosphonate groups or amine groups can be post-grafted onto as-synthesized particles to make the surface negatively charged or positively charged.<sup>1,7</sup> The porous structure and particle shape are not affected by the grafted reagents. In a typical synthesis, 3-trihydroxysilpropylmethylphosphonate was used for post-grafting the phosphonate group resulting in around  $-40$  mV surface charge, and 3-aminopropyltriethoxysilane was used for post-grafting amine groups to make surface charge around  $40$  mV. The charge density can be tuned by varying the functional groups concentration on the particles. As shown in Figure 2.6, phosphonated particles have the advantage of less aggregation than plain particles, because the phosphonate groups reduce hydrogen bonding among the particle and electrostatically repel each other, while the amine groups can interact with silanol groups by hydrogen bonding.

Besides the post-grafting method, we are also using the co-condensation method to improve the inner pore surface charge modification by either phosphonate groups or amine groups. In this method, alkoxysilanes with charged groups are mixed with TEOS and added to the aqueous solution drop-wise. In this way, the functional groups are incorporated into the particle framework as well as inner pores surfaces. As shown in Figure 2.7 (a), co-condensation of 3-trihydroxysilpropylmethylphosphonate with TEOS result in micrometer size particles, because the two silanes have different hydrolysis and condensation rates, 3-trihydroxysilpropylmethylphosphonate has hydroxyl groups which immediate condense in base solution. We found another silane



diethylphosphatoethyltriethoxysilane, which has same triethoxy groups as TEOS and is expected to have similar hydrolysis and condensation rate as TEOS. Figure 2.7 (b) shows that co-condensation of diethylphosphatoethyltriethoxysilane with TEOS preserves the particle size as well as the mesoporous structure. The method also applies to 3-aminopropyltriethoxysilane co-condensation with TEOS as shown in Figure 2.7 (c).

#### **2.1.4. Derivative Fe<sub>3</sub>O<sub>4</sub>@SiO<sub>2</sub> with phosphonate groups**

Fe<sub>3</sub>O<sub>4</sub>@SiO<sub>2</sub> core/shell nanoparticle can be modified with phosphonate groups or amine groups using the same method as MCM-41, namely post-graft or co-condensation. We observed that co-condensation of phosphonate lead to different pore sizes of Fe<sub>3</sub>O<sub>4</sub>@SiO<sub>2</sub> comparing to those in unmodified particles as shown in Figure 2.8, which doesn't happen to MCM-41. Based on the N<sub>2</sub> adsorption-desorption measurement and XRD spectra shown in Figure 2.9, phosphonated Fe<sub>3</sub>O<sub>4</sub>@SiO<sub>2</sub> by co-condensation has a surface area of 570 m<sup>2</sup>/g, total pore volume of 0.55 cc/g, and pore size of 2.5 nm after surfactant extraction. The unmodified Fe<sub>3</sub>O<sub>4</sub>@SiO<sub>2</sub> has a surface area of 530 m<sup>2</sup>/g, total pore volume of 0.66 cc/g, and pore size of 4.5 nm. The smaller pores size of co-condensed particle is due to coverage of phosphonate groups on the inner pores surfaces of Fe<sub>3</sub>O<sub>4</sub>@SiO<sub>2</sub> nanoparticle, and we believe this indicates successful modification of the inner pore, which is essential to improve drug loading.

#### **2.1.5. Florescent dye labeled MSNs**

When cells are incubated with MSNs, we need to prove that the particles are taken up by the cells.<sup>8</sup> One method to trace the distribution of MSNs in cells is to

label the particles with fluorescent dyes and monitor them using fluorescence microscopy. The two most widely used molecules *in vitro* are fluorescein isothiocyanate (FITC) and rhodamine isothiocyanate (RITC). Figure 2.10 shows the synthesis pathway to make fluorescent dye precursor. The isothiocyanate chemical (FITC/RITC) are mixed with 3-aminopropyltriethoxysilane (APTES) in anhydrous ethanol under N<sub>2</sub> for 2 hours to produce the precursor, which can be incorporated into the particles by post-grafting or co-condensation. As shown in Figure 2.11 (a), (b) and (c), RITC labeled MSNs emitting red fluorescence were found surrounding the macrophage nuclei and bacteria. In figure 2.10 (d), fluorescence images prove that FITC labeled MSN were avidly taken up by pancreatic cancer cells over time.

Another dye we used to conjugate on the particle is Nile blue, which is a hydrophobicity indicator. There is no emission fluorescence in aqueous environment and blue fluorescence emission in hydrophobic environment or nonpolar solvents. The dye molecule doesn't have an isothiocyanate group, but we react its amine groups with 3-iodopropyltrimethoxysilane (IPTMS) and then post-graft them on the particles. The synthesis pathway is shown in Figure 2.12 (a). The amine groups can react with carbon next to the iodo group through nucleophilic reaction. And the reaction is catalyzed by N, N-diisopropylethylamine (DIEA). The blue fluorescence image in Figure 2.12 (b) indicates that there are lots of hydrophobic regions in the cells, such as phospholipid bilayers, protein hydrophobic regions, and so on.

In terms of the *in vivo* studies, we utilized another NIR fluorescent dye, DyLight 680 NHS ester, to attach on the particles.<sup>5</sup> In the same way as FITC or RITC, DyLight

680 NHS ester was first mixed with APTES in anhydrous ethanol under inert atmosphere for 12 h, and then post-grafted on MSNs in the same solution. By means of this labeling method, we are able to detect the fluorescence of the particles and measure their intensities in different organs. As shown in Figure 2.13, 50 nm MSNs were found to accumulate more than 100 nm particles in lungs and livers. This result helps us to determine the preferred particle size for *in vivo* study.

#### **2.1.6. MSNs functionalized with pH-sensitive nanovalves and disulfide snap-top**

We have developed three different kinds of pH-sensitive nanovalves to trap and release drugs. As shown in Figure 2.14, all of them consist of a stalk with a bulky group and a cap.<sup>7, 9, 10</sup> The  $\alpha$ -cyclodextrin ( $\alpha$ -CD) or  $\beta$ -cyclodextrin ( $\beta$ -CD) acts as cap to trap the cargo inside and binds to the organic moiety through hydrophobic-hydrophobic interaction. When the pH is lower than 6, the binding affinity between the protonated stalk and cap immediately decreases, leading to dissociation of the cap and cargo release. The stalks are attached over the pores by a two-step synthesis and both of the aniline alkane amine and benzimidazole groups have  $pK_a$  around 6, which determine the release pH of the nanovalve.

In addition, we also developed a disulfide snap-top as shown in Figure 2.15. The capping mechanism is similar as pH-sensitive nanovalve, and the release property is realized through cleavage of disulfide bond by reducing agent. Particles enabled with different nanovalves exhibit different uptake and release capacities. The optimization and application of pH-sensitive nanovalve and disulfide snap-top will be extensively discussed in Chapters 3, 4, and 5.

### 2.1.6. Fe<sub>3</sub>O<sub>4</sub>@SiO<sub>2</sub> core/shell nanoparticle coated with phase change materials

We are developing a thermal-sensitive material for capping the pores as well as releasing the drug/dye molecule from core/shell nanoparticles when the temperature is above 37 °C. One of the designed systems is to make use of paraffins, which has different melting points dependent on the hydrocarbon chain length.<sup>11</sup> As shown in Figure 2.16 (a), to improve the coating of paraffin by hydrophobic-hydrophobic interaction, octadecyltrimethoxysilane was first attached on the particles. It is reported by Amoros that three paraffin materials heneicosane, docosane and tetracosane have melting points of 39 °C, 42 °C and 50 °C respectively. We choose heneicosane for the coating material because its 39 °C melting point is slightly higher than human body temperature (37 °C). We expect the drug to be trapped inside the pores at body temperature and released when the environmental temperature is above the melting point. Fe<sub>3</sub>O<sub>4</sub>@SiO<sub>2</sub> were first loaded with Hoechst in aqueous solution and then modified with octadecyltrimethoxysilane in acetonitrile. The particles were washed by acetonitrile and transferred to hexane mixed with paraffin. The gated particles were further washed with water to remove the surface absorbed dye molecule. Time-resolved fluorescence spectroscopy was utilized to observe released dye fluorescence intensity over time. Figure 2.16 (b) proves that at room temperature and 40 °C there is no obvious release observed from the particles. Particles were placed at the bottom of a cuvette and a laser beam directed through the supernatant. The fluorescence spectrum from the supernatant was collected at 1s intervals over the course of the experiment. Although the paraffin starts melting at 39 °C, its diffusion is

too slow in aqueous solution to unclog the pores and release the dye molecule. Further increase to 60 °C facilitates the melting and diffusion of heneicosane in water, and a significant Hoechst release was observed. After reaching the maximum release point, there is a little decrease of fluorescence intensity caused by the thermal heating for around 16 hours. This platform has the potential to be applied for *in vitro* study under oscillating magnetic fields, which requires further optimization of release capacity.

Due to the coating of paraffin, the particle surface is very hydrophobic and particles don't disperse well in aqueous solution. To solve this problem, we tried to derivatize the particle surface with 2-[methoxy(polyethyleneoxy)9-12propyl]trimethoxysilane which helps improve its hydrophilicity.

Another phase change material we utilized is 1-tetradecanol (1-TD) with a melting point of 39 °C.<sup>12-14</sup> As shown in Figure 2.17 (a), 1-TD was coated around the particle through interaction between its hydrocarbon chain and ethyleneoxy repeating units in the polymer. The particles were first loaded with rhodamine 6G and attached with 2-[methoxy(polyethyleneoxy)9-12propyl]trimethoxysilane in methanol. After all of the methanol evaporated under heating, 1-tetradecanol (1-TD) and hot water were added and stirred for 1 hour. There was a phase separation of excess 1-TD and particles dispersed in aqueous solution. The coated particles were centrifuged down and washed with cold water to remove surface impurities. Figure 2.17 (b) shows that uncapped particles release the dye when heated up to 37 °C and 50 °C, which indicates thermal heating facilitates the cargo molecule diffuse out of the pores. In

contrast, particles capped with 1-TD has no release at 37 °C and moderate release at 50 °C. The non-release behavior at 37 °C is due to capping of 1-TD below its melting temperature. On the other hand, this system needs lots of improvement and optimization since the release capacity is low.

### **2.1.7. MSNs derivatized with other thermal-sensitive polymer**

Two other polymers were utilized because of their thermal properties. Polycaprolactone diol with a molecular weight of 2000 has a softening point of 55 °C. The hydroxyl group can react with isocyanate group from the linker shown in Table 2.1. Particles were first derivatized with linkers and loaded with dye solution, and then coated with a layer of polymer. Polyethylene glycol (PEG) also reacted with 3-(triethoxysilyl)propylisocyanate and PEG with a molecular weight of 1400-1600 was coated around the particles. Both systems exhibit release behaviors under 65 °C as shown in Figure 2.18. However, we didn't apply these two systems for *in vitro* or *in vivo* study because they don't exhibit a high release capacity.

## **2.2 Experimental Section**

*Materials:* All chemicals are used as purchased: Cetyltrimethylammonium bromide (CTAB, 95%), tetraorthoethylsilicate (TEOS, 98%), 3-(trihydro-xysilyl)propyl methylphosphonate (42% in H<sub>2</sub>O), 3-iodopropyltrimethoxysilane (IPTMS, 95%), N,N'-dimethylformamide (99.8%), p-anisidine (99%),  $\alpha$ -cyclodextrin ( $\geq 98\%$ ),  $\beta$ -cyclodextrin ( $\geq 98\%$ ), Hoechst 33342 ( $\geq 97\%$ ), propidium iodide (PI) ( $\geq 95\%$ ), toluene (99.8%), fluorescein isothiocyanate ( $\geq 97.5\%$ ), rhodamine B isothiocyanate (mixed isomers), Nile blue ( $\geq 75\%$ ), triethylamine ( $\geq 99\%$ ),

1-tetradecanol, polycaprolactone diol, and polyethylene glycol were purchased from Sigma (St. Louis, MO). N-phenylaminomethyltriethoxysilane (PhAMTES), Chloromethyltrimethoxysilane (90%), and N-(2-Aminoethyl)-3-aminopropyltrimethoxysilane (NAPTS, 90 %) were purchased from Gelest (Morrisville, PA). Chloroform (99%) was purchased from EMD Millipore (Billerica, MA). Fe<sub>3</sub>O<sub>4</sub> (20 nm, 50 mg) was purchased from Ocean NanoTech (San Diego, CA).

*Synthesis of MCM-41:* The synthesis of MCM-41 was based on well-established published procedures. Cetyltrimethylammonium bromide (CTAB, 250 mg, 0.7 mmol) was dissolved in H<sub>2</sub>O (120 mL) and NaOH (875  $\mu$ L, 2M). The mixture was heated up to 80 °C and kept stable for 30 minutes, followed by adding tetraethyl orthosilicate (TEOS, 1.2 mL) drop-wise into the solution while stirring vigorously. For phosphonated MCM-41, 3-(trihydroxysilyl)propyl methylphosphonate (315  $\mu$ L) was added into the solution 15 minutes after adding TEOS. For amine modified MCM-41, N-(2-Aminoethyl)-3-aminopropyltrimethoxysilane (90 %) was mixed with TEOS before adding to CTAB solution. The solution was kept at 80 °C for 2 hours. The synthesized nanoparticles were centrifuged and washed thoroughly with methanol.

*Modified Synthesis of MCM-41:* Cetyltrimethylammonium bromide (CTAB, 250 mg, 0.7 mmol) was dissolved in H<sub>2</sub>O (120 mL) and NaOH (875  $\mu$ L, 2M). The mixture was heated up to 80 °C and kept stable for 30 minutes, followed by adding tetraethyl orthosilicate (TEOS, 1.2 mL) drop-wise into the solution while stirring vigorously. Ethyl acetate (1.2 mL) was added into the mixture right after adding TEOS, and the

solution was kept at 80 °C for 2 hours.

*Traditional Synthesis of Fe<sub>3</sub>O<sub>4</sub>@SiO<sub>2</sub>:* The typical synthesis method of Fe<sub>3</sub>O<sub>4</sub>@SiO<sub>2</sub> core/shell silica nanoparticles is based on the synthesis of MCM 41 procedure and scaled down from 120 mL to 10 mL H<sub>2</sub>O. An alkaline aqueous solution (9 mL H<sub>2</sub>O, 70 µL 2.0 M NaOH) was heated to 80 °C and kept steady while stirring rapidly. Cetyltrimethylammonium bromide (20 mg) was dissolved in 1 mL water. 100 µL of iron oxide in toluene solution (5 mg/mL) was transferred to a 10 mL flask and blown dry by air. After that 1 mL of chloroform was added to disperse the iron oxide again to get a dark solution and this was mixed with the 1 mL aqueous CTAB solution prepared before. Chloroform was boiled off the solution upon heating, and the oil-in-water microemulsion finally became clear brown. This mixture was sonicated for a few minutes to make sure there was no aggregation of iron oxide nanoparticles. The iron oxide mixture was added to the base solution, and after around ten minutes the temperature was steady at 80 °C. Finally, tetraethyorthosilicate (TEOS, 100 µL) was added into the solution stirring for 2 hours at 80 °C. When the reaction finished, Fe<sub>3</sub>O<sub>4</sub>@SiO<sub>2</sub> was washed with methanol or ethanol twice or three times. The centrifuged iron oxide core/shell silica nanoparticles are dark brown. To get negatively charged particles, diethylphosphatoethyltriethoxysilane (10 µL) was mixed with 100 µL TEOS to co-condense the phosphonate groups with silica, and to make positively charged particles, APTES (20 µL) was mixed with the as-synthesized particle (100 mg) in anhydrous ethanol under N<sub>2</sub> and stirred overnight.

*Modified Synthesis of Fe<sub>3</sub>O<sub>4</sub>@SiO<sub>2</sub>:* The synthesis procedure is very similar to the



traditional method, except that reaction was undertaken at 70 °C for 3 hours and ethyl acetate was added right after TEOS. A solution of 9 mL water, 60 µL 2.0 M NaOH was heated to 70 °C and kept steady while stirring rapidly. Cetyltrimethylammonium bromide (CTAB, 20 mg) was dissolved in 1 mL water. 90 - 170 µL of iron oxide in toluene solution (5 mg/mL) was transferred to a 10 mL flask and blown dry by air. After that 1 mL of chloroform was added to disperse the iron oxide and this was mixed with the 1 mL aqueous CTAB solution prepared before. Chloroform was boiled off the solution upon heating, and the oil-in-water microemulsion finally became clear brown. This mixture was sonicated for a few minutes to make sure there is no aggregation of iron oxide nanoparticles. The resulting solution was added to the base solution and the temperature was steady at 70 °C after 10 mins. Then, 100 µL tetraethyorthosilicate (TEOS, Aldrich, 98%) and 0.6 mL ethyl acetate were added in sequence into the solution and the mixture was stirred vigorously for 3 hours at 70 °C. When the reaction finished, the silica nanoparticles were washed and centrifuged with methanol or ethanol twice or three times. Iron oxide mesoporous silica nanoparticles synthesized with this method is uniformly monodispersed and there is little necking among the nanoparticles. As-synthesized Fe<sub>3</sub>O<sub>4</sub>@SiO<sub>2</sub> (20 mg) was dispersed in 8 mL methanol, mixed with 5.4 mg ammonium nitrate and refluxed under N<sub>2</sub> for 30 minutes. The Fe<sub>3</sub>O<sub>4</sub>@SiO<sub>2</sub> without surfactant template was collected by centrifugation and washed with methanol for twice.

*Labeling of MSNs:* In terms of post-grafting method, in a 2 mL centrifuge tube, RITC/FITC (1 mg) was mixed with APTES (2.4 µL) in 600µL anhydrous ethanol and

rotated for 2 hours. MSNs (10 mg) was mixed with 30  $\mu\text{L}$  of the RITC solution and refluxed in toluene for 12 hours. Labeled particles were washed with toluene and methanol. In terms of co-condensation, the RITC/FITC and APTES mixture was directly mixed with TEOS and added drop-wise to the base solution for making MCM-41. As for Nile blue attachment, 3-iodopropyltrimethoxysilane (IPTMS) was added into MSNs toluene dispersion and refluxed under  $\text{N}_2$  overnight. The linker modified MSNs were washed with toluene and dispersed in toluene again, followed by mixing with Nile blue and N, N-diisopropylethylamine (DIEA). For labeling MSN with NIR fluorescent dye, DyLight 680 NHS ester (0.1 mg) was mixed with APTES (0.5  $\mu\text{L}$ ) in 1 mL anhydrous ethanol under  $\text{N}_2$  at room temperature for 12 hours, and then the as-synthesized precursor was mixed with MSN in toluene and refluxed in toluene under  $\text{N}_2$  overnight.

*Synthesis of Anilinoalkane (ANA) Nanovalve:* As-synthesized MCM-41 (100 mg) was washed and dispersed in anhydrous toluene, mixed with 3-iodopropyl trimethoxysilane (IPTMS, 20  $\mu\text{L}$ , 0.1 mmol) and heated up to 40  $^\circ\text{C}$  under  $\text{N}_2$  for 12 hours. The IPTMS modified nanoparticles were washed with toluene to remove unreacted agents and re-dispersed in anhydrous toluene, and mixed with p-anisidine (123.2 mg, 1 mmol) and triethylamine (TEA, 420  $\mu\text{L}$ , 3 mmol). The solution was refluxed under  $\text{N}_2$  for another 24 hours. The final product was centrifuged and washed with toluene, methanol and water to be ready for drug/dye loading process.

*Synthesis of 1-Methyl-1H-benzimidazole (MBI) Nanovalve:* MCM-41 (100 mg) was washed and dispersed in anhydrous toluene, mixed with

chloromethyltrimethoxysilane (15  $\mu\text{L}$ ) and refluxed for 12 hours. The modified MCM-41 was washed by toluene and dimethylformamide (DMF) and dispersed in 8 ml DMF. Tetrabutylammonium iodide (2 mg), benzimidazole (12 mg) and triethylamine (150  $\mu\text{L}$ ) were added into the solution and the mixture was heated up to 70  $^{\circ}\text{C}$  under  $\text{N}_2$  for 24 hours. As-synthesized nanoparticles were washed with DMF, methanol and water thoroughly.

*Disulfide Snap-top Attachment on Phosphonated MSNs:* MCM-41 (100 mg) was dispersed into dry toluene (10 mL), mixed with (3-mercaptopropyl) trimethoxysilane (24  $\mu\text{L}$ , 0.1mmol), and refluxed for 12 hours under nitrogen atmosphere. Thiol group modified MCM-41 (100 mg) was washed and dispersed again in anhydrous toluene (10 mL) in a second step. To prepare thiocyanogen, lead thiocyanate (800 mg) was dispersed in 10 mL chloroform and titrated by bromine (200  $\mu\text{L}$ ) in chloroform (10 mL). The titration product mixture was filtered and the filtrate containing thiocyanogen in chloroform was light yellowish. 1-adamantanethiol (17 mg, 0.1 mmole) and as-synthesized thiocyanogen were added into the MSN toluene suspension. The disulfide oxidation reaction took four days under 4  $^{\circ}\text{C}$  and nitrogen gas atmosphere. As-synthesized material was yellowish and washed thoroughly with toluene, methanol and water.

*Paraffin Coating on  $\text{Fe}_3\text{O}_4@\text{SiO}_2$ :*  $\text{Fe}_3\text{O}_4@\text{SiO}_2$  (10 mg) was loaded in 1 mL Hoechst aqueous solution (5mM) first and then transferred to acetonitrile (2 mL) mixed with trimethoxyoctadecylsilane (85  $\mu\text{L}$ ) at room temperature overnight. The Hoesht loaded

MSNs were washed with acetonitrile and dispersed in 8 mL hexane. Heneicosane (0.1 g) added into the solution and this mixture was sonicated for 15 minutes in the water bath, followed by another 15 minutes stirring at room temperature. The particle was washed twice by centrifugation and the particles were placed under vacuum to remove trace amount of acetonitrile and hexane.

*Stimulated Release Studies:* The release was monitored by time-resolve fluorescence spectroscopy. To measure Hoechst release from  $\text{Fe}_3\text{O}_4@\text{SiO}_2$  and detect its fluorescence emission in supernates, dried  $\text{Fe}_3\text{O}_4@\text{SiO}_2$  powder was put in the corner of a glass vial containing 10 mL DI water. A probe laser beam (5 mW 377 nm) was passed through the supernatant fluid in the glass vial such that released Hoechst was excited. The fluorescence was detected and collected by a charge-coupled device (CCD) detector and a computer at 1 s intervals over the course of the experiment. The release profile was the plot of the integrated emission peak area between 480 nm to 520 nm as a function of time. The temperature was controlled on a hotplate.

*1-tetradecanol (1-TD) Coating on  $\text{Fe}_3\text{O}_4@\text{SiO}_2$ :*  $\text{Fe}_3\text{O}_4@\text{SiO}_2$  (20 mg) was loaded in 5 mL Rhodamine 6G (5 mM) methanol solution for 12 hours and then mixed with 2-[methoxy(polyethyleneoxy)9-12propyl]trimethoxysilane (20  $\mu\text{L}$ ) stirring under  $\text{N}_2$  overnight. The methanol solvent evaporated in air and 1-tetradecanol (1-TD) was added into the flask together with 6 mL water at 80  $^\circ\text{C}$  stirring for 1 hour. The mixture was transferred into another glass vial to separate the oil and water phase. 1-TD coated  $\text{Fe}_3\text{O}_4@\text{SiO}_2$  in water was centrifuged and washed by cold water for 4 times. The particles were placed under vacuum. The release was characterized in water and

the sample was placed in a tube soaked into a water bath. The temperature was controlled on the hotplate.

*Polycaprolactone diol/Polyethylene Glycol Grafting on MSNs:* MSNs (100 mg) was loaded in 1mL aqueous Hoechst solution (5 mM) and dried by air. The loaded particles were dispersed in toluene, followed by adding isocyanatepropyltrimethoxysilane (ICPES) and polymer polycaprolactone diol/polyethylene glycol (0.1 mmol) and refluxed under N<sub>2</sub> overnight. The Hoechst loaded MSNs were washed by methanol and deionized water. The release was characterized by time-resolve fluorescence spectroscopy.

### 2.3 Figures

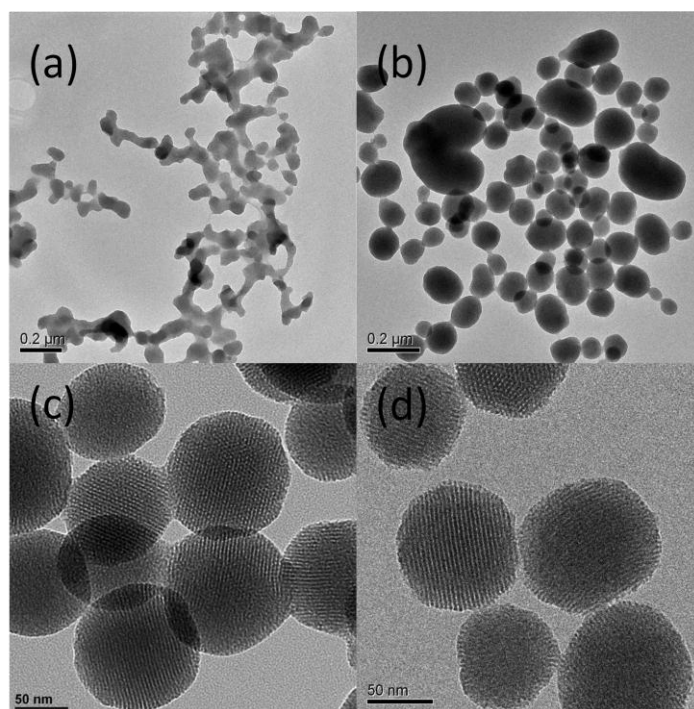


Figure 2.1. TEM images of MCM-41 synthesized (a) in pH lower than 12, (b) unstable temperature during reaction, and particles of good quality synthesized by (c) traditional method without ethyl acetate (d) and with ethyl acetate. With ester addition in the synthesis, the particles are more uniformly distributed and have fewer crosslinks among them than before.

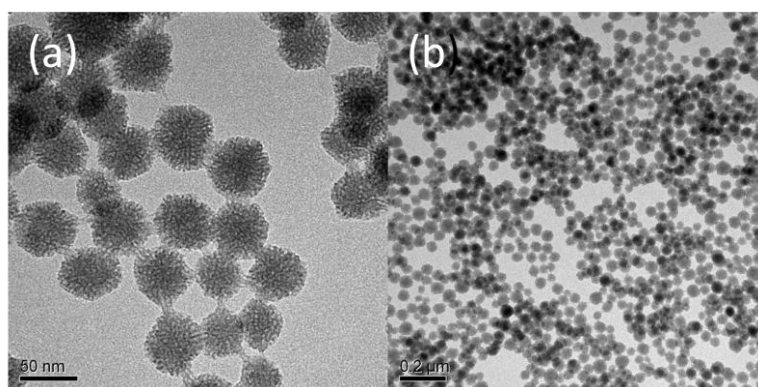


Figure 2.2. (a) & (b) 50 nm MSNs with worm-like mesoporous structure synthesized from double surfactant method.

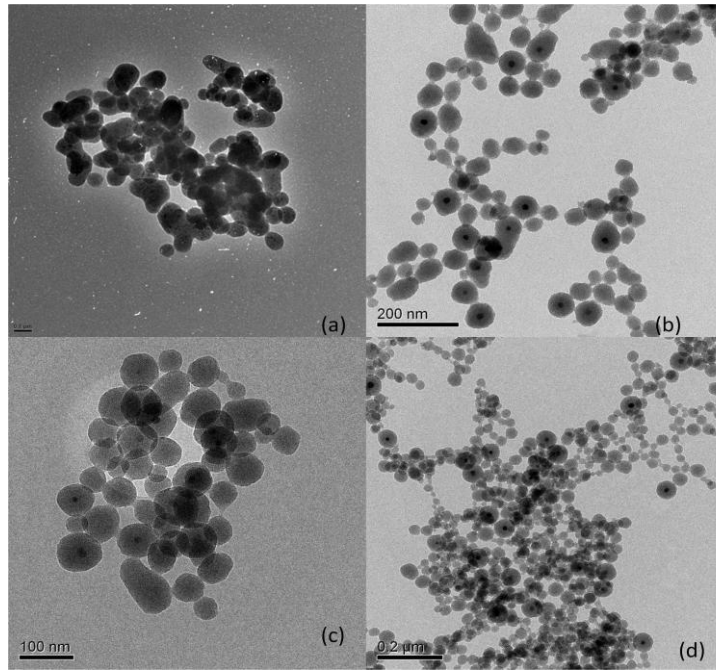


Figure 2.3.  $\text{Fe}_3\text{O}_4@\text{SiO}_2$  synthesized by traditional method exhibit wide size distribution, non-uniform  $\text{Fe}_3\text{O}_4$  distribution and free silica. The particles were synthesized with different amounts of M NaOH (a) 70  $\mu\text{L}$ , (b) 60  $\mu\text{L}$ , (c) 50  $\mu\text{L}$ , (d) 35 $\mu\text{L}$ .

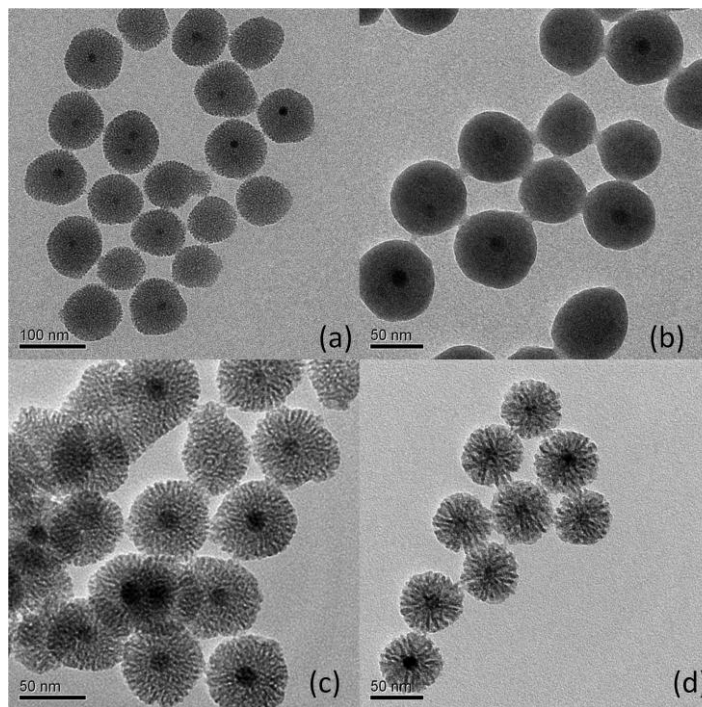


Figure 2.4.  $\text{Fe}_3\text{O}_4@\text{SiO}_2$  exhibit different sized upon mixing different amount of

Fe<sub>3</sub>O<sub>4</sub> (5 mg/mL in toluene) with aqueous base CTAB solution. (a) 80 nm Fe<sub>3</sub>O<sub>4</sub>@SiO<sub>2</sub>, 90 μL, (b) 70 nm Fe<sub>3</sub>O<sub>4</sub>@SiO<sub>2</sub>, 130 μL, (c) 60 nm Fe<sub>3</sub>O<sub>4</sub>@SiO<sub>2</sub>, 150 μL, (d) 50 nm Fe<sub>3</sub>O<sub>4</sub>@SiO<sub>2</sub>, 170 μL

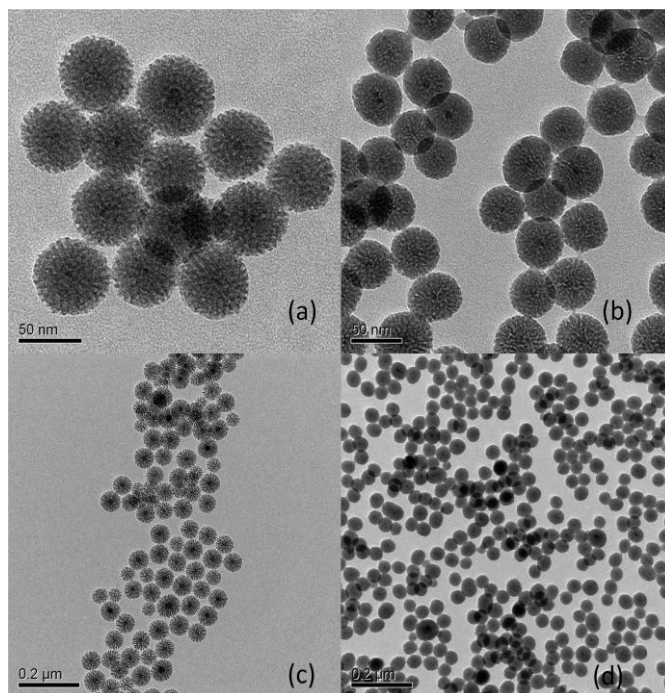


Figure 2.5. Fe<sub>3</sub>O<sub>4</sub>@SiO<sub>2</sub> with 10 nm Fe<sub>3</sub>O<sub>4</sub> core (a), (b), (c) and 20 nm core (d). All of the particles has radial mesoporous structure instead of 2D hexagonal porous.

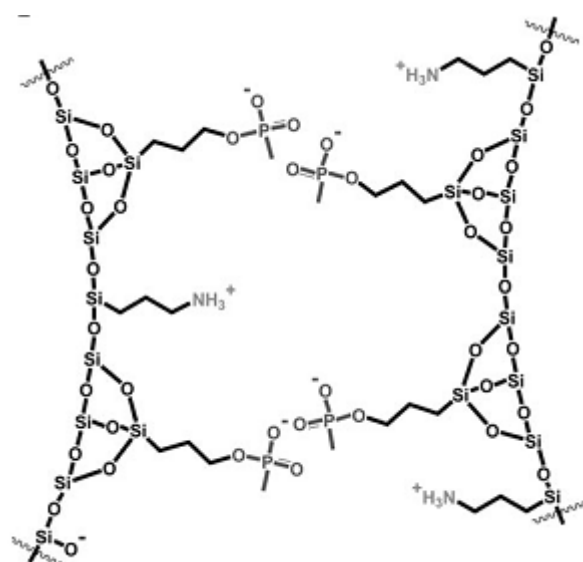


Figure 2.6. Phosphonated MCM-41 have less aggregation problem due to weaker



hydrogen bonding and negative charge repulsion.<sup>8</sup>

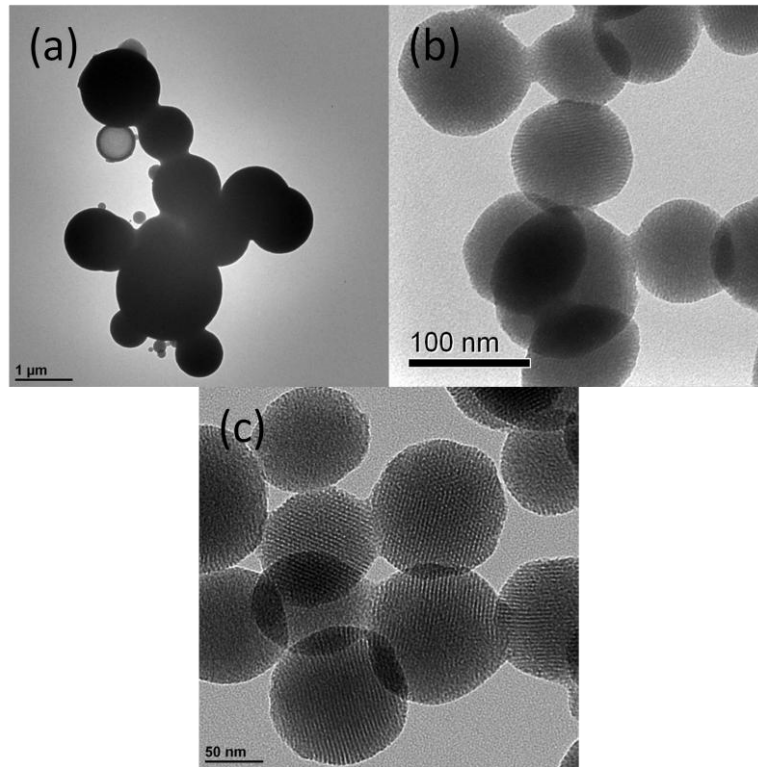


Figure 2.7. MCM-41 co-condensed with (a) 3-trihydroxysilpropylmethylphosphonate lead to particles with micrometer size, while (b) diethylphosphatoethyltriethoxysilane and (c) 3-aminopropyltriethoxysilane preserve the 100 nm size and mesoporous structure.

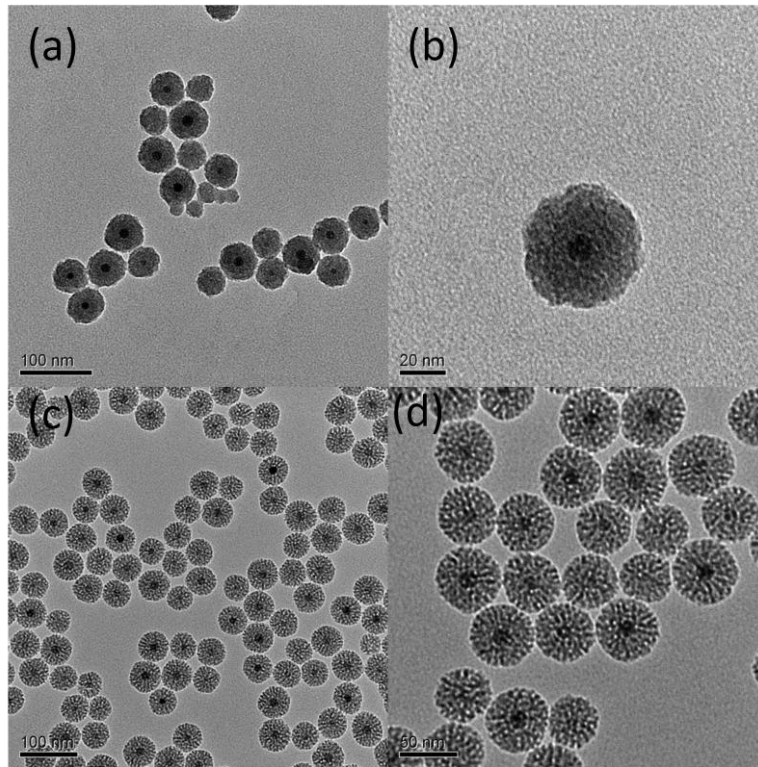


Figure 2.8.  $\text{Fe}_3\text{O}_4@\text{SiO}_2$  modified with diethylphosphatoethyltriethoxysilane by co-condensation (a), (b), and unmodified  $\text{Fe}_3\text{O}_4@\text{SiO}_2$  (c), (d). Both particles have radial mesoporous structure but different sizes.

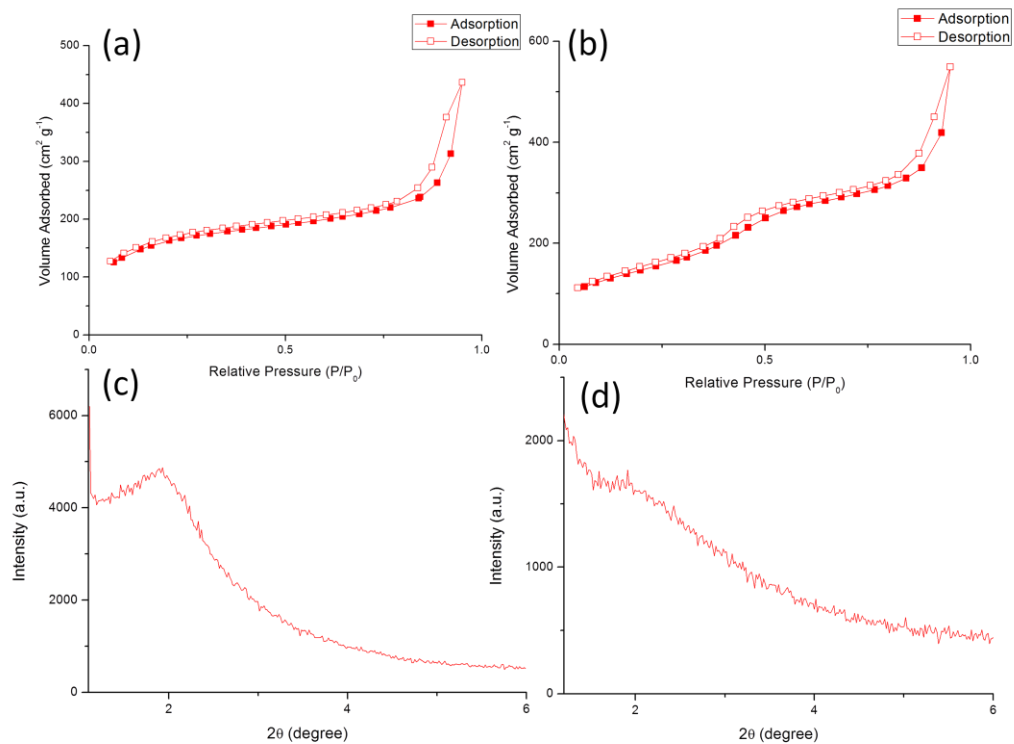


Figure 2.9. N<sub>2</sub> adsorption-desorption isothermals of (a) phosphonated Fe<sub>3</sub>O<sub>4</sub>@SiO<sub>2</sub> by co-condensation, (b) plain Fe<sub>3</sub>O<sub>4</sub>@SiO<sub>2</sub>, and XRD spectra of (c) phosphonated Fe<sub>3</sub>O<sub>4</sub>@SiO<sub>2</sub> by co-condensation and (d) plain Fe<sub>3</sub>O<sub>4</sub>@SiO<sub>2</sub>.

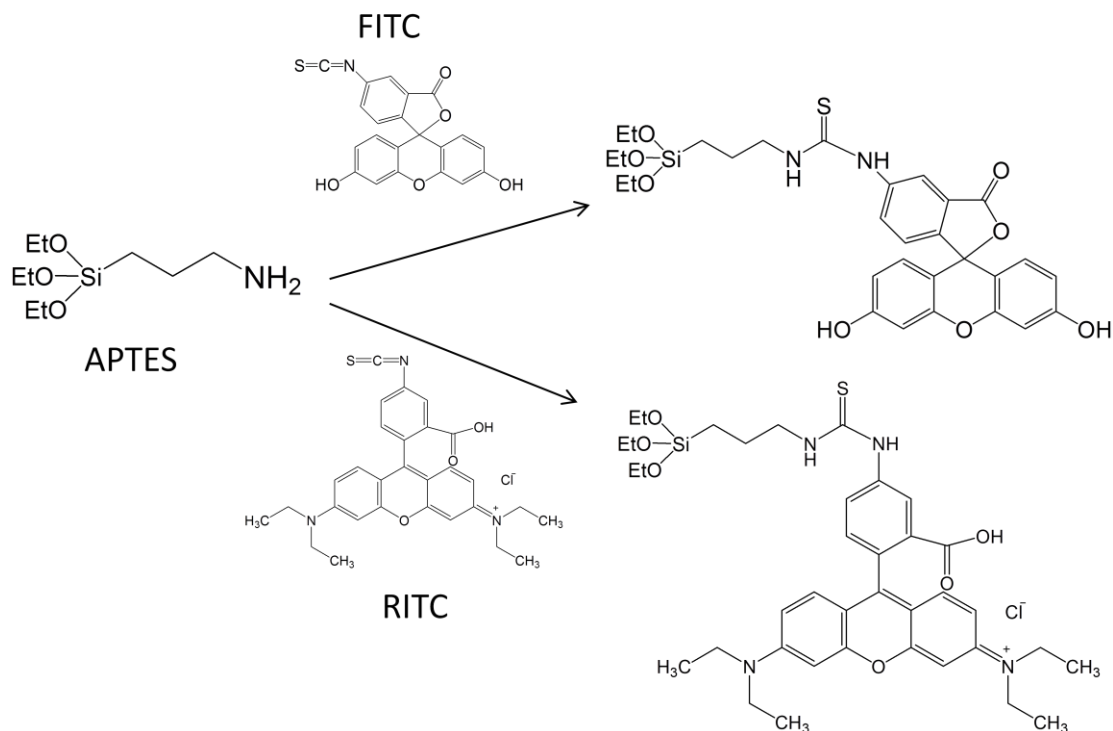


Figure 2.10. Mixing APTES with FITC or RITC at room temperature under N<sub>2</sub> atmosphere produces fluorescent dye precursor, which can be incorporated into MSNs by post-grafting or co-condensation.

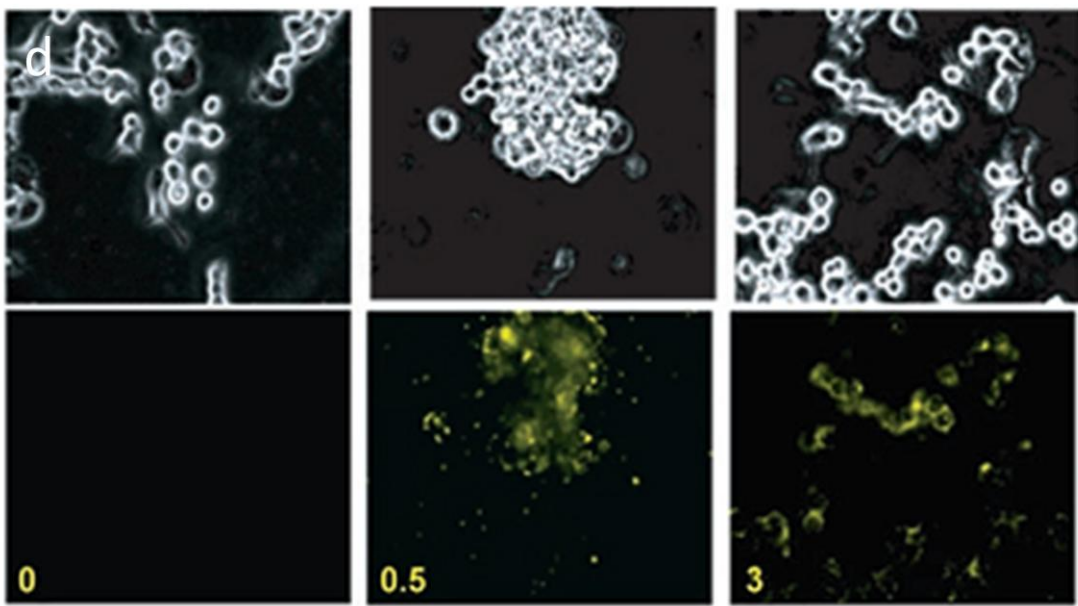
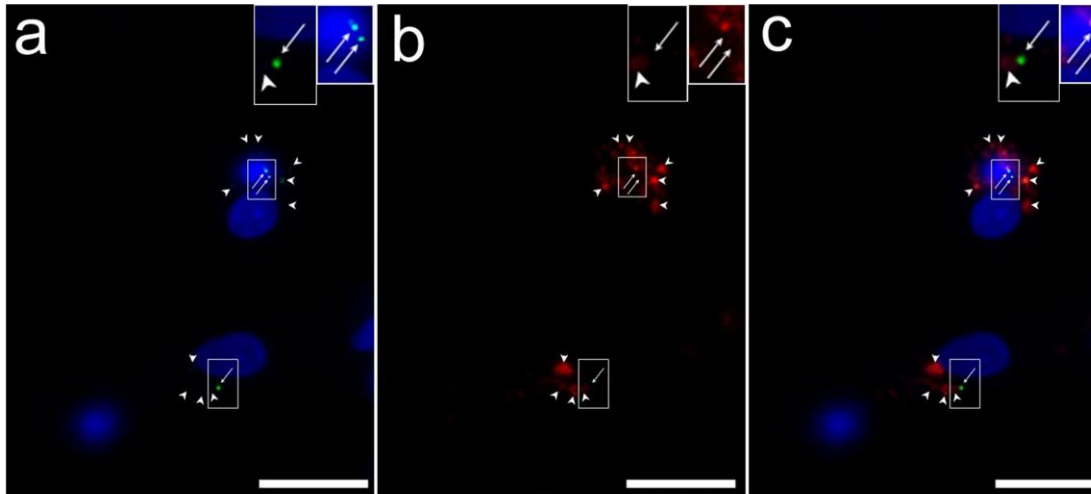


Figure 2.11. (a) *F. tularensis*-infected human monocyte derived macrophoages nucleus were stained with DAPI as blue fluorescence and bacteria were expressing GFP as green fluorescence, (b) RITC labeled MSNs distribution and (c) merged image showing that particles overlap with bacterial. (d) Upper panel shows microscopy images of pancreatic cancer cells and lower panel shows FITC labeled particles taken up by cancer cell over time.

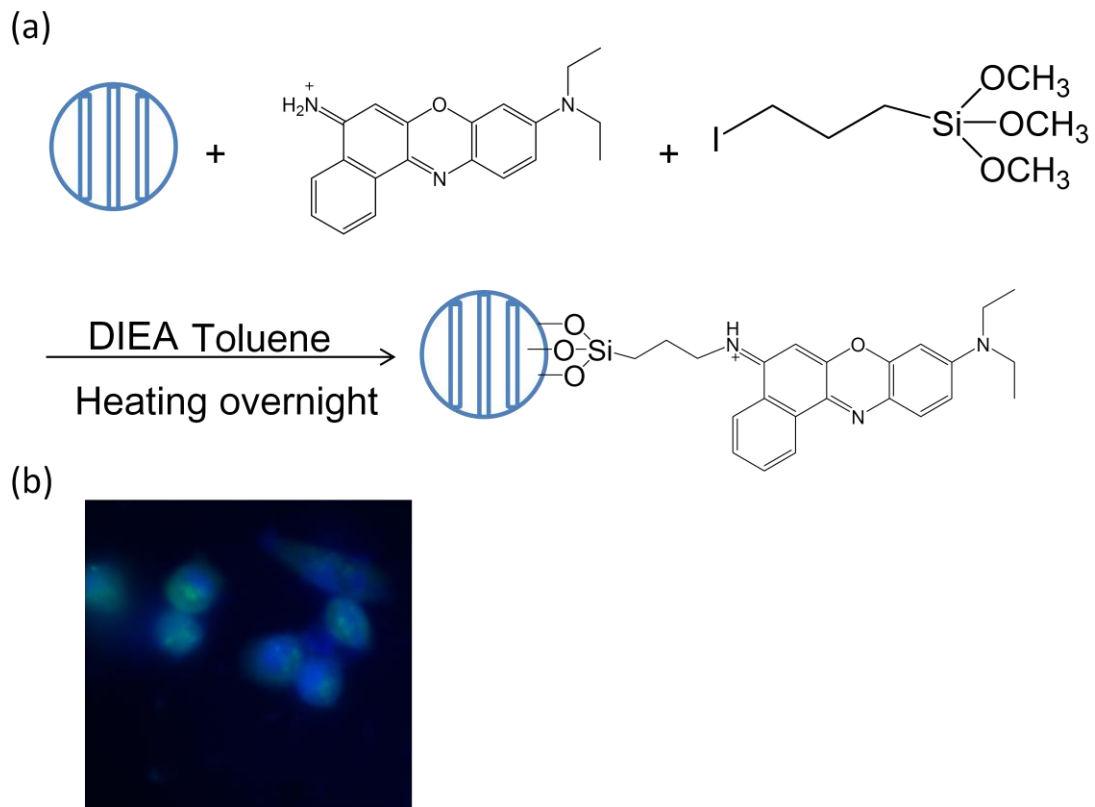


Figure 2.12 (a) Synthesis pathway of attaching Nile blue onto the MSNs. (b)

Fluorescence image of MSNs labeled with Nile blue taken up by MiaPaca-2 cell line

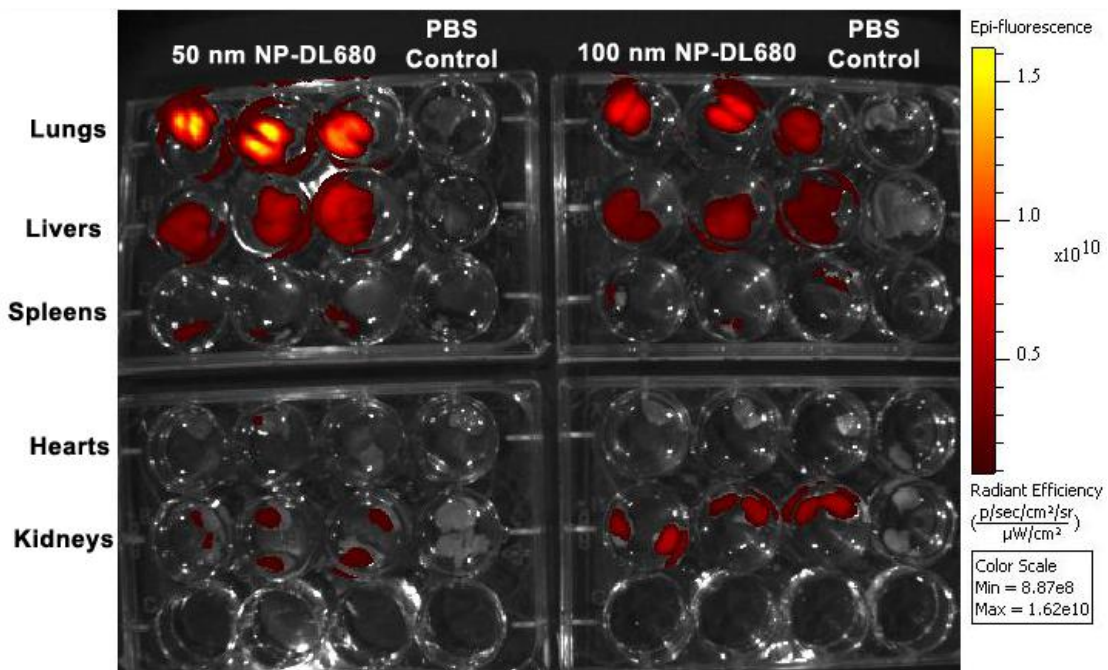


Figure 2.13. 50 nm and 100 nm MSNs labeled with Dylight 680 NHS ester were used

to determine their biodistribution in different organs.

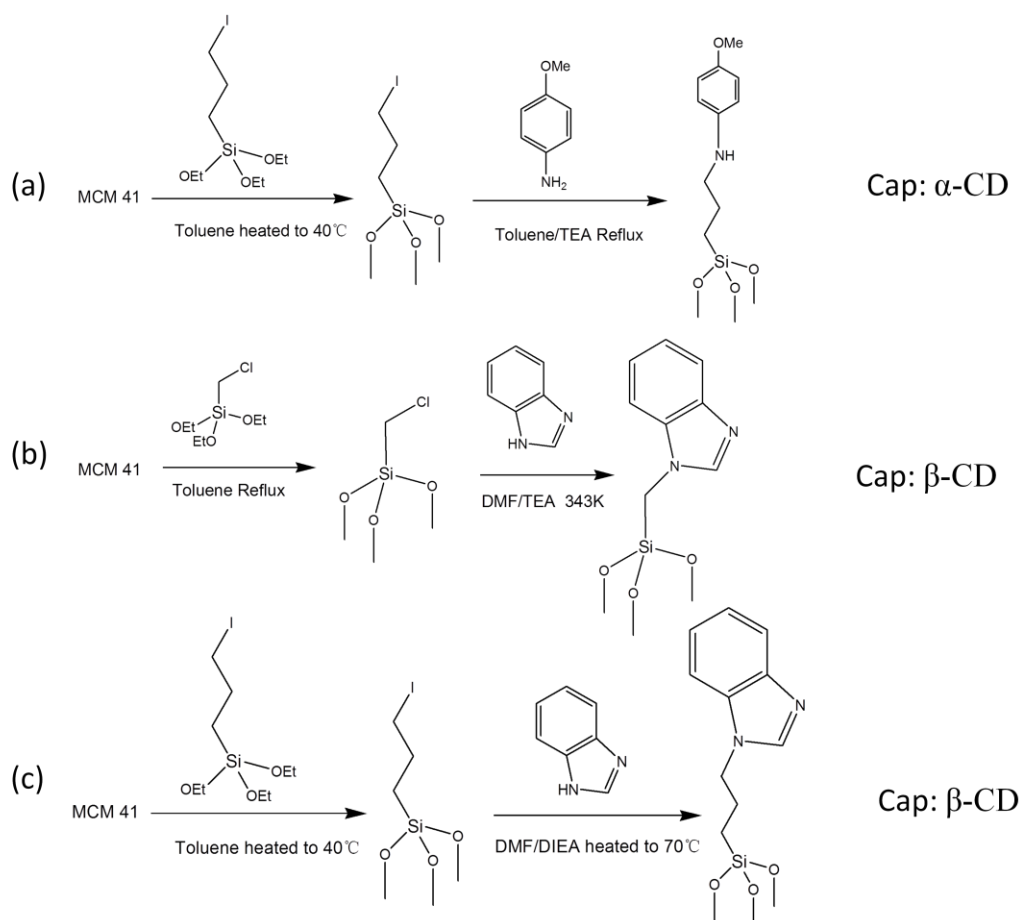


Figure 2.14. Synthesis of three pH-sensitive nanovalves (a) aniline alkane nanovalve,

(b) 1-Methyl-1H-benzimidazole (MBI) Nanovalve and (c)

(1-Propyl-1H-benzimidazole (PBI)) Nanovalve

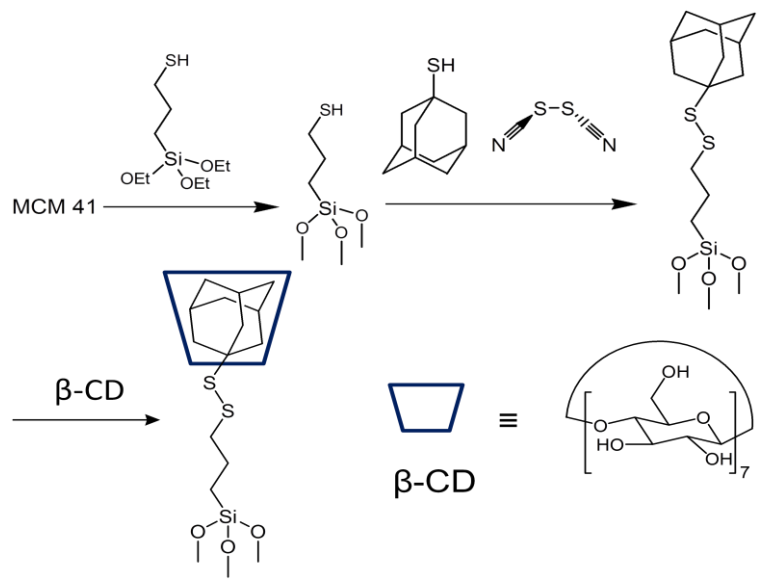


Figure 2.15. Synthesis of disulfide snap-top and capping with  $\beta\text{-CD}$

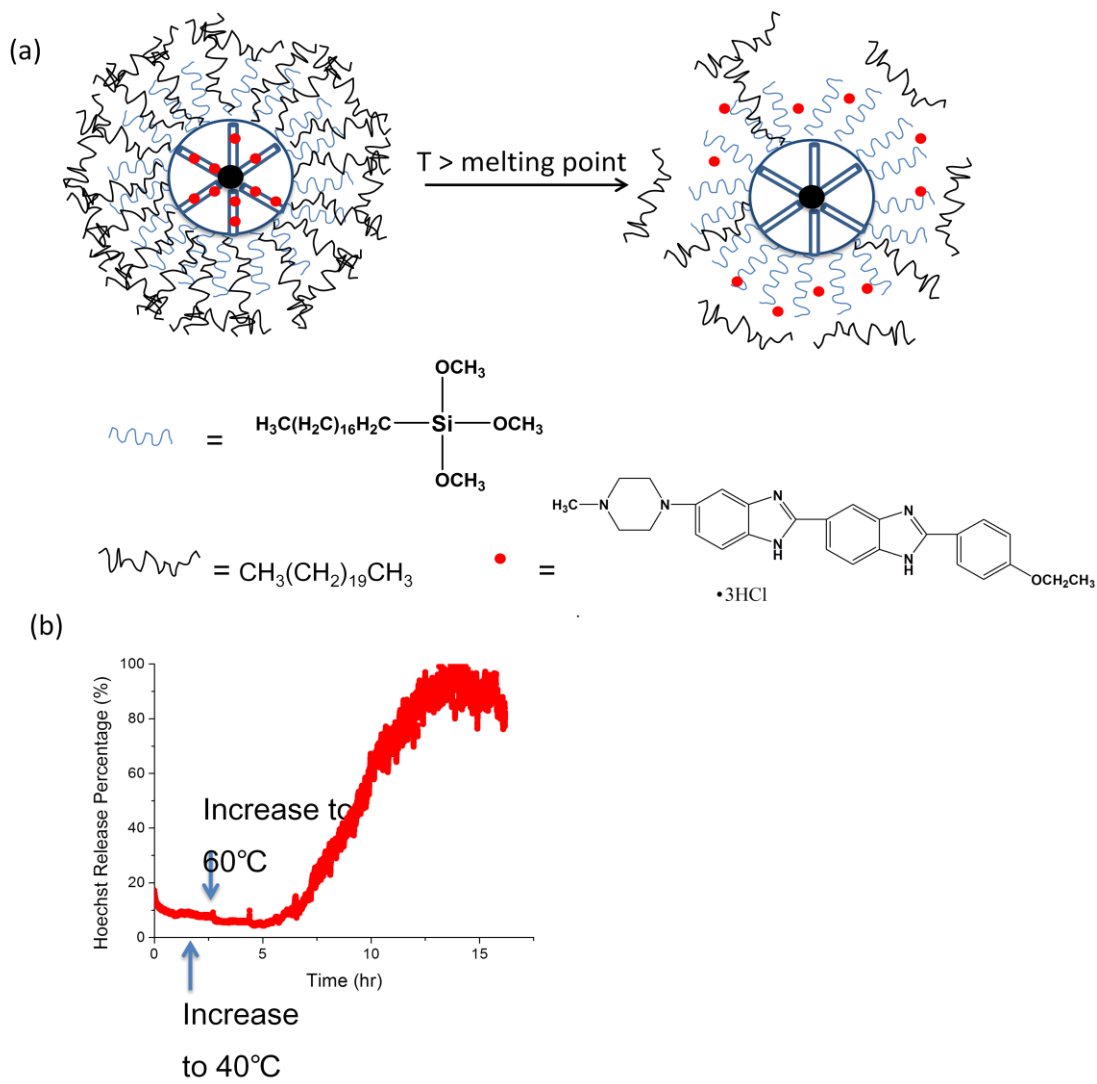


Figure 2.16 (a) The particles are functionalized with octadecyltrimethoxysilane and

coated with heneicosane to trap the Hoechst dye inside the pores. When temperature is increased above the melting point of the paraffin, the coating layer dissociates from the particle and dye is released. (b) The gated particles were dispersed in water and heated up to 40 °C at 1<sup>st</sup> hour, and there is no obvious release. After another 1.5 hours, further increase of temperature to 60 °C leads to a significant release from the particle. There is a response delay which is caused by the diffusion of hydrophobic paraffin in aqueous solution.

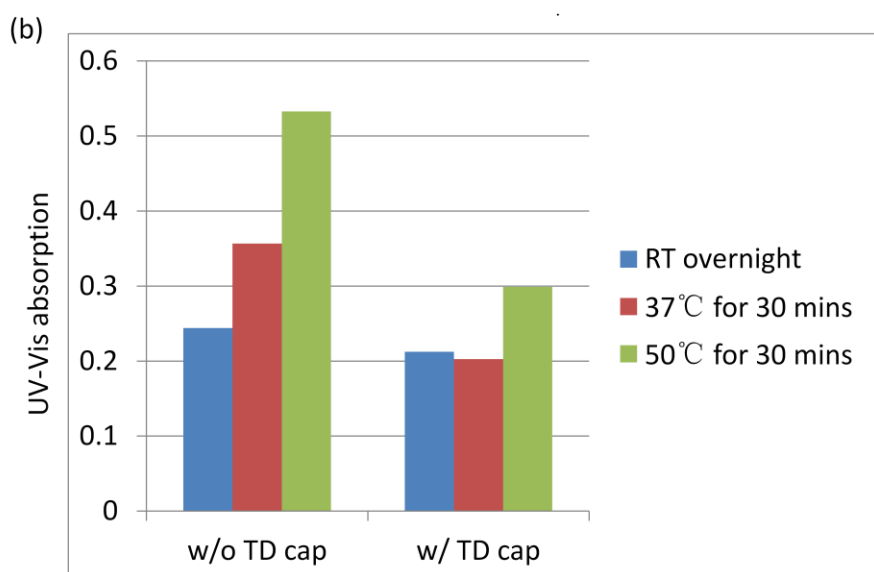
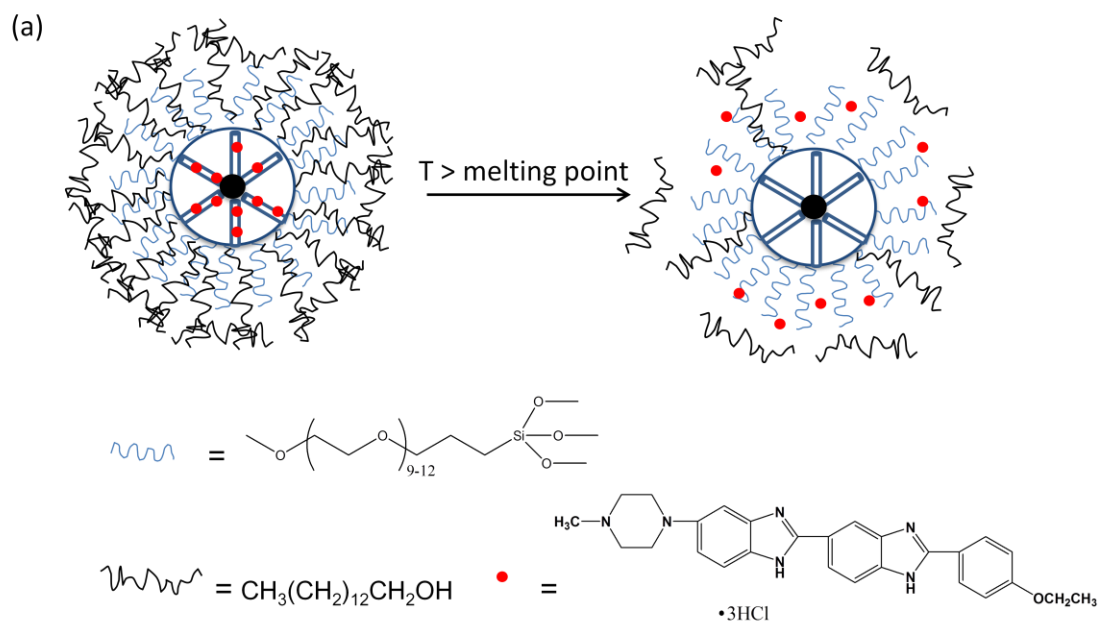




Figure 2.17. (a) 2-[methoxy(polyethyleneoxy)9-12propyl]trimethoxysilane was attached onto the particle, and 1-tetradecanol was used as capping material over the pores. When the surrounding temperature is higher than the melting point of 1-TD 39 °C, dye/drug can be released from the pores. (b) Capped functionalized particles exhibit no release at room temperature and 37 °C, while there is a slight release at 50 °C. In contrast, particles without the 1-TD cap have obvious releases at 37 °C and 50 °C.

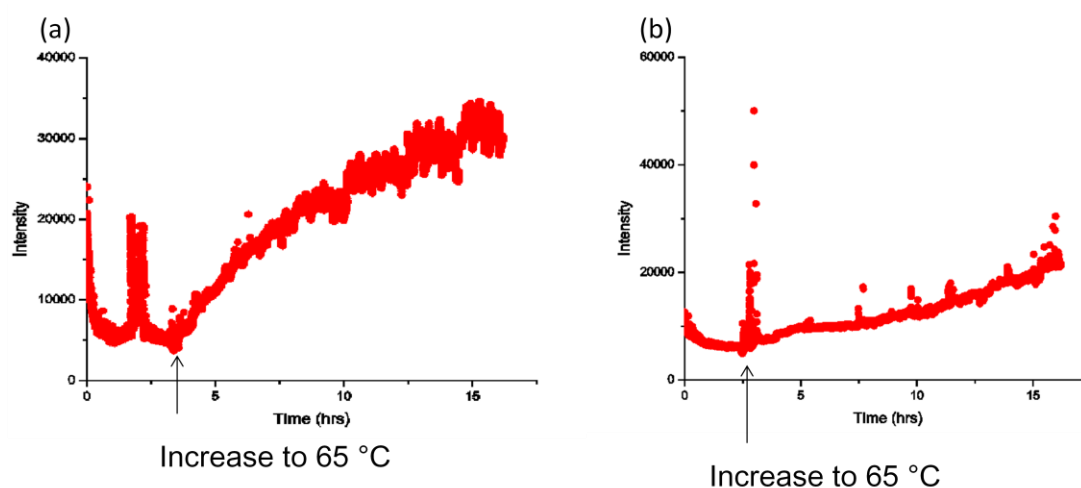
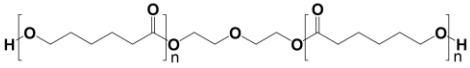
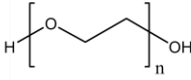


Figure 2.18. Particle coated with polycaprolactone diol (a) and polyethylene glycol (b) release Hoechst at 65 °C.

Table 2.1. Thermal-sensitive polymers and linkers to functionalize MSNs

Polymer	Linker	Softening point	Molecular Weight
<p>Polycaprolactone diol</p> 	3-(Triethoxysilyl)propyl-isocyanate	55 °C	2000
<p>Polyethyleneglycol</p> 	3-(Triethoxysilyl)propyl-isocyanate	45-50 °C	1400-1600

## 2.4 References

1. Liong, M.; Angelos, S.; Choi, E.; Patel, K.; Stoddart, J. F.; Zink, J. I. Mesoporous multifunctional nanoparticles for imaging and drug delivery. *J Mater Chem* 2009, 19, 6251-6257.
2. Li, Z. X.; Barnes, J. C.; Bosoy, A.; Stoddart, J. F.; Zink, J. I. Mesoporous silica nanoparticles in biomedical applications. *Chem Soc Rev* 2012, 41, 2590-2605.
3. Kim, J.; Kim, H. S.; Lee, N.; Kim, T.; Kim, H.; Yu, T.; Song, I. C.; Moon, W. K.; Hyeon, T. Multifunctional Uniform Nanoparticles Composed of a Magnetite Nanocrystal Core and a Mesoporous Silica Shell for Magnetic Resonance and Fluorescence Imaging and for Drug Delivery. *Angew Chem Int Edit* 2008, 47, 8438-8441.
4. Suzuki, K.; Ikari, K.; Imai, H. Synthesis of silica nanoparticles having a well-ordered mesostructure using a double surfactant system. *J Am Chem Soc* 2004, 126, 462-463.
5. Meng, H.; Xue, M.; Xia, T.; Ji, Z. X.; Tarn, D. Y.; Zink, J. I.; Nel, A. E. Use of Size and a Copolymer Design Feature To Improve the Biodistribution and the Enhanced Permeability and Retention Effect of Doxorubicin-Loaded Mesoporous Silica Nanoparticles in a Murine Xenograft Tumor Model. *Acs Nano* 2011, 5, 4131-4144.
6. Thomas, C. R.; Ferris, D. P.; Lee, J. H.; Choi, E.; Cho, M. H.; Kim, E. S.; Stoddart, J. F.; Shin, J. S.; Cheon, J.; Zink, J. I. Noninvasive Remote-Controlled Release of Drug Molecules in Vitro Using Magnetic Actuation of Mechanized

- Nanoparticles. *J Am Chem Soc* 2010, 132, 10623-10625.
7. Meng, H. A.; Xue, M.; Xia, T. A.; Zhao, Y. L.; Tamanoi, F.; Stoddart, J. F.; Zink, J. I.; Nel, A. E. Autonomous in Vitro Anticancer Drug Release from Mesoporous Silica Nanoparticles by pH-Sensitive Nanovalves. *J Am Chem Soc* 2010, 132, 12690-12697.
  8. Lu, J.; Liong, M.; Zink, J. I.; Tamanoi, F. Mesoporous silica nanoparticles as a delivery system for hydrophobic anticancer drugs. *Small* 2007, 3, 1341-1346.
  9. Du, L.; Liao, S. J.; Khatib, H. A.; Stoddart, J. F.; Zink, J. I. Controlled-Access Hollow Mechanized Silica Nanocontainers. *J Am Chem Soc* 2009, 131, 15136-15142.
  10. Xue, M.; Zhong, X.; Shaposhnik, Z.; Qu, Y. Q.; Tamanoi, F.; Duan, X. F.; Zink, J. I. pH-Operated Mechanized Porous Silicon Nanoparticles. *J Am Chem Soc* 2011, 133, 8798-8801.
  11. Aznar, E.; Mondragon, L.; Ros-Lis, J. V.; Sancenon, F.; Marcos, M. D.; Martinez-Manez, R.; Soto, J.; Perez-Paya, E.; Amoros, P. Finely Tuned Temperature-Controlled Cargo Release Using Paraffin-Capped Mesoporous Silica Nanoparticles. *Angew Chem Int Edit* 2011, 50, 11172-11175.
  12. Choi, S. W.; Zhang, Y.; Xia, Y. N. A Temperature-Sensitive Drug Release System Based on Phase-Change Materials. *Angew Chem Int Edit* 2010, 49, 7904-7908.
  13. Moon, G. D.; Choi, S. W.; Cai, X.; Li, W. Y.; Cho, E. C.; Jeong, U.; Wang, L. V.; Xia, Y. N. A New Theranostic System Based on Gold Nanocages and Phase-Change Materials with Unique Features for Photoacoustic Imaging and Controlled Release. *J Am Chem Soc* 2011, 133, 4762-4765.
  14. Liu, J.; Detrembleur, C.; De Pauw-Gillet, M. C.; Mornet, S.; Vander Elst, L.;

Laurent, S.; Jerome, C.; Duguet, E. Heat-triggered drug release systems based on mesoporous silica nanoparticles filled with a maghemite core and phase-change molecules as gatekeepers. *J Mater Chem B* 2014, 2, 59-70.

## Chapter 3

Mesoporous Silica Nanoparticles with pH – Sensitive Nanovalves for Delivery of  
Moxifloxacin Provide Improved Treatment of Lethal Pneumonic Tularemia

### 3.1. Abstract

We have optimized mesoporous silica nanoparticles (MSNs) functionalized with pH-sensitive nanovalves for the delivery of the broad spectrum fluoroquinolone, moxifloxacin (MXF), and demonstrated its efficacy in treating *Francisella tularensis* infections both *in vitro* and *in vivo*. We compared two different nanovalve systems, positive and negative charge modifications of the mesopores, and different loading conditions – varying pH, cargo concentration, and duration of loading – and identified conditions that maximize both the uptake and release capacity of MXF by MSNs. We have demonstrated in macrophage cell culture that the MSN-MXF delivery platform is highly effective in killing *F. tularensis* in infected macrophages, and in a mouse model of lethal pneumonic tularemia, we have shown that the drug-loaded MSNs are much more effective in killing *F. tularensis* than an equivalent amount of free MXF.

### 3.2. Introduction

*Francisella tularensis* is a facultative intracellular bacterial pathogen that causes tularemia, a serious and potentially fatal disease.<sup>1</sup> Because *F. tularensis* has extraordinarily high infectivity, causes serious morbidity and mortality, is readily cultured on a large scale, is relatively easily dispersed, and was developed as a biological weapon during World War II by Japan and in the Cold War by both the U.S. and the former Soviet Union,<sup>2-4</sup> it is classified as a Tier 1 Select Agent. Pneumonic tularemia, the type of tularemia of greatest concern in a bioterrorist attack, has a very high morbidity with at least half the patients requiring hospitalization, and can be fatal, resolve slowly<sup>5</sup> or relapse<sup>6</sup> even in a setting where awareness is high and appropriate

treatment is available. Therefore modalities allowing more effective and rapid treatment of tularemia are needed. Nanoparticles are attractive as drug delivery platforms for tularemia treatment because the nanoparticles are avidly taken up by cells of the mononuclear phagocyte (reticuloendothelial) system - such cells are the primary host cells in which *F. tularensis* resides and multiplies. By releasing high concentrations of antibiotic in the host cells that are infected by *F. tularensis*, nanoparticles have the potential to have a greater efficacy than free drug while simultaneously limiting off-target toxicities. Nanoparticle delivery platforms also have the advantage of shielding the drug from metabolism and clearance, thereby providing more favorable pharmacokinetics than free drug.

Considerable research has been devoted to the use of MSNs for delivery of chemotherapeutic agents for cancer; relatively less has been devoted to their use for treating infectious diseases. In the case of nanotherapeutics for cancer, uptake by macrophages is a problem to be overcome. In contrast, for infectious diseases caused by pathogens that reside and multiply within macrophages, such as *F. tularensis*, the fact that the host mononuclear phagocytes internalize nanoparticles more efficiently than other cells provides an advantageous targeting strategy with potential to increase efficacy and decrease systemic toxicities. Intravenously injected nanoparticles, or nanoparticles delivered by other routes of administration, are preferentially taken up by macrophages of the mononuclear phagocyte system and accumulate in liver, spleen and lung,<sup>7-9</sup> a distribution that mirrors the tissues infected by *F. tularensis* and many other important intracellular pathogens that cause serious human diseases, including



those that cause tuberculosis, Legionnaires' disease, Q-fever, Salmonellosis, Listeriosis, Leishmaniasis, and chlamydial, mycoplasmal, and rickettsial infections.

Mesoporous silica nanoparticles (MSNs) offer a biocompatible multifunctional platform with intrinsically high surface area and porosity capable of delivering chemotherapeutic agents and antibiotics.<sup>10-13</sup> MSNs readily accommodate stimulus-responsive functionalizations to enable on-command release of drug cargo in response to a variety of stimuli, including pH,<sup>14-17</sup> light,<sup>18</sup> and remote magnetic actuation,<sup>19</sup> and have shown superiority over free drug both in cell culture,<sup>20-22</sup> and in animal models.<sup>23</sup> An important parameter that influences the amount of MSNs that must be administered to animals or humans for therapeutic efficacy is the “release capacity”, defined as the ratio between the masses of releasable drug and of silica. The uptake and release capacity of a MSN platform depends on the properties of both the nanoparticles and the cargo molecules, including the cargo molecule size, charge in various solutions, and hydrophilic/hydrophobic properties. Herein we have systematically optimized moxifloxacin (MXF) loading of MSNs functionalized with pH sensitive nanovalves. We have studied two different pH sensitive nanovalve systems, both of which remain closed at the pH of blood (7.4) but open at pH 6 or lower and release cargo within endosomal compartments, which acidify to pH ~5 or less. We chose the most promising MSN-nanovalve platform for further optimizations based upon physical and chemical properties of MSNs and MXF.

Here, we report the optimization of our MSNs functionalized with pH-sensitive nanovalves for delivery of the fluoroquinolone antibiotic MXF, which

has been shown to be more effective than Ciprofloxacin at preventing relapse of tularemia in a mouse model.<sup>24</sup> We demonstrate that our optimized delivery platform, MSN-MBI-MXF, is safe *in vivo* and much more efficacious than an equivalent amount of free drug in treating *F. tularensis* infection in a mouse model of pneumonic tularemia.

### 3.3. Results and Discussion

#### 3.3.1. Construction of Two pH-sensitive Nanovalve Systems

We have previously developed two pH-sensitive nanovalve systems based on the MCM-41 framework.<sup>15, 25</sup> Both nanovalves consist of a stalk covalently attached to the pore entrances of MCM-41 and a cap molecule cyclodextrin (CD), which interacts with the organic moiety of the stalk through hydrophobic-hydrophobic interaction and traps the cargo inside the pores. The first nanovalve is composed of an anilinoalkane (ANA) stalk and  $\alpha$ -CD as the capping molecule. The  $pK_a$  of the nitrogen of p-anisidine is approximately 6, and at pH 7.4 the binding affinity between  $\alpha$ -CD and the hydrophobic stalk is high. When the stalk is protonated the binding constant dramatically decreases, thereby causing the  $\alpha$ -CD cap to dissociate from the stalk and the cargo to be released. The second nanovalve system has a 1-methyl-1-H-benzimidazole (MBI) stalk with  $pK_a$  about 6, and  $\beta$ -CD as the capping molecule because of its suitable cavity size and stable association with the benzimidazole moiety at physiological pH 7.4 (Figure 3.1). When benzimidazole is protonated at pH 6 or lower, the binding affinity between benzimidazole and  $\beta$ -CD decreases, leading to dissociation of the cyclodextrin. Both nanovalves are closed

tightly at physiological pH 7.4 and only open and release cargo at pH 6 and lower when the hydrophobic interaction between cyclodextrin and the organic stalk moiety is weakened and interrupted.

After the stalks were attached to MCM-41, the MSN-ANA and MSN-MBI nanoparticles were loaded in MXF aqueous/PBS solution overnight and then the  $\alpha$ -CD or  $\beta$ -CD capping molecule, respectively, was added to the mixture with stirring overnight. The MXF solution concentrations before and after loading were measured and calculated based on UV-Vis spectroscopy measurements. The amount of MXF taken up by the MSNs (including inside pore channels and on external surfaces) was calculated from this concentration difference. The mass of MXF taken up by the MSNs divided by their mass is defined as “uptake capacity” (expressed in wt %). After washing the mechanized MSNs sufficiently to remove MXF on the outer surface, the nanoparticles were dispersed in neutral water, and then acid was added to decrease the pH and release the drug (Figure 3.2A). When MSNs were placed at the corner of a cuvette in neutral solution, no MXF was detected in the supernatant fluid by fluorescence measurement. When the solution pH was adjusted to 6 by adding HCl, immediate release of MXF was observed (Figure 3.2B). It is known that the pH within the lysosome is lower than 6; thus, the nanoparticles should release the drug after being endocytosed into the lysosome compartment. This drug would then be available to diffuse to *F. tularensis*, which resides and replicates in the cytosol of the cell,<sup>26</sup> where the pH is neutral. The amount of MXF released was calculated based on the supernatant MXF concentration measured by UV-Vis. The mass of released MXF

divided by the mass of particle is defined as “release capacity” (expressed in wt %). The porous structure is preserved after these modifications (Figure 3.2C) and the hydrodynamic diameter is around 100 nm.

### **3.3.2. Enhancement of Uptake Capacity by Charge Modification of the Mesopore Channels**

To optimize the uptake and release capacities, we must consider five relevant factors: charges of cargo molecules and MCM-41 inner pore channels, nanovalve synthesis pathway, loading solvent pH, MXF concentration and loading time. MSNs with the MBI stalks (MSN-MBI) were selected as the initial model; when investigating the effects of one factor on the uptake and release capacities, all of the other parameters were kept constant.

MXF is a fourth generation fluoroquinolone used to treat various bacterial infections including *F. tularensis*. It has two ionizable groups with  $pK_a$  of 6.3 and 9.3. Based on the calculation of the molecular species distribution, at pH 7, 83.3% of MXF molecules are zwitterionic, 17% are positively charged, and almost none are negatively charged (Table 3.1). MXF has a positive net charge at neutral pH. A negatively modified inner pore readily attracts positive cargo molecules, but the release may be slow and incomplete after the cap dissociates due to the electrostatic interaction between cargo molecules and inner pores at the pH of acidifying endosomal compartments.<sup>27</sup> On the other hand, a positively charged inner pore surface will lead to lower uptake capacity than when negatively charged but may promote expulsion of the positive cargo molecules upon protonation. To modify the

MSN inner pores with either negative or positive charges, we synthesized MCM-41 with co-condensation of phosphonate or amine silanes respectively (Figure 3.3A). Phosphonate silane-modified MSNs exhibited a zeta potential of -46.28 mV and amine-silane modified MSNs exhibited a zeta potential of 38.76 mV as measured in DI water. MSN-MBI (10 mg) was dispersed in 2 ml of a 5 mM MXF aqueous solution and uptake capacity was measured as described above. Amine modified MSN-MBI (indicated as “+”) had a very low uptake capacity compared with that of phosphonate modified MSN-MBI (indicated as “-”) (Figure 3.3B). This result indicates that MXF with a positive net charge diffuses poorly into positively charged inner mesopores, resulting in very low uptake and release capacities. Phosphonated particles, on the other hand, show much greater uptake of MXF, potentially providing a much greater release capacity.

We next tested two different MBI stalk synthetic pathways to optimize the efficiency of attachment. In the first pathway, we first reacted benzimidazole with chloromethyltrimethoxysilane to produce the MBI stalk, and then covalently attached this to the MCM-41 surface. This method has the disadvantage that, in the presence of small amounts of water or moisture, the MBI stalk readily hydrolyses and undergoes self-condensation prior to coupling to the nanoparticle. In the second pathway, we covalently attached chloromethyltrimethoxysilane to the silica surface first and then coupled it with benzimidazole to form the MBI stalk. We compared the uptake capacities of negatively charged MSN-MBI nanoparticles prepared by these two pathways and found that MBI stalk attachment by pathway II had a higher uptake

capacity than attachment by pathway I, consistent with greater MSN surface coverage by the MBI stalks and hence greater trapping of drug in the pore channels.

### 3.3.3. Uptake and Release Capacity Utilizing Different Nanovalves

Both MSN-ANA and MSN-MBI were tested and proven to work effectively in our previous papers when loaded with doxorubicin, Hoechst 33342, or propidium iodide (PI).<sup>15, 25</sup> However, we know that the uptake capacity and release capacity of the MCM-41 nanovalve system is dependent upon the size and charge of the cargo molecule, as well as the length of the stalk and the outer diameter of the CD. We measured and compared the uptake capacity of MXF utilizing these two systems in order to find the best one for subsequent *in vitro* and *in vivo* studies.

Because negatively charged inner pores provided greater uptake of MXF, we used phosphonated MCM-41 and compared the uptake and release of MXF of MSN-ANA-MXF, which has  $\alpha$ -CD as cap, and MSN-MBI-MXF which has  $\beta$ -CD as cap. The same amount of phosphonated MCM-41 with one or the other nanovalve was loaded in 1 ml 10 mM MXF PBS solutions and stirred for one day. MSN-MBI-MXF had a much higher uptake capacity (7.4 wt%) and release capacity (1.02 wt%) than MSN-ANA-MXF (Table 2). The superior uptake and release capacity of the MSN-MBI-MXF is likely attributable to better trapping of the MXF within the pores. The  $\beta$ -CD has a 15.6 Å outer diameter compared with 14.6 Å for  $\alpha$ -CD while MCM-41 has an average pore diameter of 22 Å.<sup>15</sup> The larger  $\beta$ -CD has more steric hindrance and blocks the MSN pores more effectively than the smaller  $\alpha$ -CD. Moreover MSN-MBI has a shorter stalk length that positions the  $\beta$ -CD cap

closer to the MSN surface, again providing more effective steric hindrance to prevent MXF leakage. For both types of MSNs, the uptake capacity was greater than the release capacity in aqueous acid, indicating that some MXF remains bound to the MSNs and is not released in aqueous acid conditions, possibly reflecting binding of MXF to MSN *via* hydrophobic interactions.

#### **3.3.4. Uptake of MSN with pH Sensitive Nanovalves by Human Macrophages**

Nanoparticles are generally taken up well by cells of the mononuclear phagocyte system and, where this is not desired, require special surface modifications to minimize their uptake by macrophages in applications such as cancer therapeutics.<sup>28</sup> However, in our system, uptake by macrophages is desired, since *F. tularensis* replicates in host mononuclear phagocytic cells. Our MSN platform is designed to operate by uptake of the particles by macrophages, followed by release of drug within acidified endo-lysosomal compartments. To determine whether our MSNs are internalized by *F. tularensis*-infected macrophages, we examined the uptake of rhodamine-labeled MSNs by *F. tularensis*-infected human macrophages, using both peripheral blood monocyte-derived macrophages and differentiated macrophage-like THP-1 cells. We observed abundant uptake of MSN-MBI-MXF for both the monocyte-derived macrophages and the differentiated THP-1 cells (Figure 3.4). Uptake of the nanoparticles by both types of macrophages increased with time and with nanoparticle concentration.

#### **3.3.5. *In Vitro* Efficacy of MSN-ANA-MXF and MSN-MBI-MXF in Killing *F. tularensis* in Human Macrophages.**

To investigate whether these two different types of pH-sensitive  $\alpha$ - and  $\beta$ -CD nanovalves are functional under biological conditions, we assessed the efficacy of MSN-ANA-MXF and MSN-MBI-MXF in a macrophage infection model of *F. tularensis*.<sup>29</sup> Differentiated human THP-1 macrophages were infected with *F. tularensis* Live Vaccine Strain (LVS) and either not treated or treated with increasing concentrations of a) MXF, b) MSN-ANA-MXF, or c) MSN-MBI-MXF for one day. At the end of the treatment period, the number of viable bacteria remaining in the macrophages was determined to evaluate the *F. tularensis* killing effect exerted by each treatment. With no treatment, *F. tularensis* LVS grew 2.5 logs over one day. Similar levels of bacterial growth were also observed in infected macrophages treated with control MSNs (no MXF loading) indicating that the nanoparticle carriers alone do not possess any bactericidal activity (Figure 3.5B and C). All treatments including MXF, MSN-ANA-MXF and MSN-MBI-MXF killed *F. tularensis* in macrophages in a dose- dependent manner (Figure 3.5A, B and C). However, when compared at the same concentration, MSN-MBI-MXF was much more potent than MSN-ANA-MXF in killing *F. tularensis*. For example, MSN-MBI-MXF at 1  $\mu\text{g}/\text{mL}$  reduced bacterial colony forming units (CFU) by 3.4 logs compared with the level in the untreated group at one day, whereas the same concentration of MSN-ANA-MXF reduced bacterial CFU by only 0.2 logs compared with the untreated control group. The minimal inhibitory concentration in our macrophage assay is 4  $\mu\text{g}/\text{mL}$  for MSN-ANA-MXF and it falls to between 0.25 and 0.5  $\mu\text{g}/\text{mL}$  for MSN-MBI-MXF.



We prepared supernate from MSN-ANA-MXF and MSN-MBI-MXF after an hour of incubation with 100 mM maleic acid, pH 1.8 (Acid Release) and assayed its capacity to kill *F. tularensis* in the infected macrophage. While the acid-released solution prepared from 0.5 and 1  $\mu\text{g}/\text{mL}$  MSN-MBI-MXF reduced *F. tularensis* CFU in macrophages by 1.6 and 2.5 logs, respectively, the solution prepared from 1  $\mu\text{g}/\text{mL}$  of MSN-ANA-MXF reduced bacterial number by only 0.2 logs (Figure 3.5D and E). Supernates obtained from MSN-MBI-MXF or MSN-ANA-MXF at neutral pH (Neutral Eluate) had no effect in the infected macrophage bioassay. This study demonstrates that 1) the pH operative valves on MSN-MBI-MXF are tightly closed at neutral pH and open at acidic pH, 2) MXF eluted under acidic pH retains biological activity, 3) MSN-ANA-MXF and MSN-MBI-MXF kill *F. tularensis* LVS in macrophages in a dose-dependent fashion, and 4) MSN-MBI-MXF has greater efficacy than MSN-ANA-MXF, most likely because of its higher MXF uptake and release properties.

Acid-released solution obtained from 1  $\mu\text{g}/\text{mL}$  of MSN-MBI-MXF exerted the same inhibitory effect on *F. tularensis* as 0.016  $\mu\text{g}/\text{mL}$  MXF in our macrophage bioassay, indicating a 1.6% (wt/wt) aqueous acid release capacity. Based on this estimation, 0.5  $\mu\text{g}/\text{mL}$  of MSN-MBI-MXF could release 0.008  $\mu\text{g}$  of MXF in the acidified endolysosomes. In our *F. tularensis*-infected macrophage assay, MSN-MBI-MXF at 0.5  $\mu\text{g}/\text{mL}$  had a biological effect equivalent to that exerted by free MXF at a concentration of 0.016  $\mu\text{g}/\text{mL}$ , indicating an efficacy ratio of 2 (MSN-MBI-MXF : free MXF), as nanoparticle-delivered drug appeared to have an

efficacy twice that of the same amount of free drug in killing *F. tularensis* in macrophages *in vitro*. However, this efficacy ratio is likely an over-estimation since some of the yellowish color of MXF still remained on MSN-MBI-MXF after maleate treatment. In lieu of a possible hydrophobic interaction between MXF and MSN, we used acidic DMSO solution for measuring drug release capacity in subsequent *in vivo* studies.

### **3.3.6. Maximization of Uptake and Release Capacity by Optimization of Loading pH**

Our *in vitro* study indicated that it is important to obtain a high release capacity in order to achieve high efficacy. Therefore we sought to increase further the uptake and release capacities of MSN-MBI-MXF.

Specifically, we prepared MXF in different pH solutions for use in the loading process to take advantage of electrostatic interactions based on positively or negatively charged inner pore channels. It is known that MXF has a positive net charge below pH 7.4 and negative net charge above pH 7.4 (Table 3.1). Therefore we loaded phosphonate modified MSN-MBI (10 mg) (indicated as “-”) in pH 4 and pH 7 MXF solution (5 mM, 2 ml) in order to attract positive MXF molecules and increase uptake capacity. However, this acid loading presents some practical problems in experiments. The pH 4 loading helps improve uptake capacity as expected. However, it results in lower release capacity than neutral loading. Because the nanovalve can open at pH 6, loaded MSN-MBI must be transferred to neutral solution before capping. The additional steps of centrifugation and dispersion of uncapped

MSN-MBI-MXF in neutral water cause significant leakage of MXF from the particle pores before capping can be completed. We loaded amine modified MSN-MBI (10 mg) (indicated as “+”) in pH 7, 10, and 12 MXF solutions (5 mM, 2 ml) to attract negative MXF molecules. We observed that uptake capacities as well as release capacities increased as pH was increased (Figure 3.6). Among these five conditions of loading, amine modified MSN-MBI in pH 12 loading gave the highest uptake capacity; however, the release capacity was still no better than pH 7 loading with phosphonate modified MSN-MBI. Using a pH 12 loading solution may gradually degrade the MSNs within 24 hours and cause stalks to detach from the pores, enabling MXF to leak out of the pores during washing.

We found that loading phosphonated MSN-MBI with MXF in pH 7.4 PBS yielded the highest uptake and release capacity among all conditions (Figure 3.7). When phosphonate modified MSN-MBI (10 mg) was loaded in 1 ml 20 mM MXF in PBS (pH 7.4), its uptake capacity increased more than 10 times compared with its loading in neutral solution. Considering stalk protonation and deprotonation equilibrium, MSN-MBI is more tightly closed with  $\beta$ -CD at pH 7.4 than it is at pH 7. Negatively charged mesopores also have strong electrostatic interaction with positive MXF molecules. Moreover, compared with strong base, the pH 7.4 loading solution will not cause hydrolysis of silica nanoparticles and degradation of the nanovalves attached at the entrances of pore channels. All of these factors contribute to the highest uptake capacity.

We have found that a higher MXF loading concentration resulted in a higher uptake and release capacity. MSN-MBI loaded with 40 mM MXF in PBS had an uptake capacity twice that of MSN-MBI loaded with 20 mM MXF in PBS, and the release capacity reached 8.1 wt% compared with 6.2 wt% for MSN-MBI loaded with 20 mM MXF. Moreover, when we compared uptake efficiency, which is defined as the percentage of MXF taken up by MSN from the original solution (expressed in percent), almost 70% of MXF in high concentration solution was taken up by nanoparticles. We also observed that a loading time of 24 hours was appropriate to allow MXF to diffuse into pore channels and reach equilibrium. Simply extending loading time did not increase uptake and release capacity. We tested phosphonated MSNs modified with two different nanovalves (ANA, MBI); the MSNs were loaded in MXF in PBS at low concentration (10mM) and washed extensively with PBS buffer. The MSN-ANA and MSN-MBI showed uptake and release capacities of 20 wt% / 0.24 wt% and 51.4 wt% / 1.6 wt%, respectively; therefore MSN-MBI still showed the best performance in the final optimized condition (Table 3). In conclusion, phosphonated MSN-MBI loaded with MXF in PBS showed the highest release capacity, 6 – 8 wt%, among all systems tested; this was highly reproducible and this MSN loaded with MXF in PBS was employed in subsequent *F. tularensis in vitro* and *in vivo* studies.

### **3.3.7. Influence of Washing on Release Capacity**

In the washing process, the mass of MXF washed away each time divided by the mass of particle is defined as “residual” (expressed in wt %), of which the final

residual is reflected as the starting baseline in a release profile. Through measurement by UV-Vis spectroscopy, the amount of residual drug in supernatant did not increase after dispersing and rotating particles in neutral water overnight, which indicated that the residual was not due to release or leakage, but caused by non-trapped MXF dissociating from the MSN-MBI-MXF surface. In the release process, we dispersed particles in neutral deionized water and observed no leakage from MSN-MBI as indicated by the flat baseline in the release profile. After adding HCl to adjust the pH to 5, we measured an immediate increase in fluorescence intensity from the MXF released into the supernatant. The release profile reached a plateau after 14 hours, and the concentration of completely released MXF was measured by UV-Vis spectroscopy after 24 hours.

We investigated how the washing process influences particle release capacity. In testing drug-loaded nanoparticles, we routinely wash them to remove free MXF adsorbed on the external surface of the MSN to insure that the great majority of the drug is released *via* the nanovalves. However, excess washing will gradually degrade the silica nanoparticle surface due to siloxane group hydrolysis. Moreover, it will remove some of the cyclodextrin caps by disrupting host-guest interaction equilibrium. Therefore, it is important to determine the optimal number of washing steps that strikes an acceptable balance between removing MXF from the external surface and maintaining relatively high release capacity. MSNs washed 15 times did not have any residual surface MXF detectable by UV-Vis absorption measurement (Figure 3.8A); however, their release capacity was only 1.6 wt%. In contrast, MSNs washed 8

times had 2.5 wt% residual and 6.9 wt% release capacity. MSN-MBI-MXF washed 21 times had almost zero residual in the last few washes. There is a non-linear decay of the amount of MXF washed away each time, with the first 8 washes removing around 95 % of the total amount of MXF (Figure 3.8B). We found that washing 8 times is enough to remove most of the MXF on the MSN external surface and at the same time constrain damage to surface modifications.

### **3.3.8. *In Vivo* Efficacy of MSN-MBI-MXF in Treating Pneumonic Tularemia**

It is important to test nanoparticle delivery systems *in vivo* as well as *in vitro*. Nanoparticles that are effective in an *in vitro* system may fail in an *in vivo* model due to issues of efficacy, such as inadequate uptake by target organs or premature release of drug, and issues of toxicity, e.g. due to induction of coagulopathy,<sup>30</sup> hemolysis,<sup>31</sup> organ toxicities or inflammatory responses.<sup>32</sup> After the above optimizations of our MSNs so as to achieve high uptake and release capacity, we assessed the efficacy of MSN-MBI-MXF in a mouse model of pneumonic tularemia.<sup>33, 34</sup> In the first *in vivo* experiment (Experiment 1), mice were infected by the intranasal route with ~8000 CFU of *F. tularensis* LVS, a dose approximately 11 times the LD<sub>50</sub> of 700 CFU. Without treatment, the mice succumbed rapidly to the infection and suffered severe weight loss (Figure 3.9A). Mice treated with MSN-MBI-MXF (with a drug release capacity of 6.88 wt%) maintained their weight, indicating that the nanoparticle was well tolerated by the mice and helped to control the severe bacterial infection. Without treatment, bacteria multiplied to high numbers in the lungs of the mice (Figure 3.10A). However, treatment with MSN-MBI-MXF (loaded with 138 µg MXF)

reduced bacterial burden in the lung by 4.0-logs, more so than treatment with 400  $\mu\text{g}$  of free MXF (Figure 3.10C). Treatment with MSN-MBS-MXF reduced bacterial burden in the spleen by 4.3-logs to a level similar to that with 400  $\mu\text{g}$  of free MXF which was below our experimental limit of detection. All treatments reduced bacterial burden in the liver to a level below the experimental detection limit. On the basis of a median-effect plot, the efficacy of the MSN-MBI-MXF was 4.5 fold and 3 fold the efficacy of free MXF in the lung and spleen, respectively. This study demonstrates that MSN-MBI-MXF administered intravenously is much more efficacious than free MXF in treating *F. tularensis* infection in mice.

In a subsequent *in vivo* experiment (Experiment 2), we evaluated another batch of MSN-MBI-MXF (with a drug release capacity of 8.08 wt%). Mice were infected with  $\sim 4000$  CFU of *F. tularensis* LVS ( $\sim 6 \times \text{LD}_{50}$ ) by the intranasal route. One day later, mice were sham-treated or treated with 640  $\mu\text{g}$  of MSN-MBI-MXF (with  $\sim 50$   $\mu\text{g}$  of releasable MXF) or with one of the three doses of MXF (50, 100, and 200  $\mu\text{g}$ ) equal to 1x, 2x, and 4x the amount of the releasable MXF from 640  $\mu\text{g}$  of MSN-MBI-MXF by acidic DMSO. As observed in the first *in vivo* study, sham treated mice suffered substantial weight loss but mice treated with free MXF or MSN-MBI-MXF did not (Figure 3.9B). MSN-MBI-MXF treatment reduced the bacterial burden by 2.8 logs in the lung, 3.2 logs in the liver, and 3.3 logs in the spleen to a level close to that achieved by 100  $\mu\text{g}$  free MXF (Figure 3.10D). Thus, in the treatment of pneumonic tularemia in mice, MSN-MBI-MXF had an efficacy twice the equivalent amount of free MXF in the lung, spleen, and liver. Again, we observed no toxicity in the mice

from MSN-MBI-MXF treatment. Thus, these two experiments both demonstrated superiority of MSN-MBI-MXF over an equivalent amount of free MXF. In the first experiment, bacterial CFU were reduced in the lungs compared with that achieved by free drug, and the difference was statistically significant; comparisons in liver and spleen could not be made because sterilization was achieved at the doses used for all treatments. In the second experiment, we reduced the dose of MSN-MBI-MXF to prevent “bottoming out” of the values in the liver and spleen and showed that the MSN-MBI-MXF treatment reduced bacterial CFU more than an equivalent amount of free drug in these organs, a difference that was statistically significant. Bacterial burden in the lungs was also reduced more in the MSN-MBI-MXF treated animals than in animals treated with an equivalent amount of free drug, though this trend did not reach statistical difference at this lower dose of MSN-MBI-MXF.



### 3.4. Conclusion

Intracellular pathogens that reside in mononuclear phagocytes present an ideal target for nanotherapeutics because nanoparticles are readily taken up by cells of the Mononuclear Phagocyte System and have the potential to deliver high concentrations of antibiotics selectively to the intracellular compartment, thereby providing increased efficacy with reduced systemic exposure and off-target side effects.

We have optimized MSNs with pH-sensitive nanovalves for uptake and release of the antibiotic MXF. We evaluated a) two different pH-sensitive nanovalves; b) modification of the MSN's inner pores with positive or negative charges; c) loading of the MSNs with MXF in different pH solutions; and d) loading MSNs with different drug concentrations and loading durations. We found that phosphonated MSN-MBI-MXF loaded in pH 7.4 PBS gave the highest uptake and release capacity. We demonstrated that this delivery system released MXF efficiently in *F. tularensis*-infected macrophages and that it was 2.7 fold more effective than the amount of free drug released from the particles by aqueous acid. We demonstrated in a mouse model of lethal pneumonic tularemia that MSN-MBI-MXF was well tolerated and was more effective than a 2- to 4-fold greater dose of free MXF in reducing bacterial load in the lung. Our MSN-MBI-MXF delivery system has the potential to provide more effective treatment than free drug, shortening the duration of treatment of intracellular infectious diseases such as tularemia, tuberculosis, Q-fever, and Legionnaires' disease and reducing systemic toxicity of the MXF. By providing high concentrations of antibiotic directly to the site of infection, the

nanoparticle delivered drug also has the potential to decrease the emergence of drug resistance. Further optimization of our platform may be possible by incorporation of additional functionalizations to increase targeting to infected tissues and macrophages, employment of different delivery modalities, such as aerosol delivery, or utilization of other internal and external stimulus-response systems.

### 3.5. Experimental Section

*Materials:* Cetyltrimethylammonium bromide (CTAB, 95%), tetraorthoethylsilicate (TEOS, 98%) 3-(trihydro-xysilyl)propyl methylphosphonate (42% in H<sub>2</sub>O), 3-iodopropyltrimethoxysilane (IPTMS, 95%), N,N'-dimethylformamide (99.8%), p-anisidine (99%),  $\alpha$ -cyclodextrin ( $\geq 98\%$ ),  $\beta$ -cyclodextrin ( $\geq 97\%$ ), benzimidazole (98%), tetrabutylammonium iodide (98%), Hoechst 33342 ( $\geq 97\%$ ), triethylamine ( $\geq 99\%$ ), and toluene (99.8%) were purchased from Sigma (St. Louis, MO). Chloromethyltrimethoxysilane (90%), and N-(2-Aminoethyl)-3-aminopropyltrimethoxysilane (NAPTS, 90 %) were purchased from Gelest (Morrisville, PA).

*Synthesis of MCM-41:* The synthesis of MCM-41 was based on well-established published procedures. Cetyltrimethylammonium bromide (CTAB, 250 mg, 0.7 mmol) was dissolved in H<sub>2</sub>O (120 mL) and NaOH (875  $\mu$ L, 2M). The mixture was heated up to 80 °C and kept stable for 30 minutes, followed by adding tetraethyl orthosilicate (TEOS, 1.2 mL) drop-wise into the solution while stirring vigorously. For phosphonated MCM-41, 3-(trihydroxysilyl)propyl methylphosphonate (315  $\mu$ L) was added into the solution 15 minutes after adding TEOS. For amine modified MCM-41,

N-(2-Aminoethyl)-3-aminopropyltrimethoxysilane (90 %) was mixed with TEOS before adding to CTAB solution. The solution was kept at 80 °C for 2 hours. The synthesized nanoparticles were centrifuged and washed thoroughly with methanol. The successful synthesis of nanoparticles is very sensitive to the temperature and stirring speed.

*Synthesis of Anilinoalkane (ANA) Nanovalve:* As-synthesized MCM-41 (100 mg) was washed and dispersed in anhydrous toluene, mixed with 3-iodopropyl trimethoxysilane (IPTMS, 20 µL, 0.1mmol) and heated up to 40 °C under N<sub>2</sub> for 12 hours. The IPTMS modified nanoparticles were washed with toluene to remove unreacted agents and re-dispersed in anhydrous toluene, and mixed with p-anisidine (123.2 mg, 1 mmol) and triethylamine (TEA, 420 µL, 3 mmol). The solution was refluxed under N<sub>2</sub> for another 24 hours. The final product was centrifuged and washed with toluene, methanol and water to be ready for drug/dye loading process.

*Synthesis of 1-Methyl-1H-benzimidazole (MBI) Nanovalve:* MCM-41 (100 mg) was washed and dispersed in anhydrous toluene, mixed with chloromethyltrimethoxysilane (15 µL) and refluxed for 12 hours. The modified MCM-41 was washed by toluene and dimethoxyformamide (DMF) and dispersed in 8 ml DMF. Tetrabutylammonium iodide (2 mg), benzimidazole (12 mg) and triethylamine (150 µL) were added into the solution and the mixture was heated up to 70 °C under N<sub>2</sub> for 24 hours. As-synthesized nanoparticles were washed with DMF, methanol and water thoroughly.

*Surfactant Template Extraction:* Nanovalve-modified MCM-41 (100 mg) was dispersed in methanol (60 mL), mixed with concentrated HCl (12 M, 2.3 mL) and refluxed for 8 hours under N<sub>2</sub>, and then washed extensively with methanol and water.

*Drug Loading and Washing:* 10 mg of nanovalve-modified MCM-41 was suspended in MXF PBS solution at various concentrations overnight.  $\beta$ -CD (40 mg) was added to the suspension and mixed for 12 hours to make sure the capping molecule reached an equilibrium with stalks on the nanoparticle surface. Loaded and capped nanoparticles (10 mg) were centrifuged down in a 2 mL tube and the supernate kept for UV-Vis absorbance measurement. Filtered PBS was added into the tube and nanoparticles were suspended and sonicated again. This washing process was repeated and the number of times the nanoparticles were washed was the same for each group being compared.

*Uptake Capacity and Release Capacity Measurement:* After measuring UV-Vis absorbance of MXF remaining in the PBS loading solution and of standard MXF PBS solution with known concentrations of 0.01 mM, 0.02 mM and 0.025 mM MXF, the amount of unloaded MXF concentration was calculated based on Beer's law. Uptake capacity (wt %) =  $[(W_{MXF} \text{ before loading} - W_{MXF} \text{ after loading}) / W_{particle}] \times 100 \%$ . In the optimization experiments, the loaded MSN-MXF particles were dispersed in pH 4.5 HCl solution for 24 hours and then centrifuged down to measure the concentration of MXF released into the supernate. Release capacity (wt %) =  $(W_{released \text{ MXF}} / W_{particle}) \times 100 \%$ . In our *in vitro* and *in vivo* studies of the

efficacy of the nanoparticles in treating *F. tularensis* infection, MSN-MXF was dispersed in pH 1 HCl/DMSO solution to measure the maximum release capacity.

*Stimulated Release Studies:* To measure MXF release from MSNs and detect MXF fluorescence emission in supernates, dried MSN-MXF powder was put in the corner of a glass vial containing 10 mL DI water. A probe laser beam (5 mW 377 nm) was passed through the supernatant fluid in the glass vial such that released MXF was excited. The fluorescence was detected and collected by a charge-coupled device (CCD) detector and a computer at 1 s intervals over the course of the experiment. Baseline spectra were collected for 1 hour to confirm that there was no MXF leakage, and then 1 M HCl solution was added to adjust the pH to 4.5. The release profile was the plot of the integrated emission peak area between 480 nm to 520 nm as a function of time.

*Physicochemical Characterization of Nanovalve Modified MSN:* Transmission electron microscopy (TEM) images of MSN were obtained using a JEM1200-EX (JEOL) instrument (JEOL USA, Inc., Peabody, MA). Particle size and zeta potential were measured by ZetaSizer Nano (Malvern Instruments Ltd, Worcestershire, UK) with 50 µg/mL MSN dispersed in DI water.

*Bacteria:* *F. tularensis* subsp. *holarctica* Live Vaccine Strain (LVS) was obtained from Centers for Disease Control and Prevention (Atlanta, GA). LVS glycerol stocks were prepared as described and stored at -80 °C.<sup>33</sup> For *in vitro* macrophage experiments, a vial of the LVS frozen glycerol stock was thawed in a 37 °C water bath and cultivated on GCII chocolate agar plates for 3 days before use. For *in vivo*

mouse experiments, a vial of pre-titered LVS frozen stock was used directly to infect mice and immediately afterward serially diluted and plated on GCII chocolate agar to confirm the bacterial numbers used to infect. For fluorescence studies, LVS expressing superfolder green fluorescent protein (LVS-GFP) was grown on GCII chocolate agar containing kanamycin at a concentration of 10 µg/mL for 3 days prior to use for infecting macrophages.

*Macrophages:* Human peripheral blood monocytes were prepared from the blood of healthy donors and cultivated in Teflon wells for 5 days to differentiate them into monocyte derived macrophages.<sup>29</sup> Human THP-1 monocytic cells (American Type Culture Collection, TIB-202) were maintained in RPMI-1640 (Lonza) supplemented with 10% fetal bovine serum (Mediatech), 2 mM GlutaMAX (Life Technology), penicillin (100 IU) and streptomycin (100 µg/mL) at 37 °C, 5% CO<sub>2</sub> – 95% air atmosphere. Prior to usage, THP-1 cells were differentiated into macrophages with 100 nM phorbol 12-myristate 13-acetate (PMA; Sigma) in antibiotic-free RPMI with 10% fetal bovine serum.

*Assessment of MSN Efficacy in Macrophages:* PMA-differentiated THP-1 cells were plated at  $1 \times 10^5$  cells per 200 µL per well in 96-well plates (Matrical) and infected with  $10^6$  *F. tularensis* LVS for 90 min. The infected THP-1 macrophages were washed and incubated with fresh medium alone or fresh medium containing MXF, control MSNs (no MXF loading) or MXF-loaded MSNs. *F. tularensis* LVS infection and growth in THP-1 macrophages was determined by harvesting the bacteria from the infected macrophages at 2 hours and 1 day post infection. For all treatment groups,

the infected macrophage cultures were incubated in the continued presence of the treatment for one day (the free drug or nanoparticles were neither washed away nor re-added). Thereafter, *F. tularensis* LVS was harvested from the infected macrophages to assess the effect of treatment. The bacteria were harvested by lysing the macrophage monolayers with 1% saponin in PBS for 5 min at room temperature, serially diluted, and plated on GCII chocolate agar. Bacterial colony forming units (CFU) on agar plates were enumerated after incubation at 37 °C for 3 days.

*Assessment of MSN Efficacy in Mice:* Animal procedures were conducted according to protocols approved by the UCLA Animal Research Committee and NIH Guidelines for the Care and Use of Laboratory Animals in Research. In two experiments (Experiment 1 and Experiment 2), female Balb/c mice (Taconic) of approximately 18 g were provided with standard diet ad libitum and acclimated for one week. Mice were infected by the intranasal route with ~8000 (Experiment 1) or ~4000 (Experiment 2) CFU of *F. tularensis* LVS. Two mice were euthanized 5 hours after intranasal infection (day 0) to determine the number of bacteria delivered to the lung at the start of the experiment. An additional 3 mice were euthanized one day later (day 1) to determine bacterial growth during that period of time. Mice were then sham-treated or treated with MXF or MSN-MBI-MXF by tail vein injection every other day (day 1, day 3, and day 5) for a total of 3 treatments. Mice were euthanized one day after the last treatment (day 6). Lungs, livers, and spleens from infected mice that were sham-treated or treated with MXF or MSN-MBI-MXF were homogenized and serially diluted for plating on GCII chocolate agar containing sulfamethoxazole

(40 µg/mL), trimethoprim (8 µg/mL), and erythromycin (50 µg/mL). Bacterial CFU on the agar plates were enumerated after incubation at 37 °C for 4 days.

*Median-Effect Plots:* We used median-effect plots<sup>35</sup> to compare the relative efficacy of MSN-MBI-MXF and free MXF. The fraction of inhibition for samples treated with different amounts of MXF was calculated using bacterial CFU in base-10 logarithm (log CFU) with the equation: Fraction of inhibition = 1 - (log CFU from sample treated with MSN-MBI-MXF or MXF / log CFU from untreated sample). A median-effect plot for MSN-MBI-MXF or MXF was generated using MXF or MXF equivalent (MSNs) dose in base-10 logarithm as the X-axis and the fraction of surviving bacteria divided by the fraction of killed bacteria in base-10 logarithm as the Y-axis.

*Statistics:* Statistical analyses were performed using the Student's t-test. A *P* value of 0.05 or less was considered statistically significant.



### 3.6. Figures and Tables

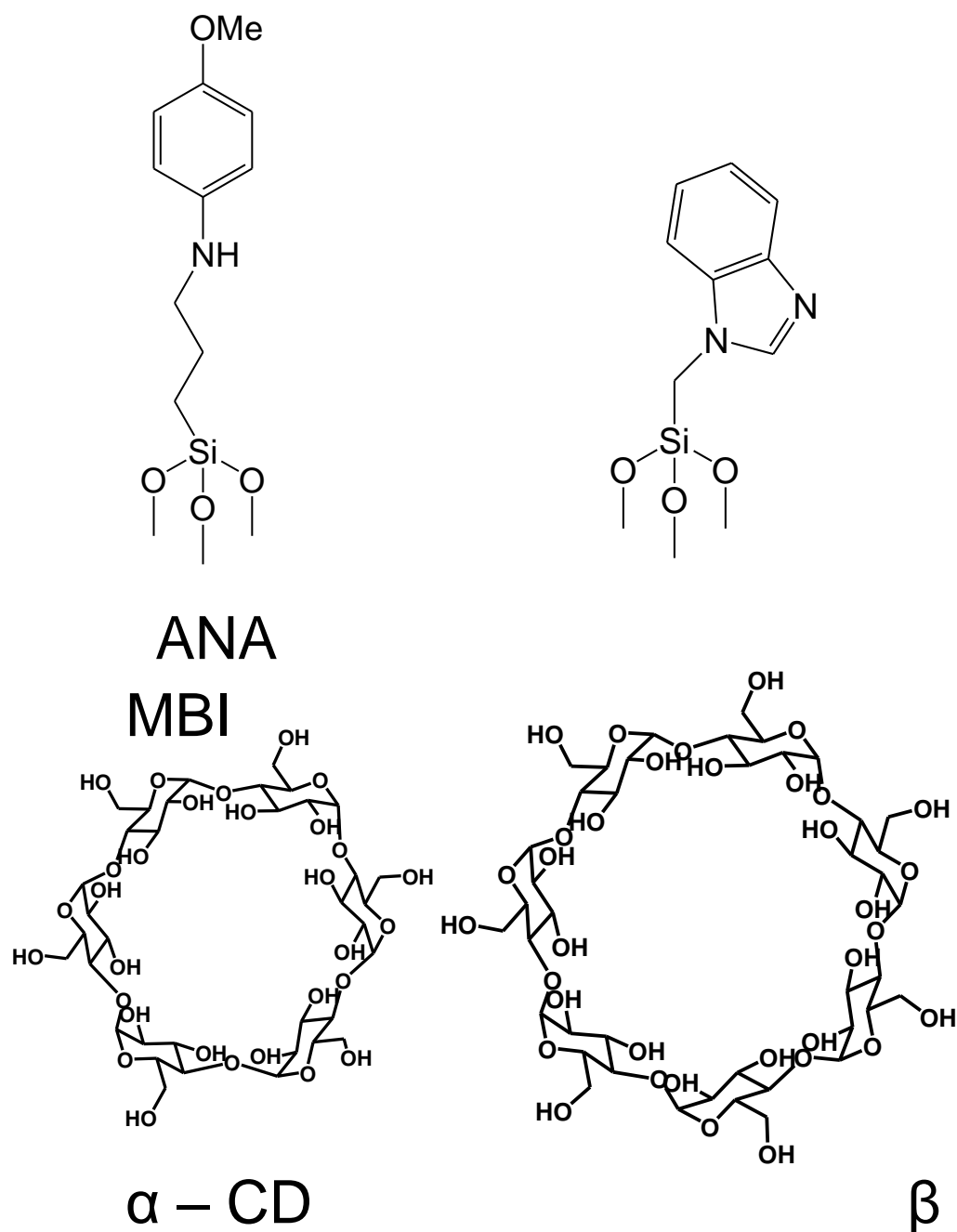


**Figure 3.1.** Chemical structures of the stalks (top) and caps (bottom) of two nanovalves. Left: the ANA (stalk) and  $\alpha$ -CD (cap); Right: the MBI (stalk) and  $\beta$ -CD (cap)

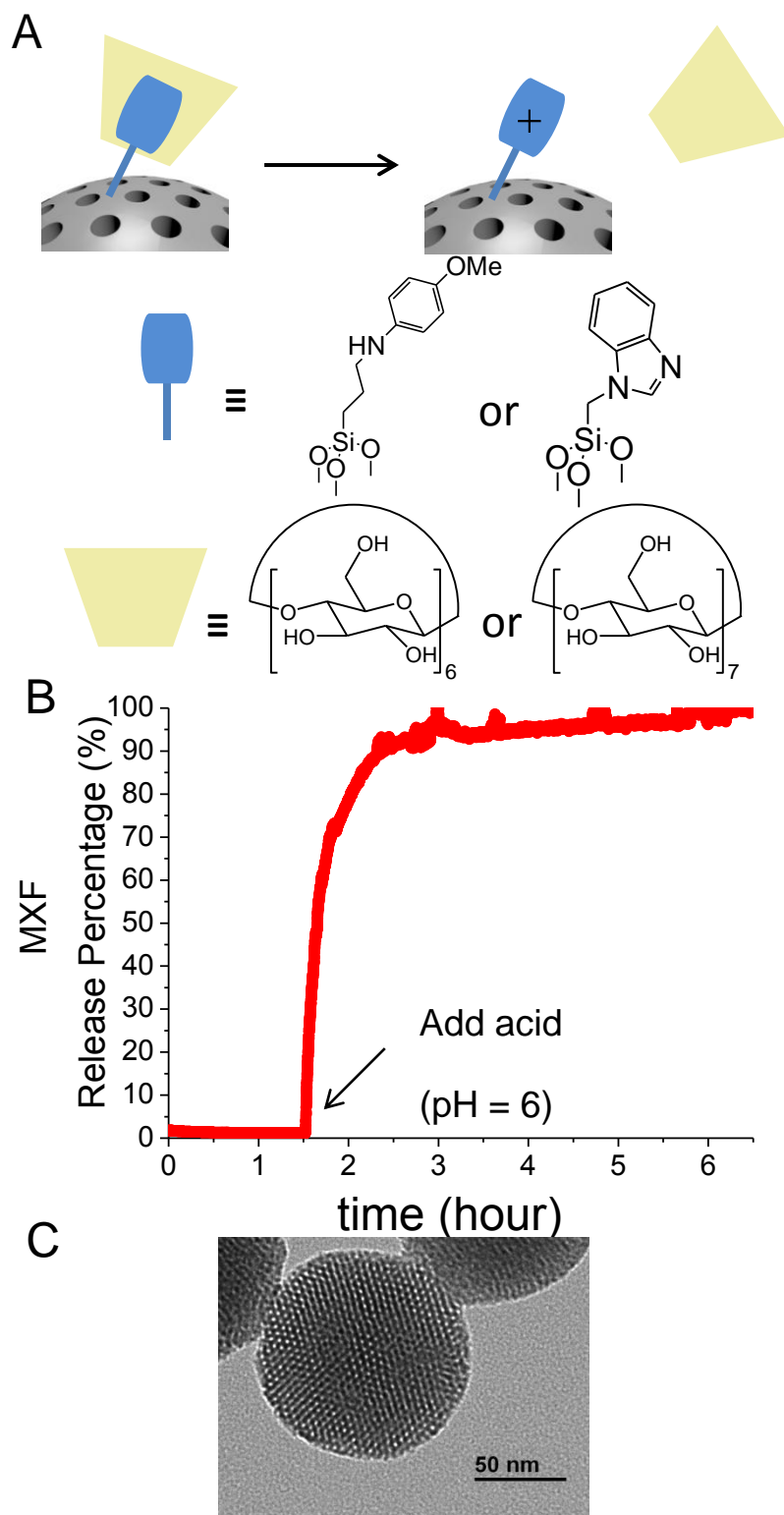


**Figure 3.2.** (A). Attachment of two different pH-sensitive nanovalves on MCM-41 surface. When the stalk is protonated, the cap molecule  $\alpha$ -CD or  $\beta$ -CD dissociates from it due to the decrease of the binding constant between them. (B)

MSN-MBI-MXF drug release profile. There is no leakage at pH 7, as indicated by the flat baseline; drug release starts when the pH is lowered to 6 by addition of acid. (C)

TEM image of MCM-41 showing its hexagonal pore structure.

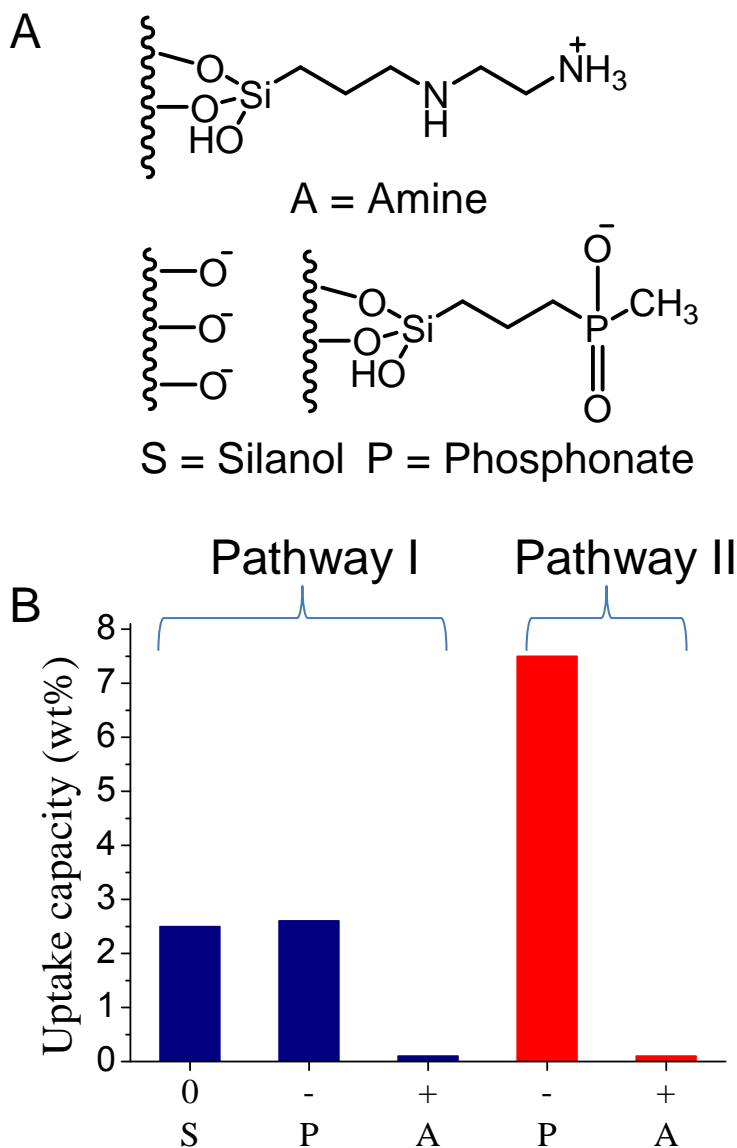


**Figure 3.3.** (A) Uptake capacity of MSN-MBI with different inner mesopore charges and stalk synthetic pathways. From left to right, samples are: slightly negatively charged underivatized MSN with stalk MBI synthesized by pathway I; negatively charged MSN-MBI by pathway I; positively charged MSN-MBI by pathway I; negatively charged MSN-MBI by pathway II; and positively charged MSN-MBI by pathway II. Pathway I: synthesize the whole stalk first and then attach it on MCM-41; pathway II: attach first part of stalk on MCM-41 first and then synthesize

the whole stalk. Negatively charged MCM-41 with nanovalve-MBI, synthesized by pathway II has highest uptake capacity, and positively charged MCM-41 uptakes almost nothing. (B) MSN mesopores modified (left to right) with amine (+), unmodified silanol (-), or phosphonate (-).

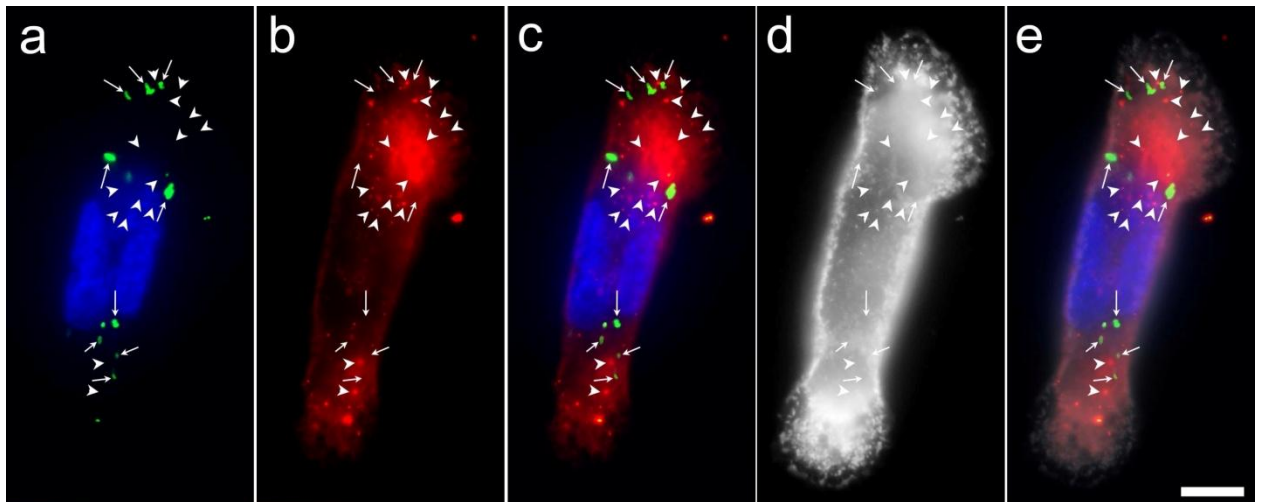


**Figure 3.4.** Confocal microscopy image of a *F. tularensis*-infected THP-1 macrophage that has taken up RITC-labeled MSN-MBI. Human macrophage-like THP-1 cells were infected with GFP-expressing *F. tularensis* for 90 min, washed, and incubated with 12.5  $\mu\text{g}/\text{mL}$  of RITC-labeled 100 nm MSN-MBI. After 3 hours, the cells were washed; the plasma membrane was stained with WGA-AlexaFluor 633; the cells were fixed; and nuclei were stained with DAPI. (a) LVS-GFP (green, arrows) and DAPI-stained nucleus (blue); (b) RITC-labeled MSN-MBI (red, arrowheads); (c) merged red, green, and blue color image; (d) contours of the cell are stained with WGA-AlexaFluor 633 (gray scale); (e) gray scale image superimposed onto merged color image, with the WGA-AlexaFluor 633 gray scale channel made partially transparent to allow the other channels to be seen. Scale bars, 10  $\mu\text{m}$ . The experiment was done twice with similar results.

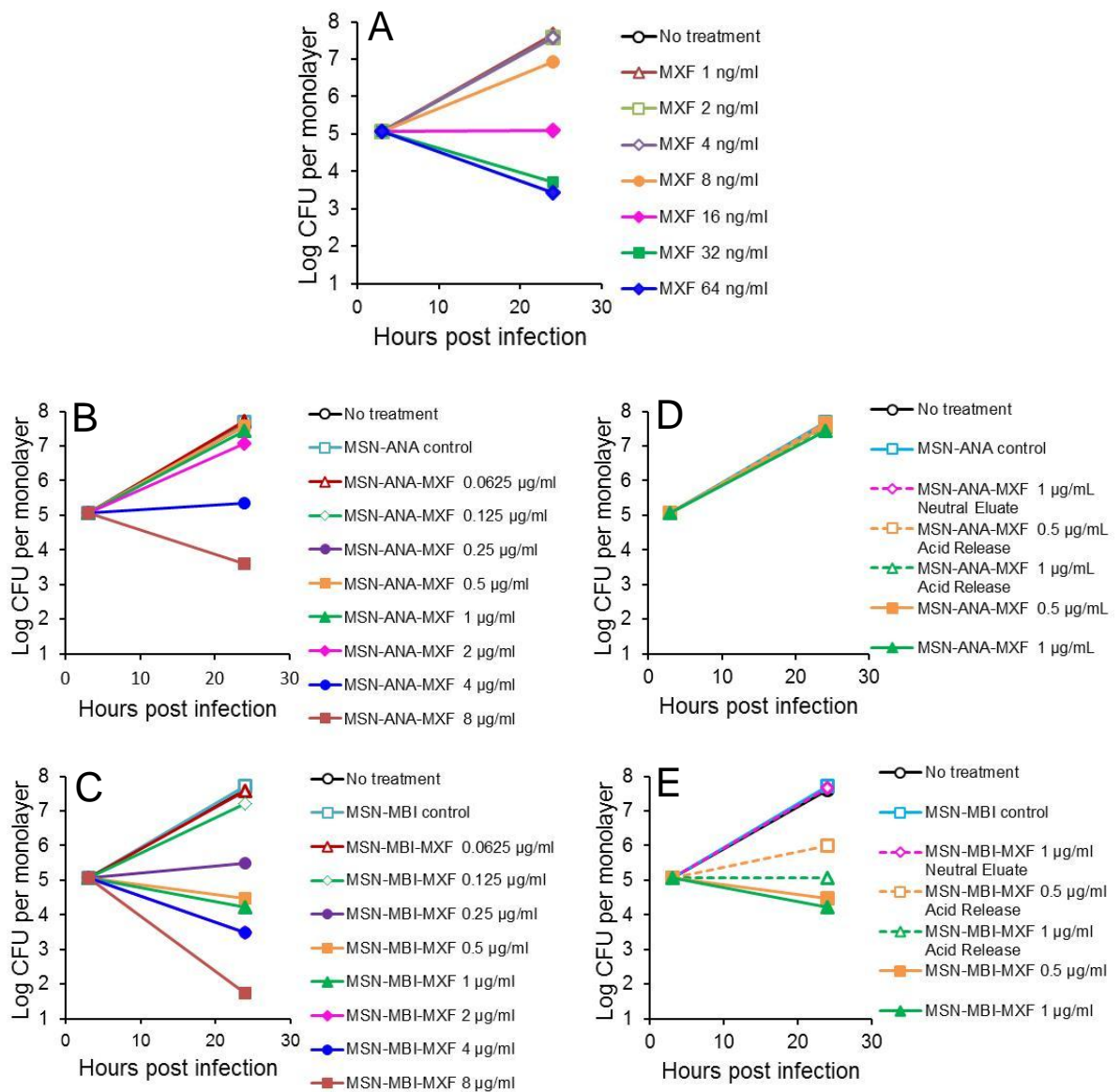


**Figure 3.5.** *In vitro* efficacy of MXF-loaded MSNs functionalized with two different types of pH-sensitive nanovalves. Human THP-1 macrophages were infected with *F. tularensis* LVS and treated with (A) MXF, (B) MSN-ANA-MXF or (C) MSN-MBI-MXF. Viable bacteria were determined by enumerating colony forming units (CFU) of *F. tularensis* in the macrophage monolayer. Impact of the drug released from (D) MSN-ANA-MXF and (E) MSN-MBI-MXF by maleate pH 1.8 was

assessed in the infected macrophage bioassay. Data shown are means of triplicate platings per macrophage monolayer, n = 1.

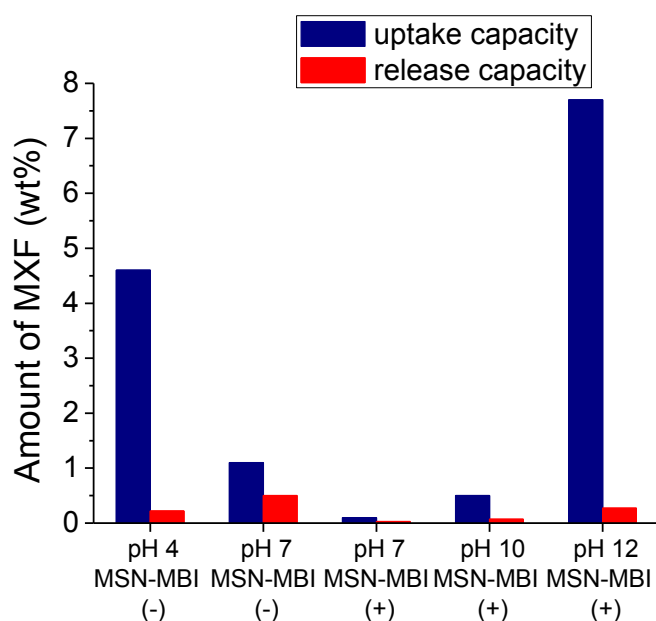


**Figure 3.6.** Uptake and release capacity of negatively charged MSN-MBI loaded at pH 4 or 7 and positively charged MSN-MBI loaded at pH 7, 10, or 12 MXF aqueous solution. MXF has positive net charge in solution at  $\text{pH} \leq 7$  and MCM-41 is negatively charged. Decreasing the loading pH from 7 to 4 increases uptake capacity, but, not release capacity because the nanovalve is open at pH 6 and particles must be transferred to neutral solution before capping. Most of MXF diffuses out of the pores because of these extra steps. At pH 7, positively charged MCM-41 repels MXF and leads to very low uptake and release capacities. MXF has negative charge when solution  $\text{pH} > 7$ , and increasing pH dramatically improves uptake capacities. However, loading at pH 12 does not lead to highest release capacity because particles degrade in base solution within 24 hours.



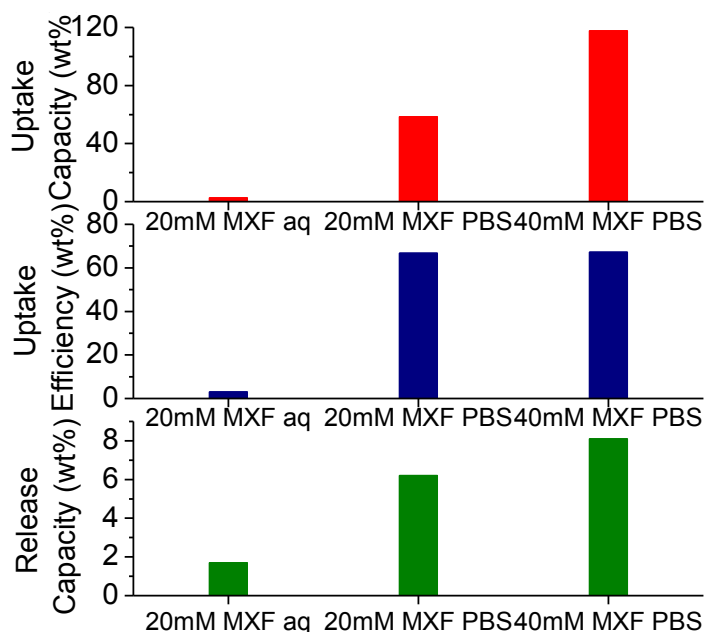


**Figure 3.7.** Uptake capacity, uptake efficiency and release capacity of phosphonated MSN-MBI loaded in 20 mM MXF aqueous solution (pH 7), 20 mM MXF PBS solution (pH 7.4) and 40 mM MXF PBS solution (pH 7.4). At same concentration 20 mM MXF, PBS loading increases the uptake more than 10 times than neutral water and release capacity got increased to 6.2 wt%, which is more than 3 times of 1.7 wt% from neutral loading. Increasing the loading concentration to 40 mM further improves uptake capacity to almost 120 wt% and release capacity 8.1 wt%. In terms of uptake efficiency, MSN-MBI uptakes around 70 % MXF from original solution for both 20 mM and 40 mM MXF loading.

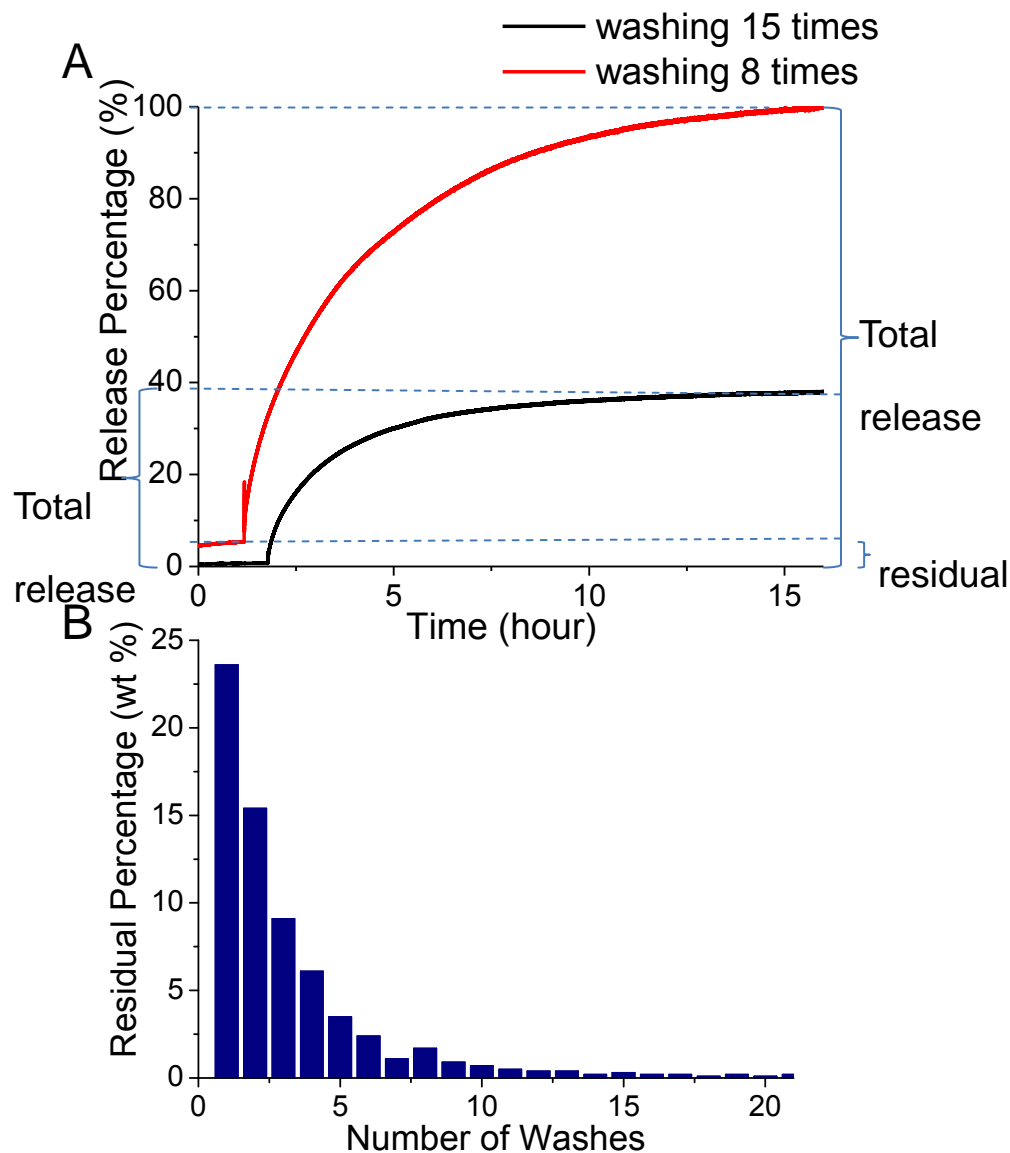


**Figure 3.8.** (A) Release profiles show that the more times the MSN are washed, the lower the amount of residual and release capacity. When particles were washed 15 times, there was negligible residual drug detected from the particle surface (no fluorescence detected). A small amount of residual was observed when drug loaded particles were washed 8 times. The experiments were repeated three times and all of them show the same relation between washing and release capacity. (B) The amount of MXF washed away each time decreases as the number of washes increases; the

decrease for each step is ~30 %. The first eight washes contribute ~95 % to the total amount of MXF ultimately removed by washing.

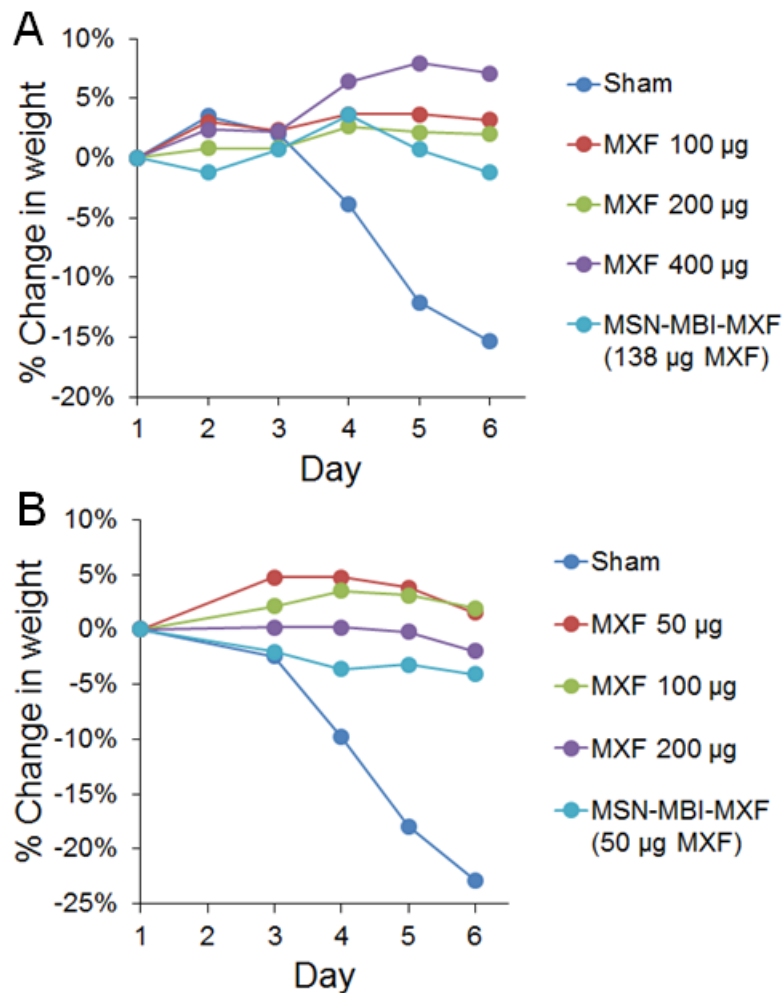


**Figure 3.9.** Treatment with MSN-MBI-MXF prevents weight loss caused by pneumonic tularemia. A and B show two independent mouse experiments (Experiment 1 and Experiment 2, respectively) in which the percentage change in weight of *F. tularensis*-infected mice was monitored over the course of the experiments. The mice were sham treated, treated with one of three doses of MXF as a free drug, as indicated, or treated with MSN-MBI-MXF (loaded with 138 µg MXF in Experiment 1 and 50 µg MXF in Experiment 2). Data shown are means of 3

– 4 mice per group. The experiment was done twice and both experiments are shown above.

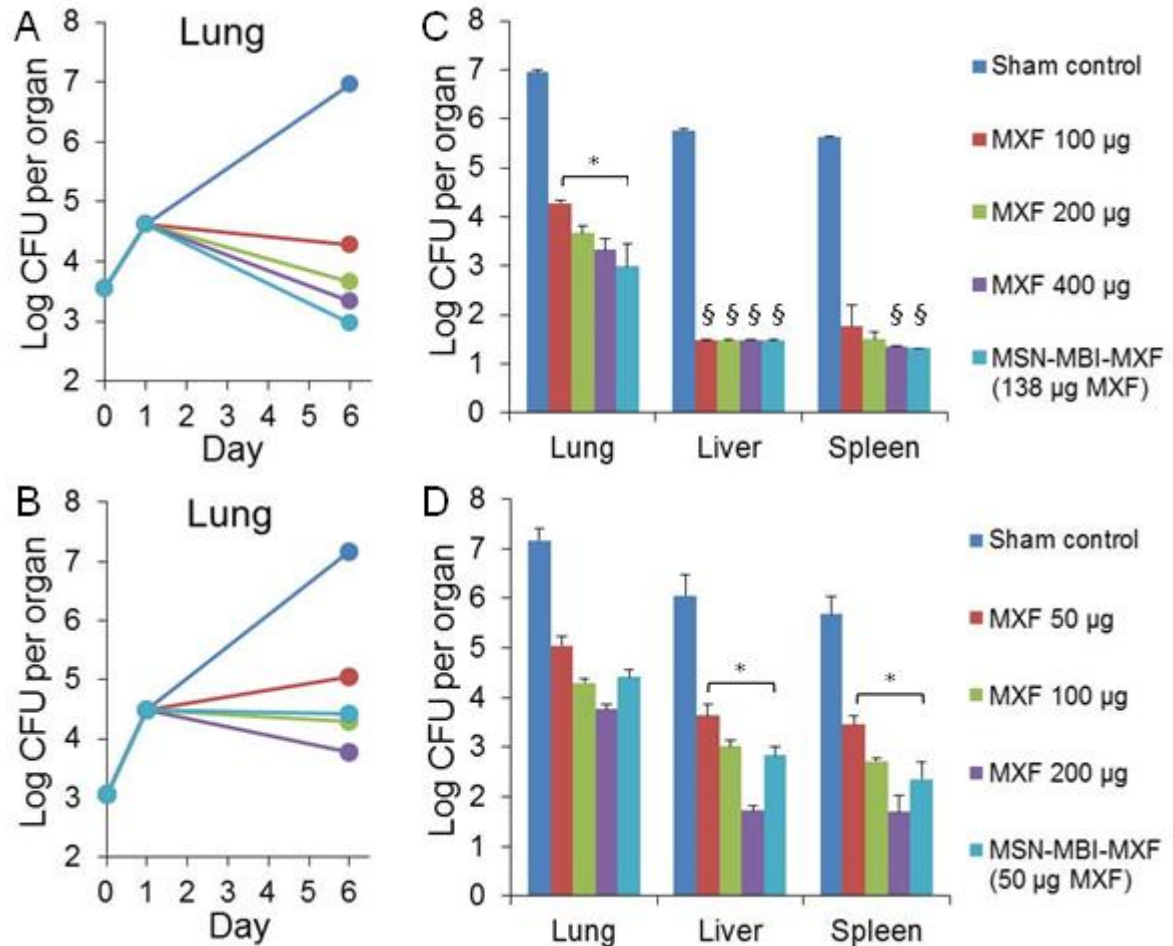


**Figure 3.10.** *In vivo* efficacy of MSN-MBI-MXF assessed by assay of *F. tularensis* burden in the mouse organs in two independent experiments, Experiment 1 (A and C) and Experiment 2 (B and D). Mice were infected with *F. tularensis* LVS by the intranasal route. (A and B) Bacterial burden in the lung was monitored over the course of infection. One day post-infection, mice were sham treated, treated with one of three doses of free MXF, as indicated, or treated with MSN-MBI-MXF (loaded with 138 µg in Experiment 1 shown in A and 50 µg in Experiment 2 shown in B) by tail vein injection on days 1, 3, and 5. (C and D) Mice were euthanized one day after

the last dose of treatment (day 6) to enumerate bacterial numbers in the lung, liver, and spleen. § Bacterial CFU below limit of detection. \*P < 0.05 by one-tailed t-test. Data shown are means ± S.E. for 3 – 4 mice per group. The experiment was done twice and both experiments are shown above.

**Table 3.1.** MXF molecular species distribution under different pH

MXF	Species in solution (calculated ratio %)					
	Positively charged			Negatively Charged		
	pH 4	pH 7	pH 7.4	pH 8	pH 10	pH 12
$^+H_2N...COOH$	99.50	16.60	7.30	1.90	0.01	0.01
$^+H_2N...COO^-$	0.49	83.30	87.80	93.50	16.60	0.20
$HN...COO^-$	0.01	0.10	4.80	4.60	83.30	99.79

% fully protonated form ( $^+H_2N...COOH$ ) =  $100 / (1 + 10^{pH-pKa1} + 10^{2*pH-pKa1-pKa2})$ , % zwitterions ( $^+H_2N...COO^-$ ) =  $100 / (1 + 10^{pKa1-pH} + 10^{pH-pKa2})$ , % fully deprotonated form ( $HN...COO^-$ ) =  $100 - \% (^+H_2N...COOH) - \% (^+H_2N...COO^-)$ <sup>36</sup>

**Table 3.2.** Uptake and release capacity of phosphonated MSN with pH sensitive nanovalves

Sample	Uptake capacity (wt %)	Release capacity (wt %)
MSN-ANA-MXF ( $\alpha$ -CD cap)	2.8 %	0.16 %
MSN-MBI-MXF ( $\beta$ -CD cap)	7.4 %	1.02 %

**Table 3.3.** Uptake capacity of MXF loaded MSN with different nanovalves (at low concentration)

Sample	Uptake capacity (wt %)
MSN-ANA-MXF	20 %
MSN-MBI-MXF	51.4 %

### 3.7. References

1. Ellis, J.; Oyston, P. C.; Green, M.; Titball, R. W. Tularemia. *Clin. Microbiol. Rev.* 2002, *15*, 631-646.
2. Christopher, G. W.; Cieslak, T. J.; Pavlin, J. A.; Eitzen, E. M. Biological Warfare - A Historical Perspective. *Jama-J Am Med Assoc* 1997, *278*, 412-417.
3. Harris, S. Japanese Biological Warfare Research on Humans - A Case-Study of Microbiology and Ethics. *Ann Ny Acad Sci* 1992, *666*, 21-52.
4. Alibek, K.; Handelman, S. *Biohazard : the Chilling True Story of the Largest Covert Biological Weapons Program in the World, Told from the inside by the Man Who Ran It*. Random House: New York, 1999; pp 319.
5. Feldman, K. A.; Ensore, R. E.; Lathrop, S. L.; Matyas, B. T.; McGuill, M.; Schriefer, M. E.; Stiles-Enos, D.; Dennis, D. T.; Petersen, L. R.; Hayes, E. B. An Outbreak of Primary Pneumonic Tularemia on Martha's Vineyard. *New Engl J Med* 2001, *345*, 1601-1606.
6. Chocarro, A.; Gonzalez, A.; Carcia, I. Treatment of Tularemia with Ciprofloxacin. *Clin Infect Dis* 2000, *31*, 623-623.
7. Chen, H. W.; Wang, L. Y.; Yeh, J.; Wu, X. Y.; Cao, Z. H.; Wang, Y. A.; Zhang, M. M.; Yang, L.; Mao, H. Reducing Non-Specific Binding and Uptake of Nanoparticles and Improving Cell Targeting with An Antifouling PEO-b-P Gamma MPS Copolymer Coating. *Biomaterials* 2010, *31*, 5397-5407.
8. Lee, J. E.; Lee, N.; Kim, H.; Kim, J.; Choi, S. H.; Kim, J. H.; Kim, T.; Song, I. C.; Park, S. P.; Moon, W. K.; *et al.* Uniform Mesoporous Dye-Doped Silica

Nanoparticles Decorated with Multiple Magnetite Nanocrystals for Simultaneous Enhanced Magnetic Resonance Imaging, Fluorescence Imaging, and Drug Delivery. *J Am Chem Soc* 2010, *132*, 552-557.

9. He, Q. J.; Zhang, Z. W.; Gao, F.; Li, Y. P.; Shi, J. L. *In vivo* Biodistribution and Urinary Excretion of Mesoporous Silica Nanoparticles: Effects of Particle Size and PEGylation. *Small* 2011, *7*, 271-280.

10. Barbe, C.; Bartlett, J.; Kong, L. G.; Finnie, K.; Lin, H. Q.; Larkin, M.; Calleja, S.; Bush, A.; Calleja, G. Silica particles: A Novel Drug-Delivery System. *Adv Mater* 2004, *16*, 1959-1966.

11. Argyo, C.; Weiss, V.; Brauchle, C.; Bein, T. Multifunctional Mesoporous Silica Nanoparticles as A Universal Platform for Drug Delivery. *Chem Mater* 2014, *26*, 435-451.

12. Li, Z. X.; Barnes, J. C.; Bosoy, A.; Stoddart, J. F.; Zink, J. I. Mesoporous Silica Nanoparticles in Biomedical Applications. *Chem Soc Rev* 2012, *41*, 2590-2605.

13. Tarn, D.; Ashley, C. E.; Xue, M.; Carnes, E. C.; Zink, J. I.; Brinker, C. J. Mesoporous Silica Nanoparticle Nanocarriers: Biofunctionality and Biocompatibility. *Accounts Chem Res* 2013, *46*, 792-801.

14. Xue, M.; Zhong, X.; Shaposhnik, Z.; Qu, Y. Q.; Tamanoi, F.; Duan, X. F.; Zink, J. I. pH-Operated Mechanized Porous Silicon Nanoparticles. *J Am Chem Soc* 2011, *133*, 8798-8801.

15. Meng, H. A.; Xue, M.; Xia, T. A.; Zhao, Y. L.; Tamanoi, F.; Stoddart, J. F.; Zink, J. I.; Nel, A. E. Autonomous *In vitro* Anticancer Drug Release from Mesoporous

- Silica Nanoparticles by pH-Sensitive Nanovalves. *J Am Chem Soc* 2010, *132*, 12690-12697.
16. Hwang, A. A.; Lu, J.; Tamanoi, F.; Zink, J. I. Functional Nanovalves on Protein-Coated Nanoparticles for *In vitro* and *In vivo* Controlled Drug Delivery. *Small* 2015, *11*, 319-328.
17. Dong, J. Y.; Xue, M.; Zink, J. I. Functioning of Nanovalves on Polymer Coated Mesoporous Silica Nanoparticles. *Nanoscale* 2013, *5*, 10300-10306.
18. Ferris, D. P.; Zhao, Y. L.; Khashab, N. M.; Khatib, H. A.; Stoddart, J. F.; Zink, J. I. Light-Operated Mechanized Nanoparticles. *J. Am. Chem. Soc.* 2009, *131*, 1686-1688.
19. Thomas, C. R.; Ferris, D. P.; Lee, J. H.; Choi, E.; Cho, M. H.; Kim, E. S.; Stoddart, J. F.; Shin, J. S.; Cheon, J.; Zink, J. I. Noninvasive Remote-Controlled Release of Drug Molecules *In vitro* Using Magnetic Actuation of Mechanized Nanoparticles. *J Am Chem Soc* 2010, *132*, 10623-10625.
20. Clemens, D. L.; Lee, B. Y.; Xue, M.; Thomas, C. R.; Meng, H.; Ferris, D.; Nel, A. E.; Zink, J. I.; Horwitz, M. A. Targeted Intracellular Delivery of Antituberculosis Drugs to Mycobacterium Tuberculosis-Infected Macrophages *via* Functionalized Mesoporous Silica Nanoparticles. *Antimicrob Agents Ch* 2012, *56*, 2535-2545.
21. Liong, M.; Lu, J.; Kovichich, M.; Xia, T.; Ruehm, S. G.; Nel, A. E.; Tamanoi, F.; Zink, J. I. Multifunctional Inorganic Nanoparticles for Imaging, Targeting, and Drug Delivery. *ACS Nano* 2008, *2*, 889-896.



22. Luo, G. F.; Chen, W. H.; Liu, Y.; Lei, Q.; Zhuo, R. X.; Zhang, X. Z. Multifunctional Enveloped Mesoporous Silica Nanoparticles for Subcellular Co-Delivery of Drug and Therapeutic Peptide. *Scientific reports* 2014, 4, 6064.
23. Lu, J.; Liong, M.; Li, Z. X.; Zink, J. I.; Tamanoi, F. Biocompatibility, Biodistribution, and Drug-Delivery Efficiency of Mesoporous Silica Nanoparticles for Cancer Therapy in Animals. *Small* 2010, 6, 1794-1805.
24. Steward, J.; Piercy, I.; Lever, M. S.; Simpson, A. J. H.; Brooks, T. J. G. Treatment of Murine Pneumonic *Francisella tularensis* Infection with Gatifloxacin, Moxifloxacin or Ciprofloxacin. *Int J Antimicrob Ag* 2006, 27, 439-443.
25. Du, L.; Liao, S. J.; Khatib, H. A.; Stoddart, J. F.; Zink, J. I. Controlled-Access Hollow Mechanized Silica Nanocontainers. *J Am Chem Soc* 2009, 131, 15136-15142.
26. Clemens, D. L.; Lee, B. Y.; Horwitz, M. A. Virulent and Avirulent Strains of *Francisella tularensis* Prevent Acidification and Maturation of Their Phagosomes and Escape into the Cytoplasm in Human Macrophages. *Infect. Immun.* 2004, 72, 3204-3217.
27. Meng, H.; Liong, M.; Xia, T.; Li, Z.; Ji, Z.; Zink, J. I.; Nel, A. E. Engineered Design of Mesoporous Silica Nanoparticles to Deliver Doxorubicin and P-glycoprotein siRNA to Overcome Drug Resistance in A Cancer Cell Line. *ACS Nano* 2010, 4, 4539-4550.
28. Storm, G.; Belliot, S. O.; Daemen, T.; Lasic, D. D. Surface Modification of Nanoparticles to Oppose Uptake by the Mononuclear Phagocyte System. *Adv. Drug Del. Rev.* 1995, 17, 31-48.

29. Clemens, D. L.; Lee, B. Y.; Horwitz, M. A. O-Antigen-Deficient *Francisella tularensis* Live Vaccine Strain Mutants are Ingested via An Aberrant Form of Looping Phagocytosis and Show Altered Kinetics of Intracellular Trafficking in Human Macrophages. *Infect Immun* 2012, 80, 952-967.
30. Ilinskaya, A. N.; Dobrovolskaia, M. A. Nanoparticles and the Blood Coagulation System. Part II: Safety Concerns. *Nanomedicine (Lond)* 2013, 8, 969-981.
31. Fornaguera, C.; Caldero, G.; Mitjans, M.; Vinardell, M. P.; Solans, C.; Vauthier, C. Interactions of PLGA Nanoparticles with Blood Components: Protein Adsorption, Coagulation, Activation of the Complement System and Hemolysis Studies. *Nanoscale* 2015, 7, 6045-6058.
32. Nel, A.; Xia, T.; Madler, L.; Li, N. Toxic Potential of Materials at the Nanolevel. *Science* 2006, 311, 622-627.
33. Jia, Q. M.; Lee, B. Y.; Bowen, R.; Dillon, B. J.; Som, S. M.; Horwitz, M. A. A *Francisella tularensis* Live Vaccine Strain (LVS) Mutant with A Deletion in capB, Encoding A Putative Capsular Biosynthesis Protein, is Significantly More Attenuated than LVS Yet Induces Potent Protective Immunity in Mice against *F. tularensis* Challenge. *Infect Immun* 2010, 78, 4341-4355.
34. Jia, Q. M.; Lee, B. Y.; Clemens, D. L.; Bowen, R. A.; Horwitz, M. A. Recombinant Attenuated *Listeria Monocytogenes* Vaccine Expressing *Francisella tularensis* IglC Induces Protection in Mice against Aerosolized Type A *F. tularensis*. *Vaccine* 2009, 27, 1216-1229.

35. Chou, T. C. Theoretical Basis, Experimental Design, and Computerized Simulation of Synergism and Antagonism in Drug Combination Studies. *Pharmacol Rev* 2006, 58, 621-681.
36. Lemaire, S.; Tulkens, P. M.; Van Bambeke, F. Contrasting Effects of Acidic pH on the Extracellular and Intracellular Activities of the Anti-Gram-Positive Fluoroquinolones Moxifloxacin and Delafloxacin against *Staphylococcus Aureus*. *Antimicrob Agents Ch* 2011, 55, 649-658.

## Chapter 4

Redox-triggered Release of Moxifloxacin from Mesoporous Silica Nanoparticles  
Functionalized with Disulfide Snap-Tops Enhances Efficacy Against Pneumonic  
Tularemia in Mice

#### 4.1. Abstract

Effective and rapid treatment of tularemia, especially the inhalational form, is needed to reduce morbidity and mortality of this serious and potentially fatal infectious disease. The etiologic agent of tularemia, *Francisella tularensis*, is a facultative intracellular bacterial pathogen which infects and multiplies to high numbers in macrophages. Nanotherapeutics are particularly promising for treatment of infectious diseases caused by intracellular pathogens whose primary host cells are macrophages because nanoparticles preferentially target and are avidly internalized by macrophages. We have developed a mesoporous silica nanoparticle (MSN) functionalized with disulfide snap-tops that has high drug loading and selectively releases drug intracellularly in response to the intracellular redox potential. These nanoparticles, when loaded with Hoechst fluorescent dye, release their cargo exclusively intracellularly and stain the nuclei of macrophages. We demonstrate the utility of the nanoparticles by comparing the efficacy of the antibiotic moxifloxacin delivered by MSNs vs. administered as free drug in macrophages infected with *F. tularensis* and in a mouse model of pneumonic tularemia. The MSNs loaded with moxifloxacin killed *F. tularensis* in macrophages in a dose-dependent fashion and had the same potency as an equivalent amount of free drug. *In vivo*, MSNs loaded with moxifloxacin prevented weight loss, illness, and death in the *F. tularensis* challenged mice, markedly reduced the organ burden of *F. tularensis* in the lung, liver and spleen, and were significantly more efficacious than an equivalent amount of free drug. This study provides an important proof-of-principle for the potential therapeutic use of a

novel nanoparticle drug delivery platform.

## 4.2. Introduction

*Francisella tularensis* is a highly infectious bacterium that causes a life threatening disease, tularemia. Inhalation of as few as 25 bacteria is sufficient to cause severe illness.<sup>1</sup> Its extremely high infectivity, ease of dissemination by the air borne route, and capacity to cause severe disease motivated its development as a biological weapon by Japan during the second World War<sup>2</sup> and by both the U.S. and the former Soviet Union during the cold war.<sup>3</sup> Although effective antibiotics for treatment of tularemia are available, intensive care is frequently required, relapse and complications are frequent, and the infection can be fatal even with appropriate treatment. Concern over its potential for use as a biological weapon has led to its federal classification as a Tier 1 Select Agent. It has been estimated that deliberate dispersal of *F. tularensis* over a large city would overwhelm health care facilities and result in thousands of deaths.<sup>4</sup> Development of more effective treatment for tularemia has the potential to reduce the number of patients requiring intensive care and to reduce the duration that such care is required. Because *F. tularensis* causes disease primarily by replicating intracellularly within host macrophages,<sup>5</sup> a delivery strategy that targets macrophages and delivers high concentrations of antibiotic to the macrophages has the potential to provide more effective treatment.

After systemic administration, nanoparticles are avidly taken up by macrophages of the mononuclear phagocyte system in the lung, liver, and spleen.<sup>6-8</sup> Because these are the cells infected by *F. tularensis*, a nanoparticle delivery system

has the potential to deliver high concentrations of antibiotic to the site of infection while minimizing systemic exposure. Nanoparticles also have several other advantages over free drug, including shielding the drug from metabolism and excretion and providing more favorable pharmacokinetics. While several different nanoparticle delivery platforms have been studied for antibiotic delivery, including liposomes, solid lipid particles, poly-L-lactide (PLGA), and biological materials such as gelatin, chitosan, and alginates,<sup>9, 10</sup> mesoporous silica nanoparticles (MSNs) offer several important advantages, including structural and chemical stability, uniformity, inherent lack of toxicity, capacity to encapsulate exceptionally high concentrations of different types of cargo, and versatility in incorporating rational design features, including stimulus responsive drug release systems.<sup>11-17</sup> In this work, we have developed a stimulus-responsive MSN platform for treatment of tularemia that delivers the antibiotic moxifloxacin (MXF) intracellularly in response to the intracellular redox potential.

Living cells have more reducing power than extracellular medium or plasma because of numerous redox couples that are kept primarily in the reduced state by metabolic processes such as glycolysis, mitochondrial electron transport, and the pentose phosphate pathway. These redox couples include NADH/NAD; NADPH/NADP; thioredoxin/oxidized-thioredoxin, cysteine/cystine, and glutathione (GSH)/GSSG, with the latter redox couple being quantitatively the most abundant inside cells, with cytosolic GSH concentrations in the 1 -10 mM range.<sup>18</sup> Extracellularly, in culture medium and in plasma, the cysteine/cystine redox couple is

quantitatively the most important. Disulfide snap-top MSNs release cargo selectively intracellularly because the redox potential is much lower in the intracellular than in the extracellular environment.<sup>19, 20</sup> On the basis of the intracellular glutathione/glutathione disulfide ratio, the redox potential is estimated to range from -250 mV in rapidly dividing cells to -200 mV in differentiating cells to -160 mV in cells undergoing apoptosis.<sup>21</sup> Different compartments within the cell also maintain different ambient potentials; for example, based on the thioredoxin redox poise, the cytoplasm, nucleus, and mitochondria exhibit redox potentials of -280, -300, and -340 mV, respectively.<sup>20</sup> On the other hand, the GSH/GSSG redox couple in plasma has a redox potential of -140 mV<sup>22</sup> and the much more abundant cysteine-cystine is even more oxidized, with a redox potential of -80 mV.<sup>23</sup> A similar situation is replicated in cell culture model systems, as human cell lines regulate the redox state of the cysteine-cystine couple in their culture medium to approximately -80 mV.<sup>24</sup> Prior to addition to cultured cells, cysteine-free RPMI-1640 has a relatively high redox potential of -37 mV and RPMI supplemented with 0.45 mM cysteine has a redox potential of -182 mV.

While the concept of redox responsive disulfide snap-top functionalized MSNs has been reported previously,<sup>19,25</sup> their functionality in cells or in animals as a means of effective antibiotic drug delivery to kill intracellular bacteria has not previously been described. Although streptomycin and aminoglycosides are historically considered the treatment of choice for tularemia, they cross membranes poorly, have relatively high minimum inhibitory levels against *F. tularensis*, have side



effects of ototoxicity and nephrotoxicity, and are difficult to administer. Doxycycline or ciprofloxacin are recommended for post-exposure treatment in a mass casualty setting.<sup>3</sup> In contrast to aminoglycosides, fluoroquinolones cross membranes readily and have much lower minimal inhibitory concentrations against *F. tularensis*. Ciprofloxacin has been used successfully both in animal models of tularemia<sup>26</sup> and in the treatment of clinical tularemia infections.<sup>27</sup> In a mouse model of pneumonic tularemia comparing ciprofloxacin, gatifloxacin, and MXF, while all three fluorquinolones showed efficacy during the treatment phase, both MXF and gatifloxacin were superior to ciprofloxacin in preventing relapse, indicating greater efficacy in eradicating the *F. tularensis*.<sup>28</sup> Because of its potent antimicrobial activity against *F. tularensis* as well as potent activity against many other important intracellular human pathogens, including *Mycobacterium tuberculosis*,<sup>29</sup> *Listeria monocytogenes*,<sup>30</sup> *Mycoplasma*, *Chlamydia*, *Shigella*, and *Salmonella*, we developed our redox-responsive disulfide snap-top MSNs (MSN-SS-MXF) for delivery of MXF.

In this study, we demonstrate that our MSN-SS-MXF delivery platform releases its antibiotic cargo intracellularly in macrophages, is effective in killing *F. tularensis* in infected macrophages in a cell culture model, and is a much more effective treatment than an equivalent amount of free drug in a mouse model of pneumonic tularemia.

### **4.3. Results and Discussion**

#### **4.3.1. Synthesis of Disulfide Snap-top MSNs**

To utilize MSNs to deliver MXF into macrophages and release the drug

intracellularly in a controlled fashion, we developed a disulfide snap-top attached to the surface of the MSN so as to trap drug inside mesopores. The synthesis procedure is illustrated in Figure 4.1. A silane stalk (3-mercaptopropyl) trimethoxysilane was attached on the surface of MSN first and then 1-adamantanethiol reacted with the silane linker in the presence of the oxidant thiocyanogen to form a disulfide bond (Figure 4.2). Disulfide modified MSN was then mixed with MXF PBS solution for 24 hours, followed by adding  $\beta$ -cyclodextrin ( $\beta$ -CD) as the capping molecule which formed a stable complex with the adamantyl group. In reducing environments (e.g. after addition of glutathione or after uptake by macrophages), the disulfide bond is cleaved and cargo is released. The strong binding affinity between the adamantyl group and  $\beta$ -CD ensure that cargo is trapped inside the pores and prevents premature leakage before reaching target cells.

MXF is a fourth generation fluoroquinolone active against both Gram-positive and Gram-negative bacteria. It has a UV-Vis maximum absorption peak at 288 nm in PBS allowing spectroscopic measurement of its concentration. We measured the absorbance of MXF in solution before and after loading the nanoparticles (Figure 4.3) and used the difference in concentration to calculate the amount of MXF taken up by the particles (including inside pore channels and on external surfaces). The mass of MXF taken up by particles divided by the mass of MSNs is defined as “uptake capacity” (expressed in wt%). After washing mechanized MSN with PBS sufficiently to remove MXF from the outer surface, the nanoparticles were dispersed in deionized water or PBS and then an excess amount of 2-mercaptoethanol was added to cleave

the disulfide bond and release the drug. The mass of released MXF divided by the mass of the particle is defined as “release capacity” (expressed in wt%)

#### **4.3.2. Optimization of Uptake and Release Capacity**

Release capacity of a nanoparticle delivery system is an important factor that impacts in vivo efficacy, as a higher release capacity allows a greater amount of drug to be delivered to target cells with the same number of MSNs. We exploited charge interactions between the cargo molecules and the MSN inner pores to achieve a high uptake and release capacity. MXF has two ionizable groups with pKa's of 6.3 and 9.3, and the extent to which the drug is positively charged, neutral, or negatively charged is pH-dependent. Hence, the pH of the loading solution markedly impacts uptake capacity. In PBS buffer with pH 7.4, 87.8% of MXF molecules are zwitterionic species, 7.3% molecules are positively charged, and 4.8% are negatively charged. We modified the inner pores of MSNs with either amine groups or phosphonate groups to make the inner environment positively or negatively charged, respectively. Positively charged cargo interacts electrostatically with negatively charged inner pores, thereby increasing the uptake capacity; however, strong electrostatic interaction between cargo molecules and pore channels may also slow the rate of cargo release.<sup>31</sup> On the other hand, positively charged inner pores electrostatically repulse the positively charged cargo molecules, thereby decreasing the uptake capacity but facilitating and increasing the rate of cargo release.

Before attaching snap-top caps, we measured the uptake capacity of MSNs with different inner pore charges and found that with positively charged mesopores the

uptake capacity was near zero, indicating that it is too difficult for MXF molecules with a positive net charge to diffuse into positively charged MSN channels. Use of negatively charged inner pores dramatically increased the uptake capacity to 30 wt% and the release capacity to 3 wt% (10 mM MXF in a volume of 1 mL PBS) (Table 4.2A). Other experiments showed that a further increase in negative charge on inner pores does not improve uptake and release capacity. Inner pore modification was achieved by co-condensation of two silanes, in which diethylphosphatoethyltriethoxysilane (DEPETS) was mixed with tetraethyl orthosilicate (TEOS) and then added to heated base solution in a dropwise fashion. Different amounts of DEPETS (10 $\mu$ L, 25 $\mu$ L and 35  $\mu$ L) were mixed with TEOS (60  $\mu$ L) to make more negatively charged inner pores, and these nanoparticles showed similar release capacity of ~2-3 wt% under the same loading conditions (Table 4.2B). This result suggested that the amount of phosphonate groups inside the pores is saturated and hence the attraction of positively charged MXF molecules is maximized.

We also tested loading MXF-SS in solutions of different pH because in acidic solutions, most of MXF molecules are positively charged and interact with negatively charged inner pores, resulting in a higher uptake capacity. However, lowering pH may also render phosphonate groups on inner pores partially protonated and thus less negatively charged, resulting in a lower uptake capacity. Experiments showed that loading with pH 3 MXF solution (1 mL 10 mM) resulted in 9.6 wt% uptake capacity, which is much lower than the 22.2 wt% uptake capacity obtained when loading with

pH 7.4 MXF solution (1 mL 10 mM). The enhanced uptake capacity at pH 7.4 is due to more negatively charged mesopores at this pH (Table 4.2C).

Moreover, we compared the uptake capacity of MSNs (10 mg) with 10  $\mu$ mol disulfide stalk surface coverage with that of MSNs with 20  $\mu$ mol surface coverage. We hypothesized that the higher surface coverage would cap more MXF molecules inside the pores. However, we obtained uptake capacities of 22.2 wt% and 19.7 wt% with surface coverage of 10  $\mu$ mol and 20  $\mu$ mol, respectively, which indicated that higher surface coverage with the silane stalks may increase the surface hydrophobicity of MSNs and lower the uptake of the hydrophilic drug MXF (Table 4.2D). Therefore, 10  $\mu$ mol disulfide stalk surface coverage provided a satisfactory balance between hydrophobicity and capping MXF within pores so as to achieve high uptake.

To obtain a higher uptake and release capacity, we loaded the same amount of MSN-SS with a more concentrated MXF PBS solution (40 mM MXF in a volume of 1mL PBS vs. 10 mM MXF in a volume of 1mL PBS). This yielded an uptake and release capacity of 135 wt% and 51 wt%, respectively, the highest release capacity yet obtained (Table 4.2E). This result indicates that the osmotic gradient of the loading system is an additional major factor impacting uptake and release capacity of MSN-SS-MXF. Considering a) the MSN's inner pores charges; b) the MSN's concentration of phosphonate groups; c) the MSN's disulfide stalk surface coverage; d) the loading concentration of MXF; and e) the loading pH, we found the optimal conditions to be negatively charged phosphonated MSNs (10  $\mu$ L DEPETS / 10 mg)

with disulfide stalk surface coverage of 10  $\mu\text{mol}$  loaded with 1mL 40 mM MXF in PBS solution (pH 7.4).

#### **4.3.3. Measurement of MSN-SS-MXF Release Capacity**

To obtain an accurate determination of MSN-SS-MXF release capacity, we used two different methods of measurement, UV-Vis spectroscopy and *F. novicida* bioassay, based on the physical property and biological activity of MXF, respectively. Measuring dye/drug UV-Vis absorption in aqueous solution is commonly used to determine release capacity. Because not all MXF molecules were released from mesopores in PBS, we dispersed MSN-SS-MXF in DMSO with 2-mercaptoethanol to completely release the MXF and determine the maximum release capacity. By UV-Vis measurement, MSN-SS-MXF released 9 wt% MXF in pure PBS, and after adding 2-mercaptoethanol, released a total of 21 wt% MXF. When MSN-SS-MXF is dispersed in DMSO,  $\beta$ -CD dissociates from the adamantyl group because of hydrophobic-hydrophobic interaction with DMSO. As shown in Table 4.1, by UV-Vis measurement, MSN-SS-MXF released 73 wt% MXF in pure DMSO, and the release capacity increased further to 133 wt% upon the addition of a reducing agent to cleave the disulfide bond. We suspected that this may reflect dissociation by DMSO of some byproducts from the MSN surface that overlap with MXF in their absorption spectrum, thus causing the DMSO eluates to overestimate the drug release capacity. To circumvent this complication, we developed a bioassay, based on inhibition of *F. novicida* growth in broth, to measure the amount of drug released from MSN-SS-MXF in PBS or DMSO with and without 2-mercaptoethanol. Using the *F.*

*novicida* bioassay, we measured a release capacity for MSN-SS-MXF of 12 wt% in PBS and a total of 18 wt% after addition of reductant, similar to the measurements obtained by UV spectroscopy under these aqueous conditions. However, when MSN-SS-MXF was dispersed in DMSO and DMSO with 2-mercaptoethanol, the bioassay measurement showed a release capacity of 48 wt% and 51 wt% respectively, lower than the 73 wt% and 133 wt% determined by UV-Vis spectroscopy. The high release capacity in DMSO alone and the minimal increase with the addition of 2-mercaptoethanol indicates that dissociation of  $\beta$ -CD from the adamantyl stalk has a release effect similar to disulfide bond cleavage. From these studies, we concluded that the release capacity of 51 wt%, measured by the bioassay, is the most accurate measurement of the maximum release capacity for MXF.

#### **4.3.4. Disulfide Snap-Top MSNs Release Cargo at Physiological GSH Concentrations**

Quantitatively, GSH is the major reducing agent in cells, with intracellular concentrations of approximately 10 mM in healthy cells.<sup>32, 33</sup> To determine whether the disulfide snap-tops operate at physiological concentrations of GSH, we loaded disulfide snap-top MSNs with Hoechst 33342, a membrane permeant probe for double-stranded DNA, and incubated them with 0 – 16 mM GSH in PBS for 18 hours at room temperature. The nanoparticles were pelleted by centrifugation and the supernates were diluted 20-fold with RPMI culture medium and added to monolayers of human macrophage-like THP-1 cells. The cells were incubated for 3 hours at 37 °C, stained with WGA-AF633 to label the plasma membranes, fixed, and the Hoechst

staining of the nuclei measured by fluorescence microscopy. We observed increasing Hoechst staining of the cell nuclei with increasing GSH concentrations in the physiological 1 – 10 mM range, confirming that the snap-top valves function at physiological intracellular concentrations of GSH (Figure 4.4).

#### **4.3.5. Release of Cargo in Response to Intracellular Environment**

To investigate whether the disulfide snap-top valves work properly inside of cells, we used the MSNs to deliver Hoechst 33342. We added Hoechst loaded disulfide snap-top MSNs and eluate prepared from the MSNs in PBS (non-reducing condition) to THP-1 macrophages and incubated at 37 °C for 18 hours. We observed that nuclei of THP-1 cells were stained after incubation with Hoechst 33342 loaded disulfide snap-top MSNs, but not after incubation with the PBS eluate of the MSNs (Figure 4.5). These results provide strong evidence that the disulfide snap-top valves open to release cargo in the intracellular reducing environment.

#### **4.3.6. Disulfide Snap-top MSNs are Taken Up by Human Macrophages and Kill intracellular *F. tularensis***

We assessed the efficacy of the disulfide snap-top MSNs loaded with MXF (MSN-SS-MXF) in a macrophage model of *F. tularensis* infection. We infected THP-1 macrophages with *F. tularensis* Live Vaccine Strain (LVS) and treated the infected macrophages with serial two-fold increasing concentrations of MSN-SS-MXF or free MXF. The infected macrophages that were not treated were lysed at 3 hours and 1 day post infection to monitor bacterial growth. All infected macrophages that were treated were lysed at 1 day post infection to determine the



impact of each treatment on bacterial viability in macrophages by enumerating colony forming units (CFU).

While with no treatment the bacteria grew 2.5 logs in one day, treatment with MSN-SS-MXF (6.25 – 400 ng/mL) or MXF (1 – 64 ng/mL) reduced bacterial CFU in macrophages in a dose-dependent manner (Figure 4.6A and C). The amount of releasable drug loaded on the disulfide snap-top MSNs was determined by the level of bacterial killing using supernatants prepared from the MSNs under a) aqueous PBS non-reducing condition; b) aqueous PBS with reducing agent 2-mercaptoethanol; and c) organic DMSO with reducing agent 2-mercaptoethanol. By comparing the amount of killing by supernatants prepared from MSN-SS-MXF with the amount of killing by free drug (Figure 4.6C), we determined the releasable drug loading under aqueous non-reducing, aqueous reducing, and organic reducing conditions to be 4.9 wt%, 9.9 wt% and 27.4 wt%, respectively. The higher percentage of drug release under organic reducing conditions indicates that MXF is strongly absorbed to MSN through hydrophobic interactions. Hence, in addition to a reducing condition, a hydrophobic environment, such as DMSO or an intracellular environment is required for efficient release of MXF from the disulfide snap-top MSN carrier.

Based on the drug release capacity of 27.4 wt%, the impact of MXF delivered by various doses of the MSN-SS-MXF in killing of *F. tularensis* LVS was compared with that of free drug using a median-effect plot.<sup>34</sup> As shown in Figure 4.6D, the median-effect plot of the MSN-SS-MXF is almost superimposable on that of the free drug, indicating that MXF delivered by the disulfide snap-top MSN has an efficacy

equal to that of free MXF in the *in vitro* macrophage model of *F. tularensis* LVS infection.

#### **4.3.7. MSN-SS-MXF is Much More Efficacious Than an Equivalent Amount of Free MXF in a Mouse Model of Pneumonic Tularemia**

We assessed the efficacy of the MSN-SS-MXF in a mouse model of pneumonic tularemia established previously for evaluation of vaccine candidates.<sup>35-37</sup> In the first of two experiments (Experiment 1), mice were infected by the intranasal route (i.n.) with 4000 CFU of *F. tularensis* LVS, a dose equivalent to about 6 times the LD<sub>50</sub>. One day later, the bacterial number in the lung increased by 1.5 logs. Without treatment, the bacteria continued to grow in the lung and disseminate to other organs. At the end of the 6-day infection period, the bacterial number reached approximately 10<sup>7</sup> in the lung and 10<sup>5</sup> - 10<sup>6</sup> in the liver and spleen (Figure 4.8A and C). One day after infection, mice were treated with 50, 100 or 200 µg of free MXF or 260 µg of the MSN-SS-MXF (loaded with 91 µg free MXF) per dose by tail vein injection every other day for a total of 3 treatment doses. During the course of infection, sham (PBS)-treated control mice suffered significant weight loss, whereas mice treated with free MXF or MSN-SS-MXF maintained their body weights (Figure 4.7A).

Bacterial burden in the lung, liver and spleen was determined on Day 6, one day after the last treatment dose. With 34.9 wt% release capacity measured under organic reducing conditions, the total amount of intracellularly releasable MXF from 260 µg of MSN-SS-MXF per treatment dose was calculated to be 91 µg. Treatment with MSN-SS-MXF reduced the bacterial burden in the lung and spleen by 3.9- and

4.3-logs, respectively; a reduction greater than that achieved by free MXF at the dose of 200  $\mu\text{g}$  (Figure 4.8C). MSN-SS-MXF treated animals also showed reduced bacterial burden in the liver to a level below that of free MXF at a dose of 100  $\mu\text{g}$ . The differences in bacterial burden reduction in the lung and spleen between treatment with MSN-SS-MXF loaded with 91  $\mu\text{g}$  MXF and treatment with an equivalent amount of free MXF (adjusted mean computed from the logit scale linear dose response curve for three doses of free drug as described in methods) were highly significant with P-values of 0.00001 and 0.00002, respectively; however, in the liver, the difference between treatment with MSN-SS-MXF and an equivalent amount of free MXF did not reach statistical significance. These results demonstrate that treatment with MSN-SS-MXF is more efficacious than treatment with an equivalent amount of free MXF in the lung and spleen with an efficacy ratio (MSN-SS-MXF : free MXF) of ~3-4 : 1 in the lung and spleen, and an efficacy ratio of ~1 : 1 in the liver.

In Experiment 2, we assayed the efficacy MSN-SS-MXF using two doses (230  $\mu\text{g}$  and 460  $\mu\text{g}$ ) of the MSN [51 wt% release capacity] and three doses (50  $\mu\text{g}$ , 150  $\mu\text{g}$  and 300  $\mu\text{g}$ ) of free MXF. Mice were infected by the intranasal route (i.n.) with 2400 CFU of *F. tularensis* LVS, a dose equivalent to about 4 times the LD<sub>50</sub>. Over the course of the *F. tularensis* infection, weight loss in sham control mice was observed after day 3 and declined steadily afterward to the end of the experiment (Figure 4.7B). In contrast, there was no net weight loss for mice treated with free MXF or MSN-SS-MXF. This confirms the observation made from the previous experiment

that the MSNs are well tolerated by the mice. Organ bacterial burdens were lowered in mice treated with increasing concentrations of MXF administered as free drug. In the lung, mice treated with 50, 150, and 300  $\mu\text{g}$  of MXF reduced bacterial burden from the level in sham-treated animals by 1.3, 2.3, and 2.9 log CFU, respectively. With a 51 wt% release capacity, mice treated with 230  $\mu\text{g}$  and 460  $\mu\text{g}$  MSN-SS-MXF per dose could release 117  $\mu\text{g}$  and 235  $\mu\text{g}$  MXF *in vivo*. The differences in bacterial burden reduction in the lung between mice treated with MSN-SS-MXF loaded with 117 or 235  $\mu\text{g}$  MXF and mice treated with an equivalent amount of free MXF (adjusted mean) were highly significant with a P-value of 0.0001 for MSN-SS-MXF loaded with 117  $\mu\text{g}$  MXF vs. an equivalent amount of free MXF and a P-value of 0.0006 for MSN-SS-MXF loaded with 235  $\mu\text{g}$  vs. an equivalent amount of free MXF. Looked at another way, CFU in the lungs of mice treated with MSN-SS-MXF loaded with 117  $\mu\text{g}$  releasable MXF was 0.75 logs lower than that of mice treated with 300  $\mu\text{g}$  of free MXF, the highest dose of free MXF tested in the experiment (Figure 4.8B). Thus, MXF delivered by the disulfide snap-top MSN is more efficacious than 3-fold the equivalent amount of free MXF in the lung.

Bacterial burden in the liver and spleen at 5 hours and 1 day post-infection were below the limit of detection for the experiment. By day 6, treatment with both doses of MSN-SS-MXF (loaded with 117 and 235  $\mu\text{g}$  MXF) kept bacterial CFU below the level obtained by treatment with 300  $\mu\text{g}$  MXF, the highest dose of free MXF tested in the experiment. In the spleen, the bacterial burdens in mice treated with either dose of MSN-SS-MXF were below the experimental limit of detection. In

contrast, *F. tularensis* LVS were detected in the liver as well as in the spleen of mice treated with all three doses of free MXF (Figure 4.8D). In this second mouse experiment, the difference in reduction of bacterial burden between mice treated with MSN-SS-MXF loaded with 117  $\mu$ g MXF and mice treated with an equivalent amount of free MXF (adjusted mean) was statistically significance for both the spleen (P value = 0.00003) and the liver (P value = 0.002). These results demonstrate that MSN-SS-MXF is much more efficacious than an equivalent amount of free MXF in the lung, spleen, and liver with an efficacy ratio (MSN-SS-MXF : free MXF) of ~5 : 1 in the lung, ~3 : 1 in the spleen, and ~3 : 1 in the liver.

We evaluated the biodistribution of the snap-top MSN following tail vein injection 24 hours after single or repeated doses in infected mice by inductively coupled plasma optical emission spectrometry (ICP-OES) analysis of the silicon content in the animal organs. The MSNs were euthanized 24 hours after a single dose (Figure 4.9A) or after 3 injections administered every other day over 5 days (Figure 4.9B). In both cases, the silica of the MSNs is found predominantly in the lung, liver, and spleen, the same three organs that are preferentially targeted by *F. tularensis*. Organs from infected mice that received repeated i.v. injections of PBS were also subjected to ICP-OES analysis. The amount of silica found in these control organs was negligible, indicating a very low background silica level in the organs (Figure 4.9C).

#### **4.4. Conclusions**

Numerous serious human infections, including those caused by

*Mycobacterium tuberculosis*, *Salmonella*, *Brucella*, *Legionella pneumophila*, and *F. tularensis*, are caused by microbes that replicate intracellularly in macrophages of the mononuclear phagocyte system. These pathogens exploit the intra-macrophage niche as a source of nutrients and a shelter against host defenses. The macrophage can also pose an obstacle to conventionally administered antibiotics that must cross its plasma membrane and often additional intracellular membranes enclosing the pathogen. Because nanoparticles are preferentially internalized by macrophages of the mononuclear phagocyte system, they are attractive as a drug delivery platform for infections cause by these pathogens. A nanoparticle delivery platform that releases drug exclusively intracellularly has the potential to release high concentrations of drug into infected cells, thus providing for a greater killing efficacy relative to free drug and at the same time limiting systemic exposure to the drug and off-target toxicities. The nanoparticle delivery platform also has the potential to improve the pharmacokinetic profile of the drug by shielding it from excretion and metabolism before it reaches its target cells. Key to the success of such a nanoparticle delivery system is a nanovalve mechanism that releases the drug cargo only after uptake of the nanoparticle into the host cell. Several different mechanisms have been developed to provide for autonomously controlled release of drug cargo from mechanized nanoparticles in response to the intracellular environment, including pH, competitive binding, enzymatic activation, and redox potential.<sup>17, 19, 31, 38-44</sup> Each system has unique chemistry and must be optimized for its drug cargo to achieve maximum loading and controlled release. In the case of the important antibiotic MXF, we have

demonstrated that we can achieve very high loading and controlled intracellular release at physiological GSH levels using MSNs functionalized with disulfide snap-tops. Indeed, loading and release of MXF into MSN-SS-MXF were far superior (release capacity 5-fold greater) to that achieved in a previous study in which we utilized pH-gated MSNs.<sup>11</sup> Consistent with this, the MSN-SS-MXF were more efficacious than the MXF-loaded pH-gated MSNs in treating pneumonic tularemia in mice, as evidenced by higher efficacy ratios vs. free drug in the lung, spleen, and liver.<sup>11</sup> MSNs taken up by macrophages will enter the endosomal-lysosomal pathway, which may have a lower concentration of GSH than the cytosol. In addition,  $\gamma$ -interferon (often elevated in infections) has been shown to lower GSH levels in macrophages.<sup>45</sup> However, lysosomes have a powerful  $\gamma$ -interferon-inducible lysosomal thiol reductase (GILT)<sup>46</sup> capable of cleaving disulfide linkages, including those present in  $\beta$ -CD-based polyrotaxanes therapeutics for lysosomal storage disease.<sup>47</sup>

Modification of the mesopores with phosphonate groups has allowed us to increase the loading and release capacity of our MSNs, and functionalization of the MSNs with a disulfide-cleavable capping system provides for very tight closure of the mesopores under extracellular conditions, preventing premature release of drug cargo, yet allows for ready opening of mesopores and release of mesopore-bound drug cargo in response to the intracellular environment. While redox-responsive disulfide gate mechanisms have been described,<sup>19, 25</sup> they have not previously been tested *in vitro* or *in vivo* for safety or efficacy in the delivery of an antibiotic for treatment of an

intracellular pathogen. Ma *et al.* used a similar cap and thread system for delivery of doxorubicin by disulfide snap-top MSNs in a cell culture system and in zebra fish,<sup>48</sup> although we have used a different synthetic route for attaching the adamantane. Most of the previously reported MSN disulfide-snap-tops have used a different chemistry for their redox sensitive gates.<sup>49-59</sup>

We have shown that our disulfide snap-top MSN loaded with MXF is safe and well tolerated *in vitro* and *in vivo*. Importantly, we demonstrated the successful treatment of a serious infectious disease, pneumonic tularemia, using the MSN-SS-MXF. In our cell culture model, the MSN-delivered MXF showed efficacy equivalent to that of free MXF. In contrast, in our *in vivo* mouse model of pneumonic tularemia, the MSN-delivered MXF was three to five times more efficacious than free drug. The difference in efficacy ratios for our *in vitro* vs. *in vivo* models likely reflects the fact that with the *in vitro* model, the macrophages in cell culture wells are exposed to a constant concentration of drug over the course of the experiment whether it is released from the MSNs or administered as free drug. In contrast, in the mouse model of pneumonic tularemia, the efficacy of the MXF administered as free drug is reduced because it is subject to metabolism and excretion and there is no preferential targeting of free drug to tissues or cells that are infected by *F. tularensis*. Hence, the MSN-delivered MXF can achieve higher levels in the infected tissues and host cells than free MXF. Indeed our ICP-OES analysis demonstrated preferential uptake of the MSN by lung, liver, and spleen, which are the main tissues infected by *F. tularensis*. In addition, because MSN-encapsulated drug is shielded from metabolism and



excretion, it is likely to have a more favorable Area Under the Curve/Minimal Inhibitory Concentration (AUC/MIC) ratio compared with free drug. The 3- to 5-fold enhanced efficacy of MSN-SS-MXF compared with free drug serves as proof-of-principle that this platform has potential to provide more effective treatment for tularemia as well as other important infections caused by bacteria that multiply intracellularly in macrophages. With our current design, the MSNs passively target infected macrophages, but it is likely that even greater enhancement of therapeutic efficacy can be achieved by surface modifications (e.g. targeting to specific cellular receptors) that further enhance targeting to infected tissues and uptake by macrophages or by use of an aerosol delivery device that delivers the MSNs directly to the lung, as has recently been demonstrated for liposomally encapsulated ciprofloxacin in treatment of tularemia.<sup>60</sup>

#### **4.5. Experimental Section**

*Materials:* Cetyltrimethylammonium bromide (CTAB, 95%), tetraorthoethyl-silicate (TEOS, 98%) 3-(trihydro-xysilyl)propyl methylphosphonate (42% in H<sub>2</sub>O), 1-adamantanethiol (95%), 2-mercaptoethanol, lead thiocyanate (99.5%),  $\beta$ -cyclodextrin ( $\geq 97\%$ ), Hoechst 33342 ( $\geq 97\%$ ), and toluene (99.8%) were purchased from Sigma (St. Louis, MO). (3-mercaptopropyl) trimethoxysilane, N-(2-Aminoethyl)-3-aminopropyltrimethoxysilane (NAPTS, 90 %) were purchased from Gelest (Morrisville, PA). Chloroform was purchased from EMC (Billerica, MA). Bromine was purchased from Fisher Scientific (Pittsburgh, PA). Chloroform was purchased from EMD (Billerica, MA).

*Synthesis of Phosphonated MSNs:* The synthesis of MCM-41 was based on well-established published procedures. Cetyltrimethylammonium bromide (CTAB, 250 mg, 0.7 mmol) was dissolved in H<sub>2</sub>O (120 mL) and NaOH (875  $\mu$ L, 2 M). The mixture was heated to 80 °C and kept stable for 30 minutes, followed by adding a mixture of tetraethyl orthosilicate (TEOS, 1.2 mL) and diethylphosphatoethyltriethoxysilane (DEPETS) (0.2 mL) drop-wise into the solution while stirring vigorously. The solution was kept at 80 °C for 2 hours and as-synthesized nanoparticles were centrifuged and washed thoroughly with methanol.

*Disulfide Snap-top Attachment on Phosphonated MSNs:* MCM-41 (100 mg) was dispersed into dry toluene (10 mL), mixed with (3-mercaptopropyl) trimethoxysilane (24  $\mu$ L, 0.1 mmol), and refluxed for 12 hours under nitrogen atmosphere. Thiol group modified MCM-41 (100 mg) was washed and dispersed again in anhydrous toluene (10 mL) in a second step. To prepare thiocyanogen, lead thiocyanate (800 mg) was dispersed in 10 mL chloroform and titrated by bromine (200  $\mu$ L) in chloroform (10 mL). The titration product mixture was filtered and the filtrate containing thiocyanogen in chloroform was light yellowish. 1-adamantanethiol (17 mg, 0.1 mmole) and as-synthesized thiocyanogen were added into the MSN toluene suspension. The disulfide oxidation reaction took four days under 4 °C and nitrogen gas atmosphere. As-synthesized material was yellowish and washed thoroughly with toluene, methanol and water.

*Loading of MXF and Drug Release Test by Continuously Monitored Fluorescence Spectroscopy:* MCM-41 (10 mg) with disulfide snap-tops was suspended in 1 mL of

40 mM MXF in PBS solution and rotated overnight.  $\beta$ -cyclodextrin (40 mg) was added into the solution as capping agent to prevent the drug from leaking out. After mixing the solution for another 12 hours, MXF loaded MCM-41 with disulfide snap-tops (MSN-SS-MXF) was dried under vacuum overnight. Release of MXF from MSN-SS-MXF in solution was measured by fluorescence spectroscopy using a 5 mW 377 nm laser beam to excite MXF in solution within a glass vial and a charge coupled device (CCD) connected to a computer to detect and collect emitted fluorescence. Specifically, the dried MSN-SS-MXF powder was put at a corner of the bottom of the glass vial containing 10 mL DI water. Baseline fluorescence spectra were collected for 1 hour to establish that there was no MXF leakage, and then 2-mercaptoethanol (200  $\mu$ L) was added to the suspension. This resulted in a dramatic increase in fluorescence emission in the supernatant fluid, indicating release of MXF. A release profile was constructed by integration of MXF emission peak area from 480 nm to 520 nm. After collecting data for 17 hours, by which time the MXF was released completely, the MXF concentration in the solution was calculated based on the UV-Vis spectrum and standard curve by Beer's law.

*Bacteria:* *Francisella tularensis* subsp. *holarctica* Live Vaccine Strain (LVS) was obtained from the Centers for Disease Control and Prevention (Atlanta, GA). For *in vitro* experiments, LVS was grown from frozen stock on GCII chocolate agar plates for 3 days prior to being used to infect macrophages. For *in vivo* experiments, pre-titered LVS frozen stock was used directly to infect mice and was serially diluted and plated on agar plates after infection to confirm bacterial CFU in the stock. For use

in the bioassay, *F. tularensis* subsp. *novicida* strain Utah 112 (*F. novicida*) was grown at 37 °C with aeration in trypticase soy broth supplemented with 0.2% cysteine (TSBC).

*F. novicida* Bioassay: MXF was eluted from 1 mg/mL of MSN-SS-MXF under a) aqueous conditions by PBS; b) aqueous reducing conditions by PBS and 2-mercaptoethanol; and c) organic reducing conditions by DMSO and 2-mercaptoethanol; mixed by end-to-end rotation for 1 hour at room temperature; and centrifuged at 10,000 g for 10 min. The supernates (1.5 µL) were added to *F. novicida* in 3 mL trypticase soy broth supplemented with 0.2% L-cysteine (TSBC) at a starting optical density (O.D.) at 540 nm of 0.05. *F. novicida* broth cultures were grown at 37 °C with shaking at 200 rpm for 6 hours. At the end of the incubation, the O.D. of the bacterial broth cultures was measured. The amount of releasable MXF from the nanoparticles was determined by comparing the O.D. of the bacterial cultures treated with the supernates to the O.D. of the cultures treated with standard concentrations of MXF.

*Macrophages:* Human monocytic THP-1 cells (ATCC TIB 202) were maintained in RPMI-1640 (Lonza) with 10% fetal bovine serum (Cellgro), 2 mM GlutaMAX (Life Technology), penicillin (100 IU) and streptomycin (100 µg/mL). Prior to use, the THP-1 cells were suspended in culture medium without antibiotics and treated with 100 nM phorbol 12-myristate 13-acetate (PMA; Sigma) for 3 days to mature the cells into a macrophage-like cell type.

*Efficacy in Killing F. tularensis in Infected Macrophages:* PMA-differentiated THP-1

macrophages were infected with *F. tularensis* LVS at a multiplicity of infection ratio of 10 bacteria to 1 THP-1 cell for 90 min at 37 °C, 5% CO<sub>2</sub> – 95% air atmosphere. Infected monolayers were washed to remove extracellular bacteria. Fresh medium with or without MXF or MSN-SS-MXF was added to the infected macrophage monolayer. The cultures were incubated in the continued presence of the treatment for one day. *F. tularensis* LVS was harvested from untreated cultures at 30 min and 1 day post infection to determine bacterial growth without treatment and from infected cultures at 1 day to assess the effect of treatment. The bacteria were harvested by lysing the infected macrophages with 1% saponin in PBS and the lysate was serially diluted and plated on GCII chocolate agar plates. Bacterial CFU on agar plates were counted after incubation at 37 °C, 5% CO<sub>2</sub> – 95% air atmosphere for 3 days.

*Efficacy in Killing F. tularensis in a Mouse Model of Pneumonic Tularemia:*

Eight-week old, female, pathogen-free Balb/c mice purchased from Taconic were acclimated for one week. Mice were infected by the intranasal route with 4000 – 8,000 CFU of *F. tularensis* LVS, a dose equivalent to about 6-12 times the LD<sub>50</sub>, respectively. Two mice were euthanized 5 hours after infection (day 0) to establish the number of bacteria in the lung at the start of the experiment. An additional 3 mice were euthanized one day later (day 1) to determine bacterial growth over that time period. Mice were then sham-treated (3 mice/group), treated with free MXF (3 mice/group for each dose) or treated with MSN-SS-MXF (4 mice/group for each dose) by tail vein injection every other day for a week (days 1, 3, and 5 for a total of 3 treatments). Mice were euthanized one day after the last treatment (day 6). Lungs,

livers, and spleens from infected mice that were sham treated or treated with free MXF or MSN-SS-MXF were homogenized in PBS, pH 7.4. The organ homogenates were serially diluted and plated on GCII chocolate agar plates containing sulfamethoxazole (40 µg/mL), trimethoprim (8 µg/mL), and erythromycin (50 µg/mL) to prevent growth of contaminants. The agar plates were incubated at 37 °C for 4 days at which time the number of bacterial colonies on each plate was counted.

*Biodistribution of MSN-SS-MXF In Vivo:* *F. tularensis*-infected mice were either sham-treated (3 mice) or treated with MSN-SS-MXF once (3 mice) or 3 times over 5 days (3 mice) and euthanized 24 hours later, at which time their organs were harvested, homogenized in PBS, digested with 0.1% HNO<sub>3</sub>, and analyzed by ICP-OES (ICPE-9000, SHIMADZU, Japan).

*Median-effect Plots:* Relative efficacies of free MXF and MSN-SS-MXF were subjected to median effect analysis. The fraction of inhibition for samples treated with different amount of MXF was calculated using bacterial CFU in base-10 logarithm (log CFU) with the equation: Fraction of inhibition = 1 – (log CFU from sample treated with a known concentration of MXF or releasable MXF from MSN-SS-MXF / log CFU from untreated sample). A median-effect plot<sup>34</sup> for MXF or MSN-SS-MXF was generated using MXF or MXF equivalent (MSN) dose in base-10 logarithm as the X-axis and the fraction of surviving bacteria divided by the fraction of killed bacteria in base-10 logarithm as the Y-axis.

*Statistics:* Statistical analyses were performed using GraphPad Prism software (version 5.01) and R 3.2.<sup>61</sup> Means were compared across groups using one way

analysis of variance (ANOVA) using the Bonferroni criteria to adjust p values for multiple comparisons. Comparisons of mean bacterial log CFU in the lung, liver and spleen between mice treated with MSN-SS-MXF or an equivalent amount of free MXF were based on a logit transform linear dose response model for the log CFU results for free drug, not assuming parallel dose response relationships. The adjusted mean for treatment with free drug was computed under this model, adjusted to the equivalent dose of MSN-SS-MXF, along with the corresponding p value for comparing the adjusted free drug mean to the MSN-SS-MXF mean. A P value of 0.05 or less was considered statistically significant.

*Study approval:* All experiments with mice were conducted within the guidelines and according to the protocol approved by the UCLA Institutional Animal Care and Use Committee.

#### 4.6. Figures and Tables

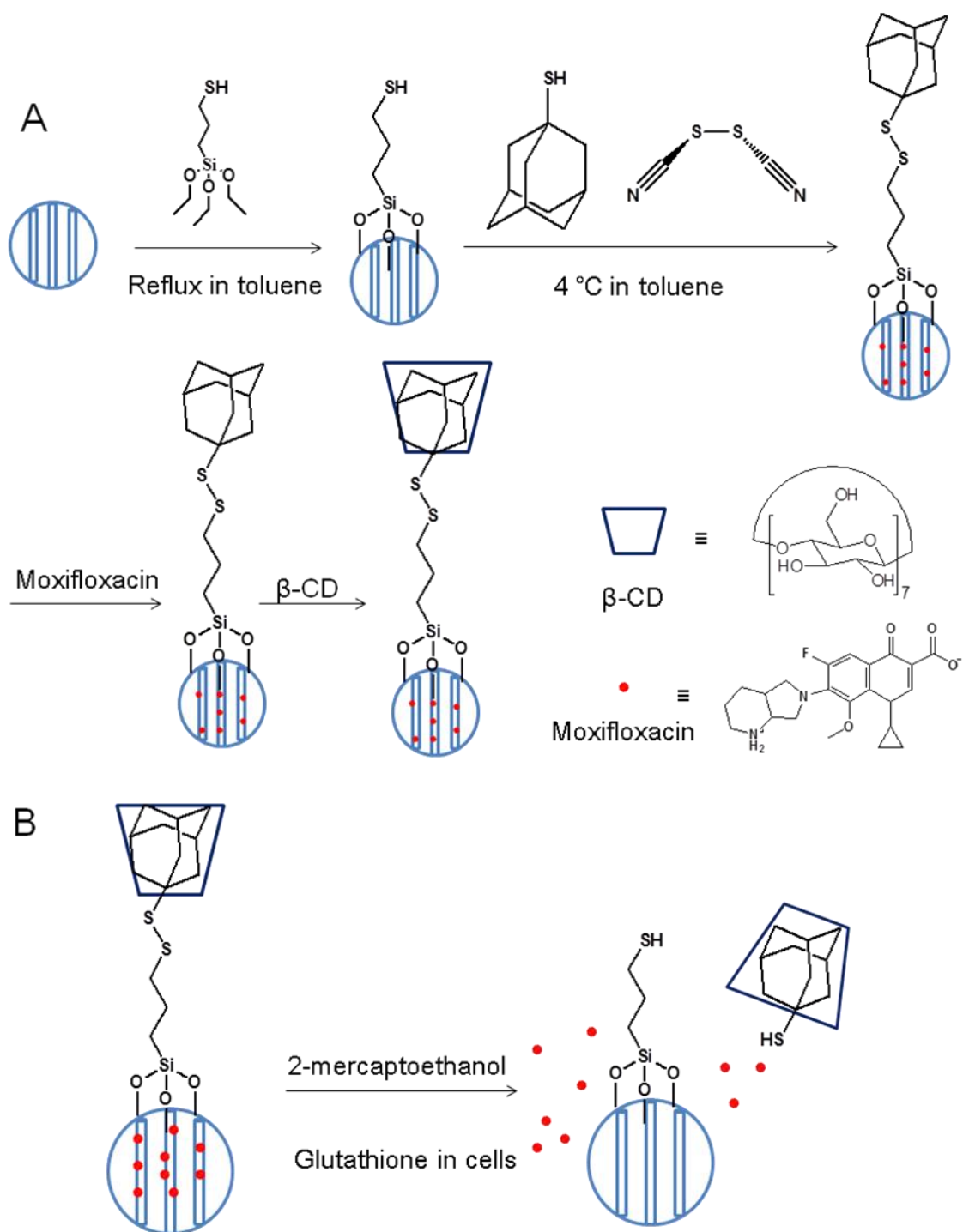


Figure 4.1. Disulfide snap-top system synthesis and release mechanism. (A) First, a silane stalk (3-mercaptopropyl) trimethoxysilane is attached to the surface of the MSN. Subsequently, 1-adamantanethiol is reacted with the silane linker in the presence of the oxidant thiocyanogen to form a disulfide bond. Disulfide modified



MSNs are then loaded with MXF, followed by the addition of  $\beta$ -cyclodextrin ( $\beta$ -CD) as the capping molecule. (B) The disulfide bond on the thread is cleaved by the reducing agent, 2-mercaptoethanol in the laboratory or glutathione inside cells, removing the bulky  $\beta$ -CD cap and releasing MXF from the pores of the nanoparticle.

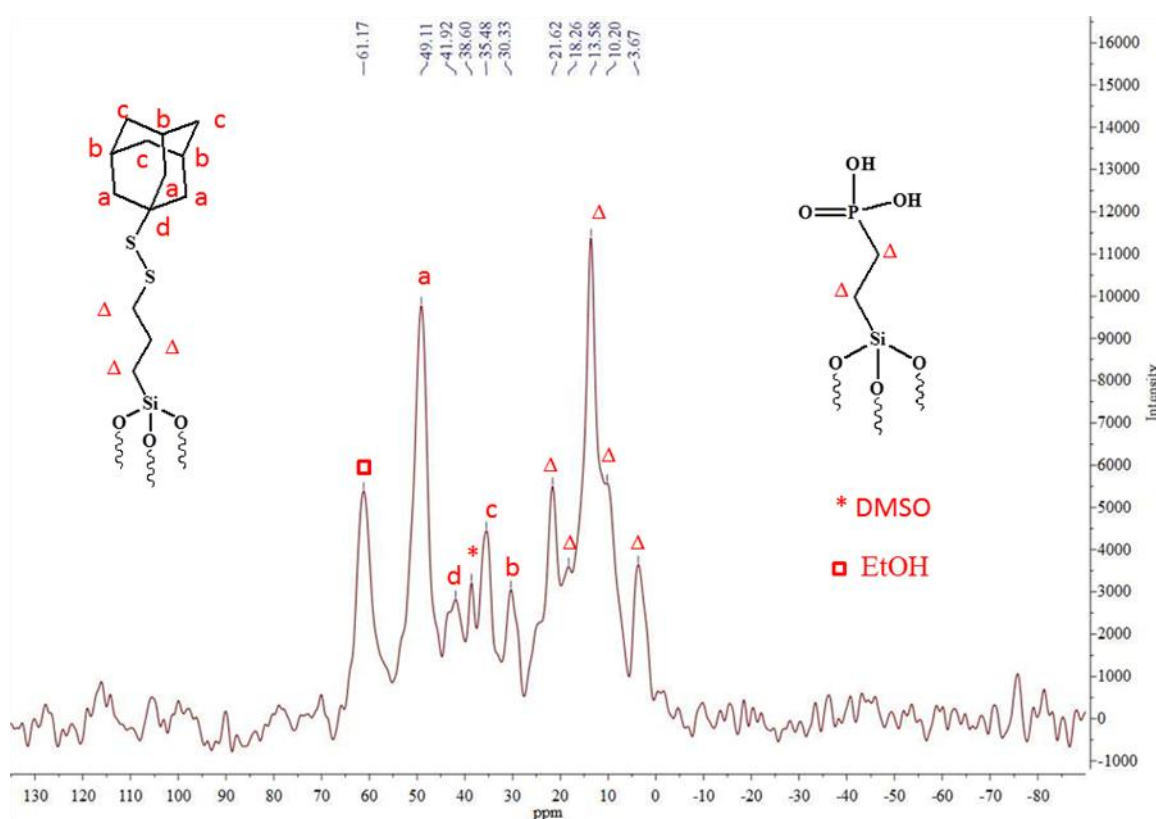


Figure 4.2. Adamantyl group attachment was confirmed by  $^{13}\text{C}$ -CPMS NMR spectroscopy

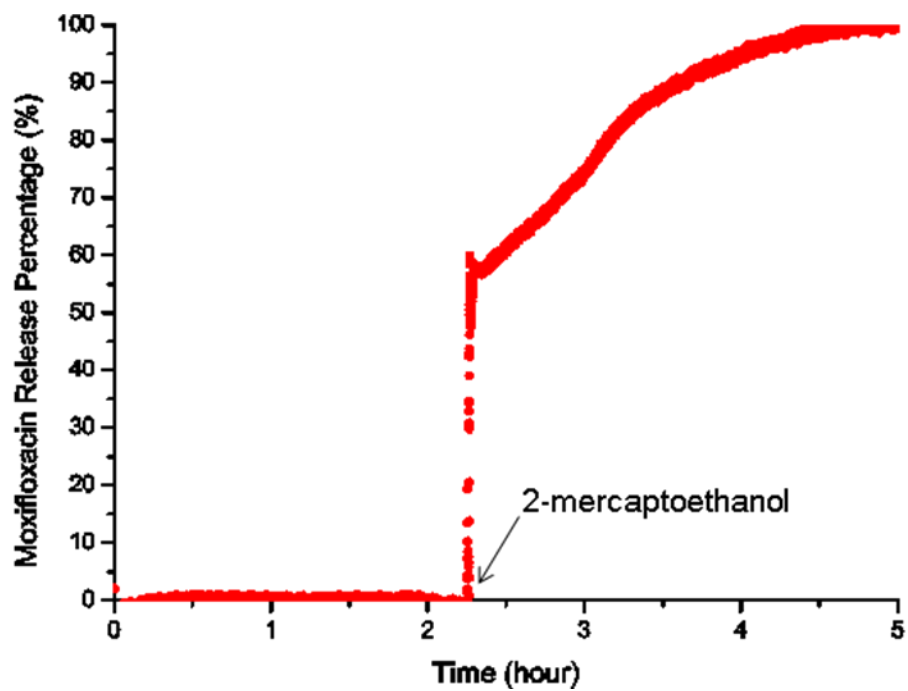


Figure 4.3. MSN-SS-MXF is released by MXF in DI water when 2-mercaptoethanol is added and cleaves the disulfide bond.

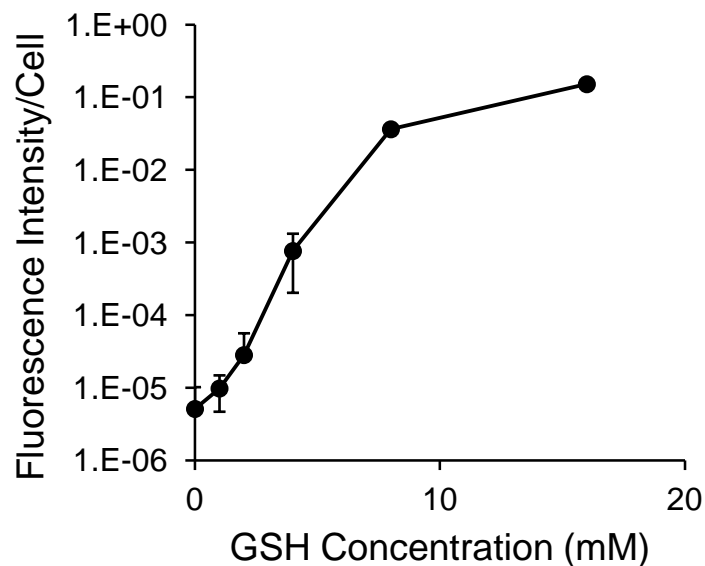


Figure 4.4. Hoechst dye release from MSN-SS snap-top by physiological concentrations of GSH. Snap-Top nanoparticles (1 mg/mL) loaded with the membrane permeant DNA stain Hoechst 33342 were incubated with various concentrations of GSH ranging from 0 – 16 mM, as indicated, overnight at room temperature. The nanoparticles were pelleted by centrifugation and the supernate was diluted 20-fold with RPMI culture medium and added to THP-1 cells. Cells were incubated for 3 hours at 37 °C, stained with WGA-AlexaFluor 633, fixed, and examined by fluorescence microscopy with fixed exposure and gain settings. Data are relative fluorescence intensity of the Hoechst staining per cell as quantitated using CellProfiler.

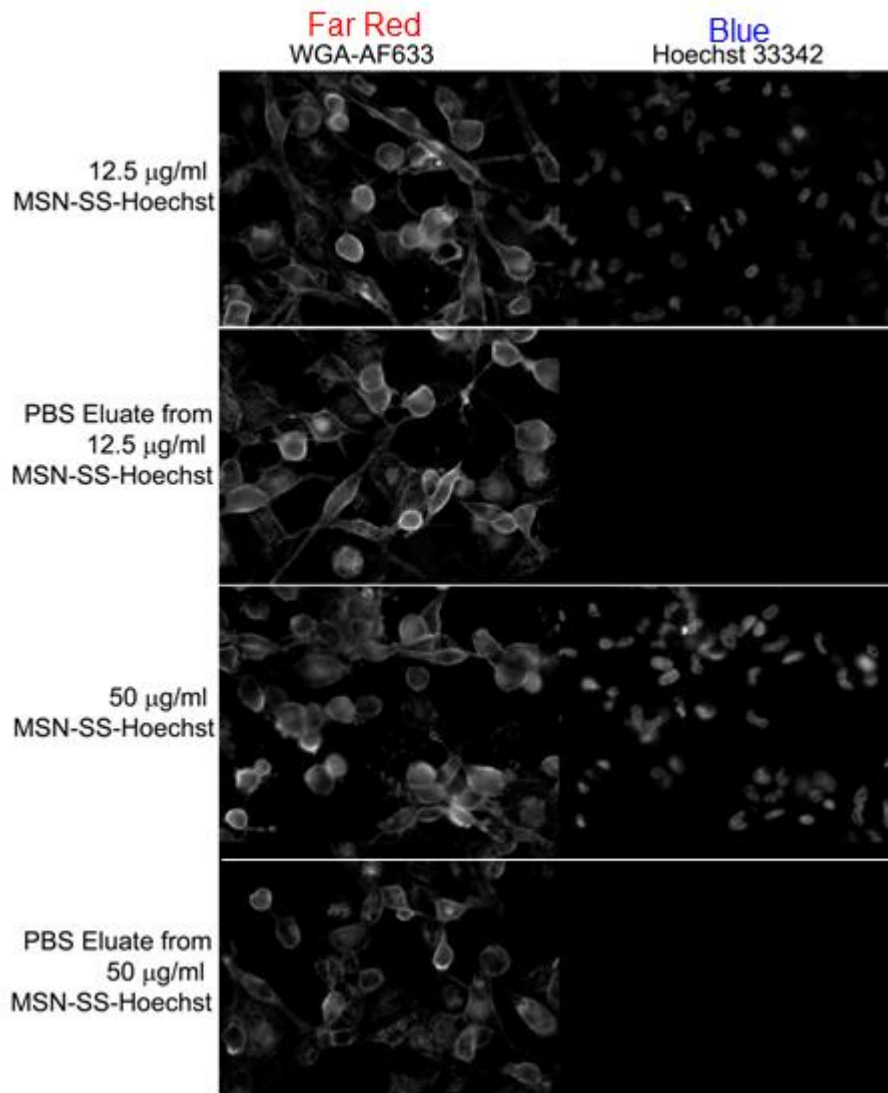


Figure 4.5. MSN-SS-Hoechst but not their PBS eluates stain the nuclei of THP-1 cells. THP-1 macrophages were incubated with snap-top MSNs loaded with the membrane permeant DNA stain Hoechst 33342 (MSN-SS-Hoechst) or the PBS eluate from MSN-SS-Hoechst for 18 h, fixed with 4% paraformaldehyde, and incubated with Alexa Fluor 633-conjugated wheat germ agglutinin (WGA) to stain the plasma membrane of the cells. Images were acquired with a Nikon Optishot microscope equipped with SPOT RKT camera using SPOT software and fixed exposure and gain settings.

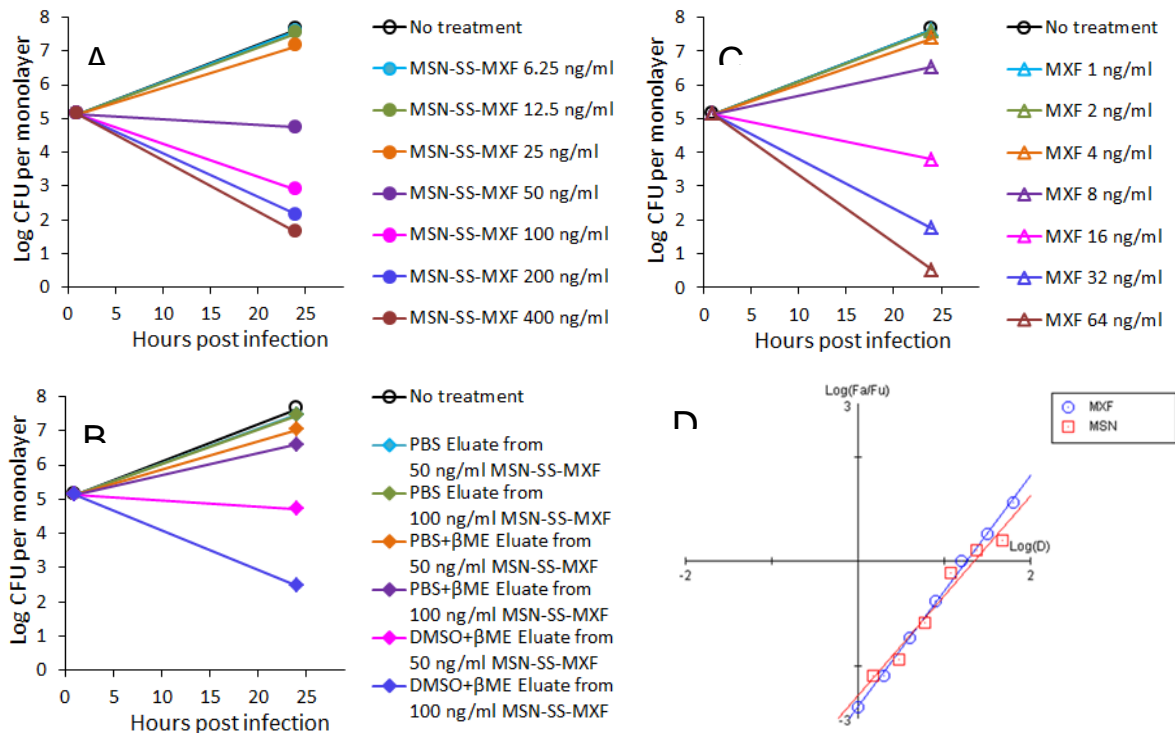


Figure 4.6. MSN-SS-MXF is as effective as MXF in killing *F. tularensis* in human macrophages. PMA-differentiated THP-1 macrophages were infected with *F. tularensis* LVS and treated with various doses of MSN-SS-MXF (A), eluates prepared from MSN-SS-MXF incubated in aqueous PBS with and without reducing agent 2-mercaptoethanol ( $\beta$ ME) or in DMSO with  $\beta$ ME (B) or free MXF (C). Bacterial colony forming units (CFU) in the macrophages with or without treatment were determined at 30 min and 24 hours post infection. (D) The impact of MSN-SS-MXF and MXF treatment on bacterial viability was compared using median-effect analysis. Median-effect curves generated by CompuSyn for free MXF and an equivalent amount of MXF on the nanoparticle (MSN) were plotted in the same graph. Log(D) is dose of free MXF or MXF equivalent of MSN-SS-MXF in logarithm; Log(Fa/Fu) is

the division of the fraction of bacteria killed ( $F_a$ ) by the fraction of bacteria surviving ( $F_u$ ) in logarithm.

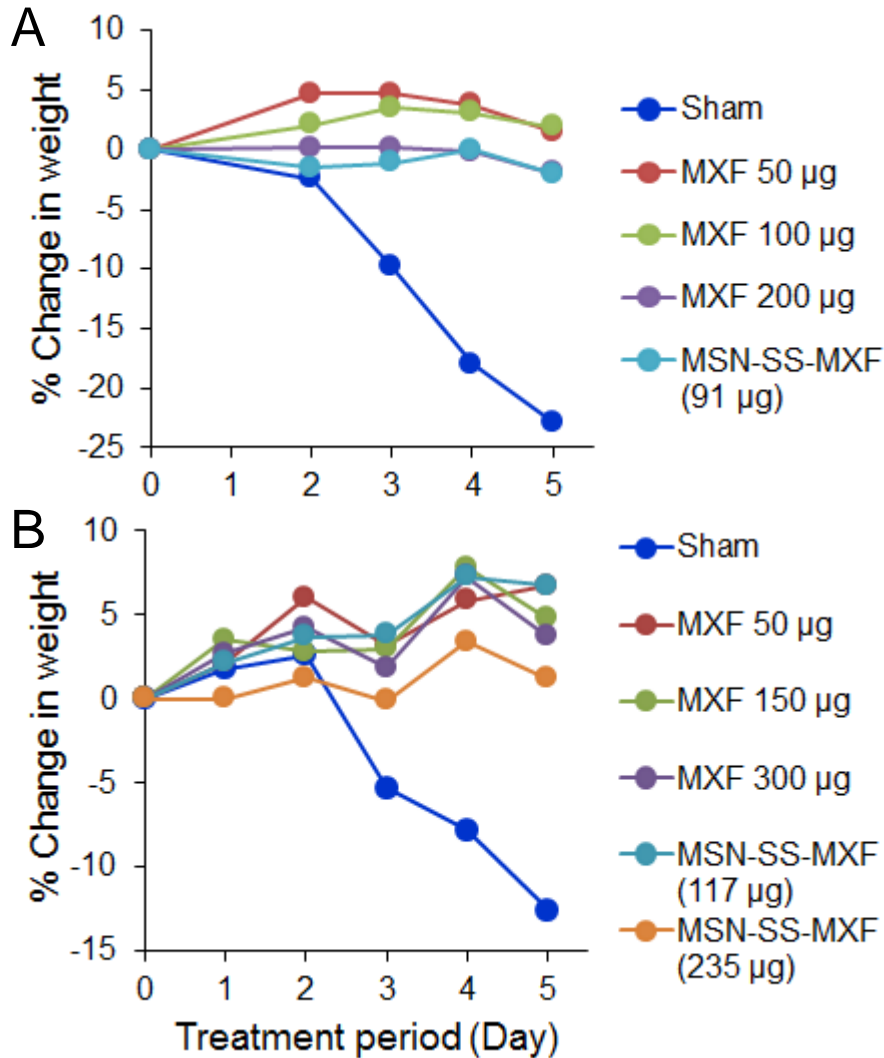


Figure 4.7. Treatment with MSN-SS-MXF prevents weight loss in mice infected with *E. tularensis*. Mice with pneumonic tularemia were weighed daily during the course of treatment. (A and B) Data shown are percentage change in weight of mice in two independent experiments. The mice were sham-treated, treated with three different doses of the broad spectrum antibiotic MXF administered as a free drug, or treated

with one or two doses of MSN-SS-MXF, as indicated.

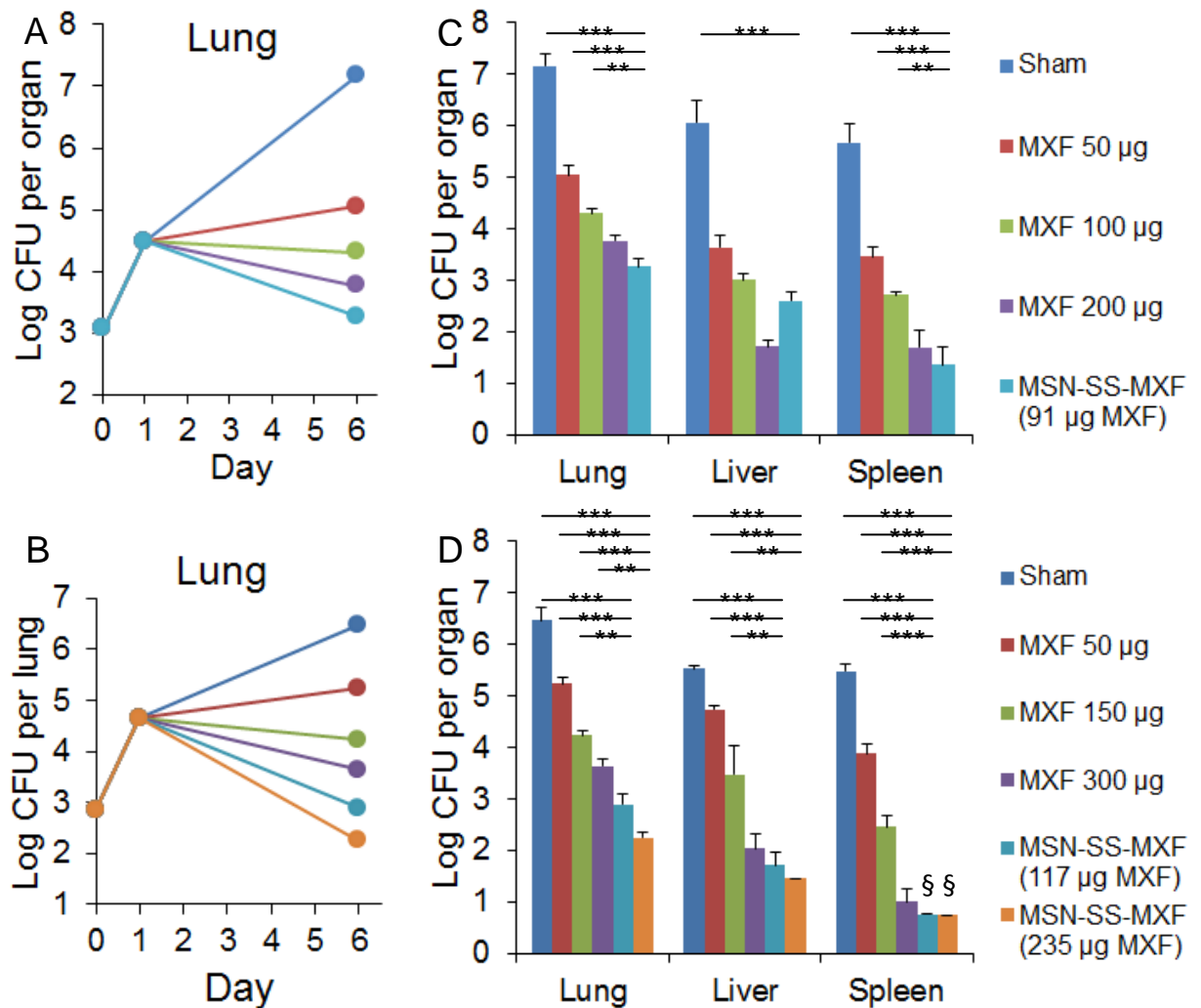


Figure 4.8. *In vivo* efficacy of MSN-SS-MXF in two independent experiments, Experiment 1 (A and C) and Experiment 2 (B and D). Mice were infected with *F. tularensis* LVS by the intranasal route. (A and B) Bacterial burden in the lung was monitored over the course of infection. One day post-infection, mice were sham-treated (3 mice/group), treated with one of the three doses of free MXF as indicated (3 mice/group), or treated with MXF delivered by the disulfide snap-top MSN (MSN-SS-MXF) by tail vein injection (4 mice/group). (C and D) The effect of each treatment on *F. tularensis* burden in lung, liver, and spleen was determined by assaying the bacterial CFU one day after the final treatment. The equivalent amount



of free MXF for the MSN-SS-MXF is shown in parenthesis. Statistics were analyzed using one-way ANOVA with Bonferroni post-test correction. \*\* $p < 0.01$ , \*\*\* $p < 0.001$ . Error bars represent standard errors. § Bacterial CFU below limit of detection.

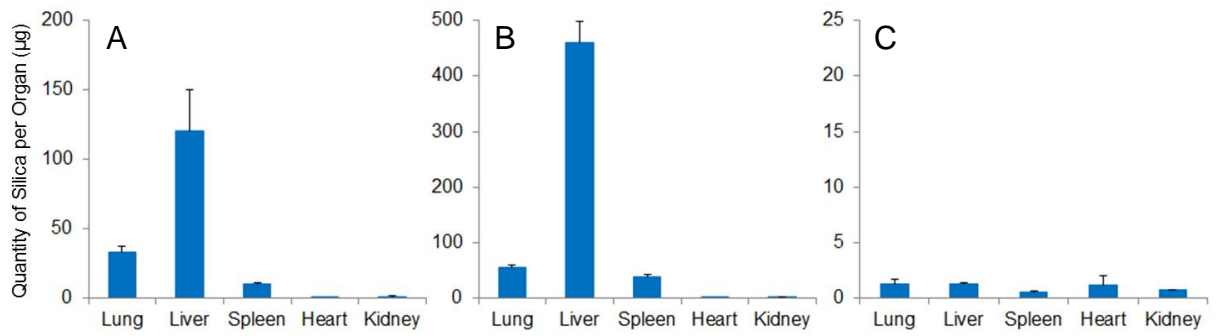


Figure 4.9. Distribution of MSN-SS-MXF in animal organs. Mice were injected via tail vein with a single dose (A) or three doses (B) of MSN-SS-MXF (460 µg) every other day over 5 days or sham-treated with three doses PBS every other day over 5 days (C) and euthanized 24 hours after the last injection. Lung, liver, spleen, heart and kidney were assayed for silica by ICP-OES analysis. A similar distribution pattern is observed after a single (A) or three repeated injections (B) of MSN-SS-MXF, with the majority of the silica found in the liver, lung and spleen. Sham-treated mice showed low background levels of silica in their organs; note different scales in the three figures (C). Data represent means  $\pm$  standard errors of results from 3 mice per experimental condition with 3 technical repeats per mouse.

Table 4.1. MSN-SS-MXF release capacity measurement with methods I and II

Measurement	PBS (wt%)	PBS + $\beta$ -ME	DMSO	DMSO + $\beta$ -ME
UV-Vis	9.14 %	21.11 %	72.68 %	133.28 %
Bioassay	11.97 %	18.05 %	48.00 %	51.26 %

Table 4.2. Optimization of Uptake and Release Capacity

A. Influence of inner pore charges on MSNs uptake and release capacities

Inner Pore Charges	Uptake Capacity (wt%)	Release Capacity (wt%)
Positive	~ 0	~ 0
Negative	30.0	3.0

B. Influence of amount of phosphonate groups on MSN-SS uptake and release capacities

Amount of DEPETS ( $\mu$ L)	Uptake Capacity (wt%)	Release Capacity (wt%)
10	28.8	2.9
25	17.0	2.4
35	22.0	2.1

C. Influence of loading pH on MSN-SS uptake capacity

Loading pH	Uptake Capacity (wt%)
3	9.6
7.4	22.2

D. Influence of disulfide stalk surface coverage on MSN-SS uptake capacity

Amount of Disulfide Stalk Surface Coverage (10 mg MSNs)	Uptake Capacity (wt%)
10 $\mu$ mol	22.2
20 $\mu$ mol	19.7

E. Influence of MXF loading concentration on MSN-SS uptake and release capacities

MXF Loading Concentration	Uptake Capacity (wt%)	Release Capacity (wt%)
10 mM	30	3
40 mM	135	51

#### 4.7. References

1. Saslaw, S.; Eigelsbach, H. T.; Prior, J. A.; Wilson, H. E.; Carhart, S., Tularemia vaccine study. II. Respiratory challenge. *Arch. Intern. Med.* 1961, 107, 702-714.
2. Harris, S., Japanese biological warfare research on humans: a case study of microbiology and ethics. *Ann. N. Y. Acad. Sci.* 1992, 666, 21-52.
3. Dennis, D. T.; Inglesby, T. V.; Henderson, D. A.; Bartlett, J. G.; Ascher, M. S.; Eitzen, E.; Fine, A. D.; Friedlander, A. M.; Hauer, J.; Layton, M.; Lillibridge, S. R.; McDade, J. E.; Osterholm, M. T.; O'Toole, T.; Parker, G.; Perl, T. M.; Russell, P. K.; Tonat, K., Tularemia as a biological weapon: medical and public health management. *JAMA* 2001, 285, 2763-2773.
4. Oyston, P. C.; Sjostedt, A.; Titball, R. W., Tularaemia: bioterrorism defence renews interest in *Francisella tularensis*. *Nat. Rev. Microbiol.* 2004, 2, 967-978.
5. Twenhafel, N. A.; Alves, D. A.; Purcell, B. K., Pathology of inhalational *Francisella tularensis* spp. *tularensis* SCHU S4 infection in African green monkeys (*Chlorocebus aethiops*). *Vet Pathol* 2009, 46, 698-706.
6. Chen, H.; Wang, L.; Yeh, J.; Wu, X.; Cao, Z.; Wang, Y. A.; Zhang, M.; Yang, L.; Mao, H., Reducing non-specific binding and uptake of nanoparticles and improving cell targeting with an antifouling PEO-b-PgammaMPS copolymer coating. *Biomaterials* 2010, 31, 5397-5407.
7. Lee, J. E.; Lee, N.; Kim, H.; Kim, J.; Choi, S. H.; Kim, J. H.; Kim, T.; Song, I. C.; Park, S. P.; Moon, W. K.; Hyeon, T., Uniform mesoporous dye-doped silica nanoparticles decorated with multiple magnetite nanocrystals for simultaneous

enhanced magnetic resonance imaging, fluorescence imaging, and drug delivery. *J Am Chem Soc* 2010, 132, 552-557.

8. He, Q.; Zhang, Z.; Gao, F.; Li, Y.; Shi, J., In vivo biodistribution and urinary excretion of mesoporous silica nanoparticles: effects of particle size and PEGylation. *Small* 2011, 7, 271-280.

9. Ungaro, F.; d'Angelo, I.; Coletta, C.; d'Emmanuele di Villa Bianca, R.; Sorrentino, R.; Perfetto, B.; Tufano, M. A.; Miro, A.; La Rotonda, M. I.; Quaglia, F., Dry powders based on PLGA nanoparticles for pulmonary delivery of antibiotics: modulation of encapsulation efficiency, release rate and lung deposition pattern by hydrophilic polymers. *J Control Release* 2012, 157, 149-159.

10. Pinto-Alphandary, H.; Andremont, A.; Couvreur, P., Targeted delivery of antibiotics using liposomes and nanoparticles: research and applications. *Int J Antimicrob Agents* 2000, 13, 155-168.

11. Li, Z.; Clemens, D. L.; Lee, B.-Y.; Dillon, B. J.; Horwitz, M. A.; Zink, J. I., Mesoporous Silica Nanoparticles with pH-Sensitive Nanovalves for Delivery of Moxifloxacin Provide Improved Treatment of Lethal Pneumonic Tularemia. *ACS Nano* [Online early access]. DOI: 10.1021/acsnano.5b04306. Published Online: Oct 5, 2015.

12. Hwang, A. A.; Lee, B. Y.; Clemens, D. L.; Dillon, B. J.; Zink, J. I.; Horwitz, M. A., pH-Responsive Isoniazid-Loaded Nanoparticles Markedly Improve Tuberculosis Treatment in Mice. *Small* 2015, 11, 5065- 5078.

13. Clemens, D. L.; Lee, B. Y.; Xue, M.; Thomas, C. R.; Meng, H.; Ferris, D.; Nel, A.

- E.; Zink, J. I.; Horwitz, M. A., Targeted intracellular delivery of antituberculosis drugs to *Mycobacterium tuberculosis*-infected macrophages via functionalized mesoporous silica nanoparticles. *Antimicrob Agents Chemother* 2012, 56, 2535-2545.
14. Tarn, D.; Ashley, C. E.; Xue, M.; Carnes, E. C.; Zink, J. I.; Brinker, C. J., Mesoporous Silica Nanoparticle Nanocarriers: Biofunctionality and Biocompatibility. *Acc Chem Res* 2013, 46, 792–801.
15. Argyo, C.; Weiss, V.; Br äuchle, C.; Bein, T., Multifunctional Mesoporous Silica Nanoparticles as a Universal Platform for Drug Delivery. *Chemistry of Materials* 2014, 26, 435-451.
16. Wu, S.-H.; Mou, C.-Y.; Lin, H.-P., Synthesis of mesoporous silica nanoparticles. *Chemical Society Reviews* 2013, 42, 3862-3875.
17. Li, Z.; Barnes, J. C.; Bosoy, A.; Stoddart, J. F.; Zink, J. I., Mesoporous silica nanoparticles in biomedical applications. *Chem Soc Rev* 2012, 41, 2590-2605.
18. Hwang, C.; Sinskey, A. J.; Lodish, H. F., Oxidized redox state of glutathione in the endoplasmic reticulum. *Science* 1992, 257, 1496-1502.
19. Ambrogio, M. W.; Pecorelli, T. A.; Patel, K.; Khashab, N. M.; Trabolsi, A.; Khatib, H. A.; Botros, Y. Y.; Zink, J. I.; Stoddart, J. F., Snap-top nanocarriers. *Org Lett* 2010, 12, 3304-3307.
20. Go, Y. M.; Jones, D. P., Redox compartmentalization in eukaryotic cells. *Biochimica et biophysica acta* 2008, 1780, 1273-1290.
21. Schafer, F. Q.; Buettner, G. R., Redox environment of the cell as viewed through the redox state of the glutathione disulfide/glutathione couple. *Free radical biology &*

medicine 2001, 30, 1191-1212.

22. Jones, D. P.; Mody, V. C., Jr.; Carlson, J. L.; Lynn, M. J.; Sternberg, P., Jr., Redox analysis of human plasma allows separation of pro-oxidant events of aging from decline in antioxidant defenses. *Free radical biology & medicine* 2002, 33, 1290-1300.

23. Jones, D. P.; Carlson, J. L.; Mody, V. C.; Cai, J.; Lynn, M. J.; Sternberg, P., Redox state of glutathione in human plasma. *Free radical biology & medicine* 2000, 28, 625-635.

24. Anderson, C. L.; Iyer, S. S.; Ziegler, T. R.; Jones, D. P., Control of extracellular cysteine/cystine redox state by HT-29 cells is independent of cellular glutathione. *American journal of physiology. Regulatory, integrative and comparative physiology* 2007, 293, R1069-1075.

25. Guardado-Alvarez, T. M.; Devi, L. S.; Vabre, J. M.; Pecorelli, T. A.; Schwartz, B. J.; Durand, J. O.; Mongin, O.; Blanchard-Desce, M.; Zink, J. I., Photo-redox activated drug delivery systems operating under two photon excitation in the near-IR. *Nanoscale* 2014, 6, 4652-4658.

26. Russell, P.; Eley, S. M.; Fulop, M. J.; Bell, D. L.; Titball, R. W., The efficacy of ciprofloxacin and doxycycline against experimental tularaemia. *J Antimicrob Chemother* 1998, 41, 461-465.

27. Chocarro, A.; Gonzalez, A.; Garcia, I., Treatment of tularemia with ciprofloxacin. *Clin Infect Dis* 2000, 31, 623.

28. Steward, J.; Piercy, T.; Lever, M. S.; Simpson, A. J.; Brooks, T. J., Treatment of



murine pneumonic *Francisella tularensis* infection with gatifloxacin, moxifloxacin or ciprofloxacin. *Int J Antimicrob Agents* 2006, 27, 439-443.

29. Nuermberger, E. L.; Yoshimatsu, T.; Tyagi, S.; O'Brien, R. J.; Vernon, A. N.; Chaisson, R. E.; Bishai, W. R.; Grosset, J. H., Moxifloxacin-containing regimen greatly reduces time to culture conversion in murine tuberculosis. *Am J Respir Crit Care Med* 2004, 169, 421-426.

30. Grayo, S.; Join-Lambert, O.; Desroches, M. C.; Le Monnier, A., Comparison of the in vitro efficacies of moxifloxacin and amoxicillin against *Listeria monocytogenes*. *Antimicrob Agents Chemother* 2008, 52, 1697-1702.

31. Meng, H.; Xue, M.; Xia, T.; Zhao, Y. L.; Tamanoi, F.; Stoddart, J. F.; Zink, J. I.; Nel, A. E., Autonomous in vitro anticancer drug release from mesoporous silica nanoparticles by pH-sensitive nanovalves. *J Am Chem Soc* 2010, 132, 12690-12697.

32. Meister, A., Glutathione metabolism and its selective modification. *J Biol Chem* 1988, 263, 17205-17208.

33. Morgan, B.; Ezerina, D.; Amoako, T. N.; Riemer, J.; Seedorf, M.; Dick, T. P., Multiple glutathione disulfide removal pathways mediate cytosolic redox homeostasis. *Nat Chem Biol* 2013, 9, 119-125.

34. Chou, T. C., Theoretical basis, experimental design, and computerized simulation of synergism and antagonism in drug combination studies. *Pharmacol Rev* 2006, 58, 621-681.

35. Jia, Q. M.; Bowen, R.; Sahakian, J.; Dillon, B. J.; Horwitz, M. A., A Heterologous Prime-Boost Vaccination Strategy Comprising the *Francisella tularensis* Live Vaccine

Strain capB Mutant and Recombinant Attenuated *Listeria monocytogenes* Expressing *F. tularensis* IglC Induces Potent Protective Immunity in Mice against Virulent *F. tularensis* Aerosol Challenge. *Infect. Immun.* 2013, 81, 1550-1561.

36. Jia, Q.; Lee, B. Y.; Clemens, D. L.; Bowen, R. A.; Horwitz, M. A., Recombinant attenuated *Listeria monocytogenes* vaccine expressing *Francisella tularensis* IglC induces protection in mice against aerosolized Type A *F. tularensis*. *Vaccine* 2009, 27, 1216-1229.

37. Jia, Q.; Lee, B. Y.; Bowen, R.; Dillon, B. J.; Som, S. M.; Horwitz, M. A., A *Francisella tularensis* live vaccine strain (LVS) mutant with a deletion in capB, encoding a putative capsular biosynthesis protein, is significantly more attenuated than LVS yet induces potent protective immunity in mice against *F. tularensis* challenge. *Infect. Immun.* 2010, 78, 4341-4355.

38. Angelos, S.; Khashab, N. M.; Yang, Y. W.; Trabolsi, A.; Khatib, H. A.; Stoddart, J. F.; Zink, J. I., pH clock-operated mechanized nanoparticles. *J Am Chem Soc* 2009, 131, 12912-12914.

39. Patel, K.; Angelos, S.; Dichtel, W. R.; Coskun, A.; Yang, Y. W.; Zink, J. I.; Stoddart, J. F., Enzyme-responsive snap-top covered silica nanocontainers. *J Am Chem Soc* 2008, 130, 2382-2383.

40. Angelos, S.; Yang, Y. W.; Patel, K.; Stoddart, J. F.; Zink, J. I., pH-responsive supramolecular nanovalves based on cucurbit[6]uril pseudorotaxanes. *Angew Chem Int Ed Engl* 2008, 47, 2222-2226.

41. Ambrogio, M. W.; Thomas, C. R.; Zhao, Y. L.; Zink, J. I.; Stoddart, J. F.,

Mechanized silica nanoparticles: a new frontier in theranostic nanomedicine. *Acc Chem Res* 2011, 44, 903-913.

42. Xue, M.; Zhong, X.; Shaposhnik, Z.; Qu, Y.; Tamanoi, F.; Duan, X.; Zink, J. I., pH-Operated mechanized porous silicon nanoparticles. *J Am Chem Soc* 2011, 133, 8798-8801.

43. Liong, M.; Angelos, S.; Choi, E.; Patel, K.; Stoddart, J. F.; Zink, J. I., Mesostructured multifunctional nanoparticles for imaging and drug delivery. *Journal of Materials Chemistry* 2009, 19, 6251-6257.

44. Liong, M.; Lu, J.; Kovoichich, M.; Xia, T.; Ruehm, S. G.; Nel, A. E.; Tamanoi, F.; Zink, J. I., Multifunctional inorganic nanoparticles for imaging, targeting, and drug delivery. *ACS Nano* 2008, 2, 889-896.

45. Venketaraman, V.; Dayaram, Y. K.; Amin, A. G.; Ngo, R.; Green, R. M.; Talaue, M. T.; Mann, J.; Connell, N. D., Role of glutathione in macrophage control of mycobacteria. *Infect. Immun.* 2003, 71, 1864-1871.

46. Arunachalam, B.; Phan, U. T.; Geuze, H. J.; Cresswell, P., Enzymatic reduction of disulfide bonds in lysosomes: characterization of a gamma-interferon-inducible lysosomal thiol reductase (GILT). *Proc. Natl. Acad. Sci. U. S. A.* 2000, 97, 745-750.

47. Tamura, A.; Yui, N., Lysosomal-specific cholesterol reduction by biocleavable polyrotaxanes for ameliorating Niemann-Pick type C disease. *Scientific reports* 2014, 4, 4356.

48. Ma, X.; Teh, C.; Zhang, Q.; Borah, P.; Choong, C.; Korzh, V.; Zhao, Y., Redox-responsive mesoporous silica nanoparticles: a physiologically sensitive

codelivery vehicle for siRNA and doxorubicin. *Antioxid Redox Signal* 2014, 21, 707-722.

49. Zhao, Q.; Wang, C.; Liu, Y.; Wang, J.; Gao, Y.; Zhang, X.; Jiang, T.; Wang, S., PEGylated mesoporous silica as a redox-responsive drug delivery system for loading thiol-containing drugs. *Int J Pharm* 2014, 477, 613-622.

50. Zhao, Q.; Geng, H.; Wang, Y.; Gao, Y.; Huang, J.; Wang, Y.; Zhang, J.; Wang, S., Hyaluronic acid oligosaccharide modified redox-responsive mesoporous silica nanoparticles for targeted drug delivery. *ACS Appl Mater Interfaces* 2014, 6, 20290-20299.

51. Zhang, J.; Niemela, M.; Westermarck, J.; Rosenholm, J. M., Mesoporous silica nanoparticles with redox-responsive surface linkers for charge-reversible loading and release of short oligonucleotides. *Dalton transactions* 2014, 43, 4115-4126.

52. Zhang, B.; Luo, Z.; Liu, J.; Ding, X.; Li, J.; Cai, K., Cytochrome c end-capped mesoporous silica nanoparticles as redox-responsive drug delivery vehicles for liver tumor-targeted triplex therapy in vitro and in vivo. *J Control Release* 2014, 192, 192-201.

53. Yi, Z.; Hussain, H. I.; Feng, C.; Sun, D.; She, F.; Rookes, J. E.; Cahill, D. M.; Kong, L., Functionalized Mesoporous Silica Nanoparticles with Redox-Responsive Short-Chain Gatekeepers for Agrochemical Delivery. *ACS Appl Mater Interfaces* 2015, 7, 9937-9946.

54. Wang, Y.; Han, N.; Zhao, Q.; Bai, L.; Li, J.; Jiang, T.; Wang, S., Redox-responsive mesoporous silica as carriers for controlled drug delivery: A comparative study based

on silica and PEG gatekeepers. *European journal of pharmaceutical sciences : official journal of the European Federation for Pharmaceutical Sciences* 2015, 72, 12-20.

55. Wan, X.; Wang, D.; Liu, S., Fluorescent pH-sensing organic/inorganic hybrid mesoporous silica nanoparticles with tunable redox-responsive release capability. *Langmuir* 2010, 26, 15574-15579.

56. Sun, J. T.; Piao, J. G.; Wang, L. H.; Javed, M.; Hong, C. Y.; Pan, C. Y., One-pot synthesis of redox-responsive polymers-coated mesoporous silica nanoparticles and their controlled drug release. *Macromolecular rapid communications* 2013, 34, 1387-1394.

57. Nadrah, P.; Porta, F.; Planinsek, O.; Kros, A.; Gaberscek, M., Poly(propylene imine) dendrimer caps on mesoporous silica nanoparticles for redox-responsive release: smaller is better. *Physical chemistry chemical physics : PCCP* 2013, 15, 10740-10748.

58. Luo, Z.; Cai, K.; Hu, Y.; Zhao, L.; Liu, P.; Duan, L.; Yang, W., Mesoporous silica nanoparticles end-capped with collagen: redox-responsive nanoreservoirs for targeted drug delivery. *Angew Chem Int Ed Engl* 2011, 50, 640-643.

59. Dai, L.; Li, J.; Zhang, B.; Liu, J.; Luo, Z.; Cai, K., Redox-responsive nanocarrier based on heparin end-capped mesoporous silica nanoparticles for targeted tumor therapy in vitro and in vivo. *Langmuir* 2014, 30, 7867-7877.

60. Hamblin, K. A.; Wong, J. P.; Blanchard, J. D.; Atkins, H. S., The potential of liposome-encapsulated ciprofloxacin as a tularemia therapy. *Front Cell Infect Microbiol* 2014, 4, 79.

61. R Core Team., R: A language and environment for statistical computing. . R Foundation for Statistical Computing, Vienna, Austria. **2015**, <http://www.R-project.org/>.

## Chapter 5

Measurement of Uptake and Release Capacities of Fe<sub>3</sub>O<sub>4</sub>@SiO<sub>2</sub> Mesoporous Silica Nanoparticles Modified With pH-Sensitive Nanovalve and its thermally triggered release test

## 5.1. Abstract

Uniformly size distributed  $\text{Fe}_3\text{O}_4@\text{SiO}_2$  core/shell nanoparticles were synthesized, with different core sizes and particle diameters.  $\text{Fe}_3\text{O}_4@\text{SiO}_2$  has a radial mesopore structure originating from the core instead of a 2D hexagonal mesoporous structure. The central space occupation by iron oxide core and its surrounding stabilizing ligands were expected to influence its capacity for loading. We have investigated how much drug can be uptake and released with this specific structure. Hoechst 33342, a fluorescent stain for DNA in nuclei was employed as the drug model. Experimental results show that uptake capacity increases with loading concentrations and reaches a saturation point of around 15 wt% when loaded from a 20 mM Hoechst solution. On the other hand, the release capacity increases at first and reaches highest value at 10 mM Hoechst loading, and then gradually decreases due to increase of binding between excess Hoechst and cyclodextrin (CD) caps from the pH-sensitive nanovalve introduced in chapter 3. Therefore the optimal loading concentrations for uptake capacity and release capacity are different. Moreover, we find that external heating triggers a small amount of Hoechst release, compared with the release caused by pH change. The  $\text{Fe}_3\text{O}_4$  core can generate heat and increase its surrounding temperature under an oscillating magnetic field. However, the temperature change of superparamagnetic  $\text{Fe}_3\text{O}_4$  exposed to oscillating magnetic pulses is not sufficient to trigger the release of Hoechst or Propidium iodide (PI) effectively.

## 5.2. Introduction

There has been extensive research on utilizing mesoporous silica nanoparticle for



drug delivery by chemically modifying its outer surface with polymer, nanovalve, protein, etc. We are making use of the inner space of MSNs, and synthesizing mesoporous silica materials surrounding other materials to combine physical and chemical properties of various materials. Magnetic nanocrystal is one of the nano materials which can serve as a therapeutic and imaging reagent.<sup>1</sup> Combining magnetic nano materials with MSNs helps induce hyperthermia effect and T<sub>2</sub>-weighted magnetic resonance imaging contrast.<sup>2</sup> Iron oxide with diameter smaller than 20 nm has single domain and behaves as superparamagnetic material.<sup>3</sup> With embedded iron oxide, the Fe<sub>3</sub>O<sub>4</sub>@SiO<sub>2</sub> core/shell nanoparticle has the advantages of generating heat, which can facilitate controlled drug release when exposed to oscillating magnetic field, as well as targeting tissues through attraction of permanent magnet and serving as MRI contrast to observe distribution for *in vivo* study.<sup>4-8</sup>

The synthesis methods of Fe<sub>3</sub>O<sub>4</sub>@SiO<sub>2</sub> have been developed for several years. It is not difficult to coat Fe<sub>3</sub>O<sub>4</sub> with mesoporous silica layer; however, the resulting core/shell nanoparticles always have a wide size distribution and imperfect sphere shape. Moreover, the iron oxide core is not evenly embedded into each particle, and the resulting particles may contain none, single, or multiple cores. Among the reported methods, Hyeon<sup>2</sup> and co-workers successfully developed a method to make uniformly dispersed and single core Fe<sub>3</sub>O<sub>4</sub>@SiO<sub>2</sub>, by adding ethyl acetate. Utilizing this uniformly distributed single core Fe<sub>3</sub>O<sub>4</sub>@SiO<sub>2</sub>, we modified its surface with pH-sensitive nanovalve to investigate its uptake and release capacities.<sup>9-14</sup>

Different from MCM-41 mesoporous silica nanoparticles, the uptake and release

capacities of  $\text{Fe}_3\text{O}_4@\text{SiO}_2$  core/shell nanoparticle are lower because of radial porous structure instead of 2D hexagonal array, central space occupation by  $\text{Fe}_3\text{O}_4$  and the stabilizing agent oleic acid surrounding iron oxide. Therefore it is important to determine the optimal loading condition for  $\text{Fe}_3\text{O}_4@\text{SiO}_2$  modified with pH-sensitive nanovalve. In bio-application, the amount of silica nanoparticles that will be injected into mice is determined based on its uptake and release capacities. A higher value of release capacity indicates lower amount of silica nanoparticle, which is crucial to prevent *in vivo* toxicity caused by excess materials. Moreover, external heating may also affect the dissociation of cyclodextrin cap from organic moiety on the stalk. And it is possible to make use of superparamagnetic iron oxide core to facilitate controlled drug release in acidic environment by means of exposing to oscillating magnetic field.

### **5.3. Results and Discussion**

#### **5.3.1. Improvement of $\text{Fe}_3\text{O}_4@\text{SiO}_2$ Synthesis with Controlled Size Distribution**

After transferring oleic acid stabilized  $\text{Fe}_3\text{O}_4$  from chloroform to CTAB aqueous solution, we coated the  $\text{Fe}_3\text{O}_4$  core with mesoporous silica layer, following the same method as synthesizing MCM-41. As shown in Figure 5.1, the as-synthesized  $\text{Fe}_3\text{O}_4@\text{SiO}_2$  has a broad size distribution and some particles do not have  $\text{Fe}_3\text{O}_4$  core inside. The  $\text{Fe}_3\text{O}_4@\text{SiO}_2$  was synthesized using different amounts of NaOH solution (70  $\mu\text{L}$ , 60  $\mu\text{L}$ , 50  $\mu\text{L}$ , and 35  $\mu\text{L}$ ) to adjust the hydrolysis and condensation rate. It is shown that with lower amount of base in the reaction, we got single core  $\text{Fe}_3\text{O}_4@\text{SiO}_2$  with a little narrower size distribution; however, there are many small free mesoporous silica nanoparticles and crosslinks between each other.

With modified methods reported by Hyeon, we synthesized  $\text{Fe}_3\text{O}_4@\text{SiO}_2$  with much more uniform size distribution than with previous method, and the diameters ranges from 50 nm to 80 nm when using different concentrations of  $\text{Fe}_3\text{O}_4$  as shown in Figure 5.2. Moreover, this method can be applied for different size  $\text{Fe}_3\text{O}_4$  cores as shown in Figure 5.3. Core/shell particles with 10 nm and 20 nm  $\text{Fe}_3\text{O}_4$  core were both successfully synthesized. We were using 10 nm  $\text{Fe}_3\text{O}_4@\text{SiO}_2$  with a diameter of 50 nm as delivery model for further uptake and release capacity test.

We have the hypothesis that when ethyl acetate was mixed with the base solution, there are two factors changed in the reaction: First the pH and second the TEOS hydrolysis and condensation rate. Hydrolysis of ethyl acetate itself lowers the pH of the reaction mixture (pH = 12), which increases the condensation rate. Moreover, one of the ethyl acetate hydrolysis products is ethanol, which is also the product TEOS hydrolysis, thus moving the TEOS hydrolysis reaction equilibrium to the left, and slowing the hydrolysis rate. In a short period of time, fewer amounts of hydrolyzed TEOS will lead to less silica formed in the condensation reaction.

### **5.3.2. The Uptake and Release Capacity of $\text{Fe}_3\text{O}_4@\text{SiO}_2$ Core/Shell Nanoparticle**

The structure of pH-sensitive nanovalve and cargo molecule used in this model to measure uptake and release capacities are shown in Figure 5.4A. The N-phenylaminomethyltriethoxysilane (PHAMTES) stalk was attached on the outer surface of 10 nm  $\text{Fe}_3\text{O}_4@\text{SiO}_2$  with 50 nm diameter. The  $\alpha$ -CD interacts with the stalk through hydrophobic-hydrophobic interaction with a high non-covalent binding affinity at neutral or physiological pH. When the pH is lower than 3, the stalk is

protonated, leading to dissociation of  $\alpha$ -CD because of binding affinity decrease. As a result, the mesopores will be unblocked and cargo molecules diffuse out.<sup>9</sup> Figure 5.4B shows the release profile of Hoechst from  $\text{Fe}_3\text{O}_4@\text{SiO}_2$ . At pH 7, the pH-sensitive nanovale is very tight to cap the cargo molecule inside the pores, and there is no Hoechst leaking out as indicated by the flat baseline. When the pH is adjusted to 3, there is a dramatic increase of Hoechst concentration detected by the time-resolved fluorescence spectroscopy. After around five hours, the release profile reached a plateau, which means the release process finished and there is an equilibrium between the Hoechst concentrations inside and outside the pores. This figure shows that  $\text{Fe}_3\text{O}_4@\text{SiO}_2$  enabled with a pH-sensitive nanovale can deliver and release Hoechst as expected, and the radial mesopores can be tightly blocked by the nanovale.

In the loading and release process, uptake efficiency is defined as the percentage of Hoechst that is taken up by  $\text{Fe}_3\text{O}_4@\text{SiO}_2$  from the original loading solution. Uptake capacity is defined as the weight of total Hoechst taken up by  $\text{Fe}_3\text{O}_4@\text{SiO}_2$  divided by the weight of particle, and release capacity is defined as the weight of total released Hoechst from  $\text{Fe}_3\text{O}_4@\text{SiO}_2$  divided by the weight of particle.<sup>15</sup>

After  $\text{Fe}_3\text{O}_4@\text{SiO}_2$  was attached with pH-sensitive nanovale, equal amounts of the particles were loaded with various Hoechst concentrations in aqueous solutions, ranging from 1 mM to 30 mM. The  $\text{Fe}_3\text{O}_4@\text{SiO}_2$  particles were dispersed in the loading solution for 24 hours and then mixed with  $\alpha$ -CD to encircle the stalk and cap the mesopores for 12 hours. Finally the test samples were centrifuged down in a 2 ml

tube. The uptake efficiency was calculated from the Hoechst concentration difference in the supernatant before and after loading, and the uptake capacity was calculated with known particle weight after drying under vacuum. As shown in Figure 5.5A the uptake efficiency was more than 90 % when loading in 1 mM Hoechst, and decreased to around 20 % with 10 mM and 20 mM Hoechst, and finally down to around 13 % with 30 mM Hoechst loading. So when the loading concentration is very low at 1 mM, 90 % of the cargos diffuse into the pores, while this percentage decreases to 20 % when loading concentration increases 10 or 20 fold. The weight of Hoechst taken up by particles (inside the mesopores and absorbed on the outer surface) shown in Table 5.1 exhibits a clear uptake trend when increasing the loading concentration. For the same amount of particles (17 mg), the Hoechst weight loaded and absorbed increases from 0.57 mg to 2.49 mg. Comparing the experimental results of 20 mM and 30 mM Hoechst loading, we found that even though the uptake efficiency decreased from 20 % to 13 %, the actual amount of Hoechst taken up by particles were almost the same. This is reflected when comparing the uptake capacity shown in Figure 5.4. B. And this result implies that increase loading concentration helps increase uptake capacity, however, there is a saturation point due to the total surface area and total pore volume of  $\text{Fe}_3\text{O}_4@\text{SiO}_2$ . Further increase of the concentration above a certain value, e.g. 20 mM in our situation, won't lead to higher uptake, because the surface area of  $\text{Fe}_3\text{O}_4@\text{SiO}_2$  was completely occupied by Hoechst through both capping with  $\alpha$ -CD and absorbing by electrostatic interaction.

We also investigated the release capacity for these particles loaded with different

Hoechst concentrations. Before being dispersed in acidic aqueous solution for release study, the  $\text{Fe}_3\text{O}_4@\text{SiO}_2$  particles were washed extensively with deionized water to get rid of Hoechst absorbed on the outer surface of  $\text{Fe}_3\text{O}_4@\text{SiO}_2$ , as well as from any pores uncapped by the nanovalves. As shown in Table 1 and Figure 5.5. B., the release capacity surprisingly increased from 0.6 wt % to 1.09 wt % and finally decreased to 0.24 wt % when increasing loading concentrations. The explanation is that when the Hoechst loading solution concentration is higher than 10 mM, the organic moiety of unloaded Hoechst will compete with the PhAMTES stalk and bind to  $\alpha$ -CD, which leads to uncapping some of the mesopores and further leaking of Hoechst. This is especially obvious when loading concentration goes up to 40 mM with a lot of excess Hoechst in solution. When the concentration is low at 1 mM, most of cargo is loaded and capped inside the pores and the amount of surplus Hoechst is negligible compared with  $\alpha$ -CD. In terms of the release capacity value, it is lower than that of MCM-41 for two reasons. First, with radial mesopore structure  $\text{Fe}_3\text{O}_4@\text{SiO}_2$  has a surface area of  $530 \text{ m}^2/\text{g}$  and total pore volume of  $0.67 \text{ cc/g}$ , while MCM 41 has a surface area of  $1000 \text{ m}^2/\text{g}$  and total pore volume of  $0.8 \text{ cc/g}$ . Therefore  $\text{Fe}_3\text{O}_4@\text{SiO}_2$  has less inner surface absorption of hydrophilic dye through electrostatic interaction and packing in the pores. Second, there are oleic acid ligands as stabilizer around the  $\text{Fe}_3\text{O}_4$  core, and their hydrophobic hydrocarbon chain is toward the silica shell which may decrease the hydrophilic cargo loading. Overall among the four concentrations we applied for  $\text{Fe}_3\text{O}_4@\text{SiO}_2$  loading, 10 mM Hoechst aqueous solution gives the highest release capacity, while 20 mM results in highest

uptake capacity.

### **5.3.3. Influence of external heating / oscillating magnetic field on Hoechst release from $\text{Fe}_3\text{O}_4@\text{SiO}_2$**

It is known that temperature has impacts on molecule thermodynamic behaviors and the binding affinity between host and guest molecules. We increased the bulk solution temperature to investigate if increase of surrounding temperature will trigger dissociation of CD from the stalk and dye release. At the same time, the release due to external thermal heating was compared with the total amount of cargo released from pH change. As shown in Figure 5.6., we loaded particles with Hoechst and PI to test their release from  $\text{Fe}_3\text{O}_4@\text{SiO}_2$  enabled with pH-sensitive nanovalves. The solid particles were placed at the corner of a glass vial and the concentration of Hoechst/PI in the supernatant was detected by the time-resolved fluorescence spectroscopy. Figure 5.6. A. shows that in the first hour, there was no Hoechst dye releasing from the mesopores at pH 7. When the solution was heated up to 84 °C by external hotplate heating, there was a slight increase of Hoechst fluorescence detected in the supernatant. However, part of the increase was caused by the temperature sensitive emission of Hoechst molecule, which was reflected by the decrease of fluorescence intensity when external heating was turned off. After the particle solution cooled down to room temperature for around one hour, HCl solution was added to adjust the pH to 3 to release the rest of Hoechst from pores. Comparing the Hoechst release from pH change and external heating, we found that more than 90 % of Hoechst was released within 2 hours when lowering pH to 3, and less than 10 % Hoechst release

was caused by external heating. Therefore external heating helps release small amount of Hoechst, however, the total release amount is much less than that caused by pH change. And the release rate in acidic solution at room temperature is higher than that in heated solution.

Moreover, we loaded  $\text{Fe}_3\text{O}_4@\text{SiO}_2$  with PI, which is another widely used cargo molecule, considering its different size from Hoechst. As shown In Figure 5.6. B., there is no release in the first hour at pH 7 and room temperature. Heating up to 84 °C helped release less than 5 % of PI and most of PI got released after adjusting the pH to 3. Both release results from two cargos indicate that heating itself cannot supply sufficient energy for CD to dissociate from the stalk and trigger cargo release effectively. This may be caused by the relative stable binding affinity between the nanovalve stalk and cap within this temperature range (25 to 84 °C).

Superparamagnetic iron oxide can induce a huge temperature increase when exposed to oscillating magnetic field. After coated with mesoporous silica shell and placed in aqueous medium, the magnetic  $\text{Fe}_3\text{O}_4@\text{SiO}_2$  increases local and surrounding temperature to different extents depending on the oscillating magnetic field intensity and particle size. As shown in Figure 5.7., 13.5 mg 10 nm  $\text{Fe}_3\text{O}_4@\text{SiO}_2$  was placed in 1 mL of water in centrifuge tube and exposed to external oscillating magnetic field for 40 minutes. The supernatant temperature increases from room temperature 27 °C to a maximum of 38 °C within 25 minutes and is constant thereafter due to equilibrium between heat generation and dissipation. This experiment proves that the magnetic  $\text{Fe}_3\text{O}_4@\text{SiO}_2$  nanoparticles can generate heat



under oscillating magnetic field. Taking into account the heat dissipation of solution surround  $\text{Fe}_3\text{O}_4@\text{SiO}_2$ , the particle surface temperature increase should be higher than the bulk solution. We tested  $\text{Fe}_3\text{O}_4@\text{SiO}_2$  loaded with Hoechst or PI under the oscillating magnetic field to see if there is any thermally triggered release. As shown in Figure 5.8. The fluorescence intensity was detected over time and an oscillating magnetic pulse with duration of 2 minutes was applied 3 times for Hoechst loaded particles and 6 times for PI loaded particles. In terms of Hoechst, the oscillating magnetic field caused spikes in the signal, and there is no obvious release based on the fluorescence intensity profile. For PI, the gradually decrease of fluorescence intensity indicated no release and it was possibly affected by oscillating magnetic field. Comparing this experimental result with external heating, we think the particle local temperature is much lower than 84 °C, which does not supply enough energy to dissociate  $\alpha$ -CD from the stalk and release the cargo.

#### **5.4. Conclusions**

We successfully synthesized uniformly distributed and well dispersed  $\text{Fe}_3\text{O}_4@\text{SiO}_2$  by adding ethyl acetate into the reaction mixture and used this synthesis with 10nm and 20 nm  $\text{Fe}_3\text{O}_4$ , as well as various  $\text{Fe}_3\text{O}_4$  concentrations to obtain different sizes of core/shell nanoparticle. We chose the 10 nm  $\text{Fe}_3\text{O}_4$  with 50 nm silica shell diameter to test its uptake and release capacity with Hoechst as cargo molecule. The core/shell particles were modified with pH-sensitive nanovalves to trap Hoechst and the release was triggered at pH 3. The experimental results show that when the loading concentrations increase from 1 mM to 40 mM, the highest uptake capacity is

reached at 20 mM, while the highest release capacity is reached at 10 mM Hoechst loading. The pores are saturated with Hoechst when loading concentration is higher than 20 mM as calculated from the weight of Hoechst taken up by the particles. In other words, high uptake capacity does not necessarily mean high release capacity, because there may be a lot drug absorbed on the outer surface or loaded in the uncapped pores, and those cargo molecules will be removed in the sample washing process. Moreover, there is competitive binding between Hoechst and the stalk organic moiety to  $\alpha$ -CD. Therefore it is of importance to find an optimal loading concentration to reach highest release capacity.

External heating does help release a small amount of cargo, but not as much as the amount of cargo release triggered by pH change. This can be explained as the thermal energy (84 °C) is not enough for  $\alpha$ -CD to dissociate from the stalk. Both tests with  $\text{Fe}_3\text{O}_4@\text{SiO}_2$  loaded with Hoechst and PI proved this point. Moreover, exposing magnetic  $\text{Fe}_3\text{O}_4@\text{SiO}_2$  to an oscillating magnetic field does not supply enough thermal energy to disturb the non-covalent hydrophobic-hydrophobic interaction between  $\alpha$ -CD and phenyl amino stalk, which can be explained based on the external heating experiment as well as the temperature change around the core reported by our group before.

## **5.5. Experimental Section**

*Materials:* All chemicals are used as purchased: Cetyltrimethylammonium bromide (CTAB, 95%), tetraorthoethylsilicate (TEOS, 98%),  $\alpha$ -cyclodextrin ( $\geq 98\%$ ), Hoechst 33342 ( $\geq 97\%$ ), propidium iodide (PI) ( $\geq 95\%$ ), toluene (99.8%), and  $\text{Fe}_3\text{O}_4$  (10 nm,

5 mg/mL in toluene) were purchased from Sigma (St. Louis, MO). N-phenylaminomethyltriethoxysilane (PhAMTES) was purchased from Gelest (Morrisville, PA). Chloroform (99%) was purchased from EMD Millipore (Billerica, MA).

*Traditional Synthesis of Fe<sub>3</sub>O<sub>4</sub>@SiO<sub>2</sub>:* The typical synthesis method of Fe<sub>3</sub>O<sub>4</sub>@SiO<sub>2</sub> core/shell silica nanoparticles is based on the synthesis of MCM 41 procedure and scaled down from 120 mL to 10 mL H<sub>2</sub>O. An alkaline aqueous solution (9 mL H<sub>2</sub>O, 70 μL 2.0 M NaOH) was heated to 80 °C and kept steady while stirring rapidly. Cetyltrimethylammonium bromide (20 mg) was dissolved in 1 mL water. 100 μL of iron oxide in toluene solution (5 mg/mL) was transferred to a 10 mL flask and blown dry by air. After that 1 mL of chloroform was added to disperse the iron oxide again to get a dark solution and this was mixed with the 1 mL aqueous CTAB solution prepared before. Chloroform was boiled off the solution upon heating, and the oil-in-water microemulsion finally became clear brown. This mixture was sonicated for a few minutes to make sure there was no aggregation of iron oxide nanoparticles. The iron oxide mixture was added to the base solution, and after around ten minutes the temperature was steady at 80 °C. Finally, tetraethyorthosilicate (TEOS, 100 μL) was added into the solution stirring for 2 hours at 80 °C. When the reaction finished, Fe<sub>3</sub>O<sub>4</sub>@SiO<sub>2</sub> was washed with methanol or ethanol twice or three times. The centrifuged iron oxide core/shell silica nanoparticles are dark brown.

*Modified Synthesis of Fe<sub>3</sub>O<sub>4</sub>@SiO<sub>2</sub>:* The synthesis procedure is very similar to the traditional method, except for that reaction was undertaken at 70 °C for 3 hours and

ethyl acetate was added right after TEOS. A solution of 9 mL water, 60  $\mu$ L 2.0 M NaOH was heated to 70  $^{\circ}$ C and kept steady while stirring rapidly. Cetyltrimethylammonium bromide (CTAB, 20 mg) was dissolved in 1 mL water. 90 - 170  $\mu$ L of iron oxide in toluene solution (5 mg/mL) was transferred to a 10 mL flask and blown dry by air. After that 1 mL of chloroform was added to disperse the iron oxide and this was mixed with the 1 mL aqueous CTAB solution prepared before. Chloroform was boiled off the solution upon heating, and the oil-in-water microemulsion finally became clear brown. This mixture was sonicated for a few minutes to make sure there is no aggregation of iron oxide nanoparticles. The resulting solution was added to the base solution and the temperature was steady at 70  $^{\circ}$ C after 10 mins. Then, 100  $\mu$ L tetraethyorthosilicate (TEOS, Aldrich, 98%) and 0.6 mL ethyl acetate were added in sequence into the solution and the mixture was stirred vigorously for 3 hours at 70  $^{\circ}$ C. When the reaction finished, the silica nanoparticles were washed and centrifuged with methanol or ethanol twice or three times. Iron oxide mesoporous silica nanoparticles synthesized with this method is uniformly monodispersed and there is little necking among the nanoparticles. As-synthesized  $\text{Fe}_3\text{O}_4@\text{SiO}_2$  (20 mg) was dispersed in 8 mL methanol, mixed with 5.4 mg ammonium nitrate and refluxed under  $\text{N}_2$  for 30 minutes. The  $\text{Fe}_3\text{O}_4@\text{SiO}_2$  without surfactant template was collected by centrifugation and washed with methanol for twice.

*Attachment of pH-sensitive Nanovalve on  $\text{Fe}_3\text{O}_4@\text{SiO}_2$  and cargo loading:* 100 mg as-synthesized  $\text{Fe}_3\text{O}_4@\text{SiO}_2$  anhydrous toluene 4 times and dispersed in toluene (10

mL), mixed with PhAMTES (30  $\mu$ L) and refluxed under  $N_2$  for 24 hours. The anilinoalkane modified  $Fe_3O_4@SiO_2$  was collected by centrifugation and washed with toluene, methanol and deionized water. Particles were then soaked in 1 mL Hoechst (1 mM, 10 mM, 20 mM and 30 mM) for 24 hours, followed by adding  $\alpha$ -CD (200 mg, 0.1 mmol) and rotated for another 3 days at room temperature. The Hoechst loaded  $Fe_3O_4@SiO_2$  with pH-sensitive nanovalve was washed with water to get rid of dye absorbed on the outer surface or not capped. The resulting product was dried under vacuum for 12 hours and weighed by analytical scale.

*Uptake and Release Capacity Measurement:* UV-Vis spectra were collected on a Cary 500 UV-Vis-NIP spectrophotometer. UV-Vis spectra work function was calibrated with Hoechst standard solution (0.01 mM, 0.02 mM, 0.025 mM). Uptake capacity (wt %) =  $[(W_{\text{Hoechst before loading}} - W_{\text{Hoechst after loading}}) / W_{\text{particle}}] \times 100$  %. In term of release capacity, loaded particle  $Fe_3O_4@SiO_2$  was dispersed in pH 3 HCl solution for 24 hours and then centrifuged down to measure the concentration of MXF released into the supernate. Release capacity (wt %) =  $(W_{\text{released Hoechst}} / W_{\text{particle}}) \times 100$  %.

*Stimulated Release Studies:* To measure Hoechst release from  $Fe_3O_4@SiO_2$  and detect Hoechst fluorescence emission in supernates, weighed and dried  $Fe_3O_4@SiO_2$  powder was put at the corner of a glass vial containing 10 ml DI water. A probe laser beam (5 mW 377 nm) was passed through the supernatant in the glass vial such that released Hoechst was excited and emitted fluorescence was detected and collected by a charge-coupled device (CCD) detector and a computer in 1 s intervals over the course of the experiment. Baseline spectra were collected to confirm that there was no

Hoechst leakage, and then 1M HCl solution was added to adjust the pH to 3. The release profile was constructed by integration of maximum emission peak area from 480 nm to 520 nm as a function of time. For external heating experiment, a hotplate was utilized to heat up the bulk solution and the temperature was calibrated before the release experiment.

*Temperature change induced by magnetic  $Fe_3O_4@SiO_2$ :*  $Fe_3O_4@SiO_2$  (13.5 mg) was placed at the bottom of a centrifuge tube with 1mL deionized water and placed in the center of a water-cooled copper coil. The copper coil can generate an oscillating magnetic field with highest frequency of 500 kHz and maximum amplitude of 37.4 kAm<sup>-1</sup>. The machine was turned on for 40 minutes continuously and supernatant temperature was detected at 1<sup>st</sup> minute, 2<sup>nd</sup> minute, 5<sup>th</sup> minute, 10<sup>th</sup> minute etc. with a 5 minutes interval.

*Oscillating magnetic field stimulated release:* The glass vial contain water and magnetic  $Fe_3O_4@SiO_2$  was placed inside a water-cooled copper coil. Oscillating magnetic pulses were produced by manually turning on and off the machine with duration of 2 minutes. The position of glass vial was adjusted so that the probe laser beam can penetrate through the supernatant without being blocked by the copper coil.

*Physiochemical Characterization of  $Fe_3O_4@SiO_2$ :* Transmission electron microscopy (TEM) images of  $Fe_3O_4@SiO_2$  were obtained using a JEM1200-EX (JEOL) instrument (JEOL USA, Inc., Peabody, MA). UV-Vis spectra were collected with Cary 5000 UV-vis-NIP spectrophotometer.

## 5.6. Figures and Tables

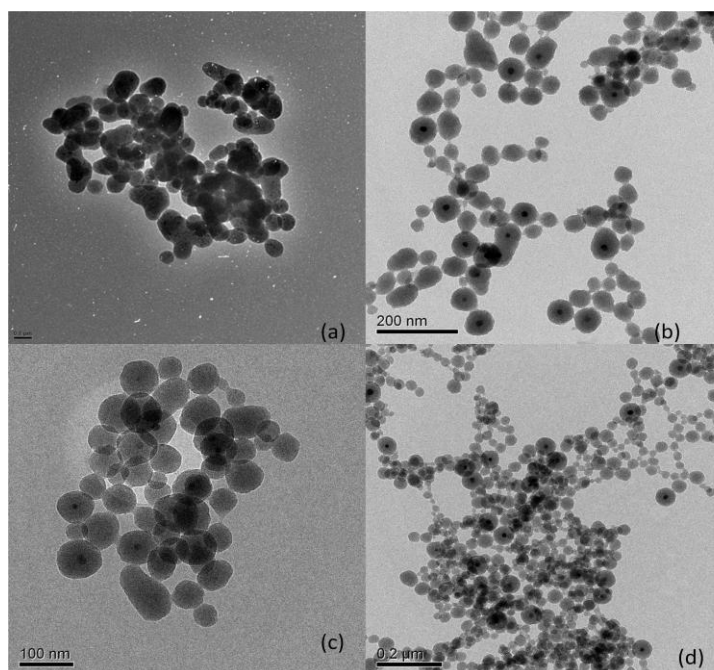


Figure 5.1. TEM of  $\text{Fe}_3\text{O}_4@\text{SiO}_2$  synthesized without ethyl acetate using different amount of 2M NaOH (a). 70  $\mu\text{L}$ , (b). 60  $\mu\text{L}$ , (c). 50  $\mu\text{L}$ , (d). 35  $\mu\text{L}$ .

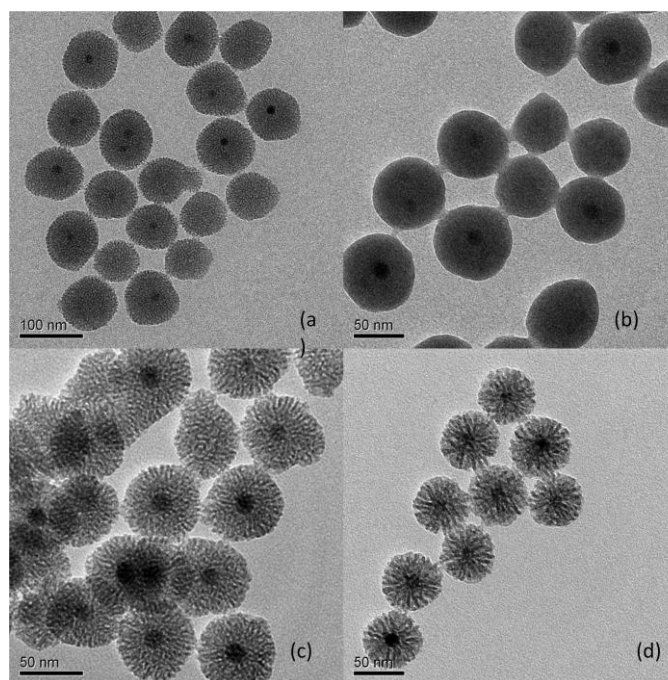


Figure 5.2. TEM of different size  $\text{Fe}_3\text{O}_4@\text{SiO}_2$  synthesized with ethyl acetate and

different amount of  $\text{Fe}_3\text{O}_4$ / Toluene (5 mg/mL) (a). 80 nm  $\text{Fe}_3\text{O}_4@ \text{SiO}_2$ , 90  $\mu\text{L}$ , (b). 70 nm  $\text{Fe}_3\text{O}_4@ \text{SiO}_2$ , 130  $\mu\text{L}$ , (c). 60 nm  $\text{Fe}_3\text{O}_4@ \text{SiO}_2$ , 150  $\mu\text{L}$  (d). 50 nm  $\text{Fe}_3\text{O}_4@ \text{SiO}_2$ , 170  $\mu\text{L}$

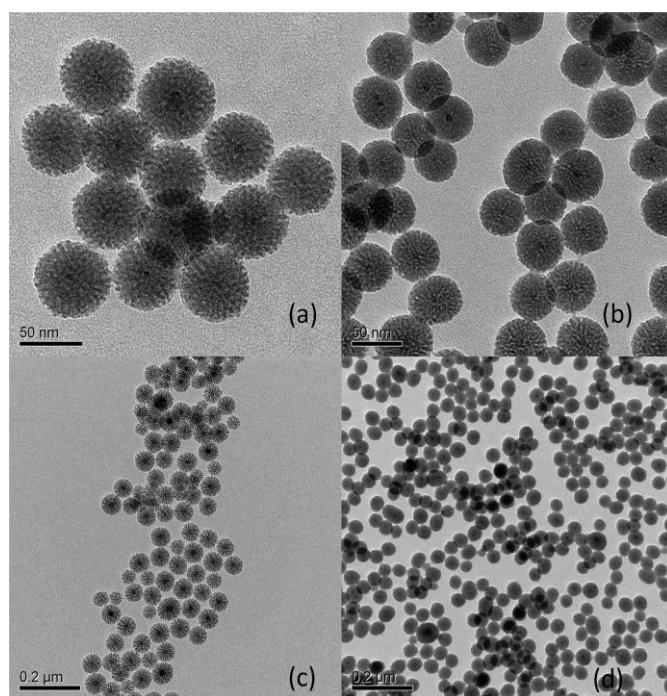


Figure 5.3. TEM of as-synthesized  $\text{Fe}_3\text{O}_4@ \text{SiO}_2$  showing uniform size distribution and radial mesoporous structure with (a, b, c). 10 nm core and (d). 20 nm core



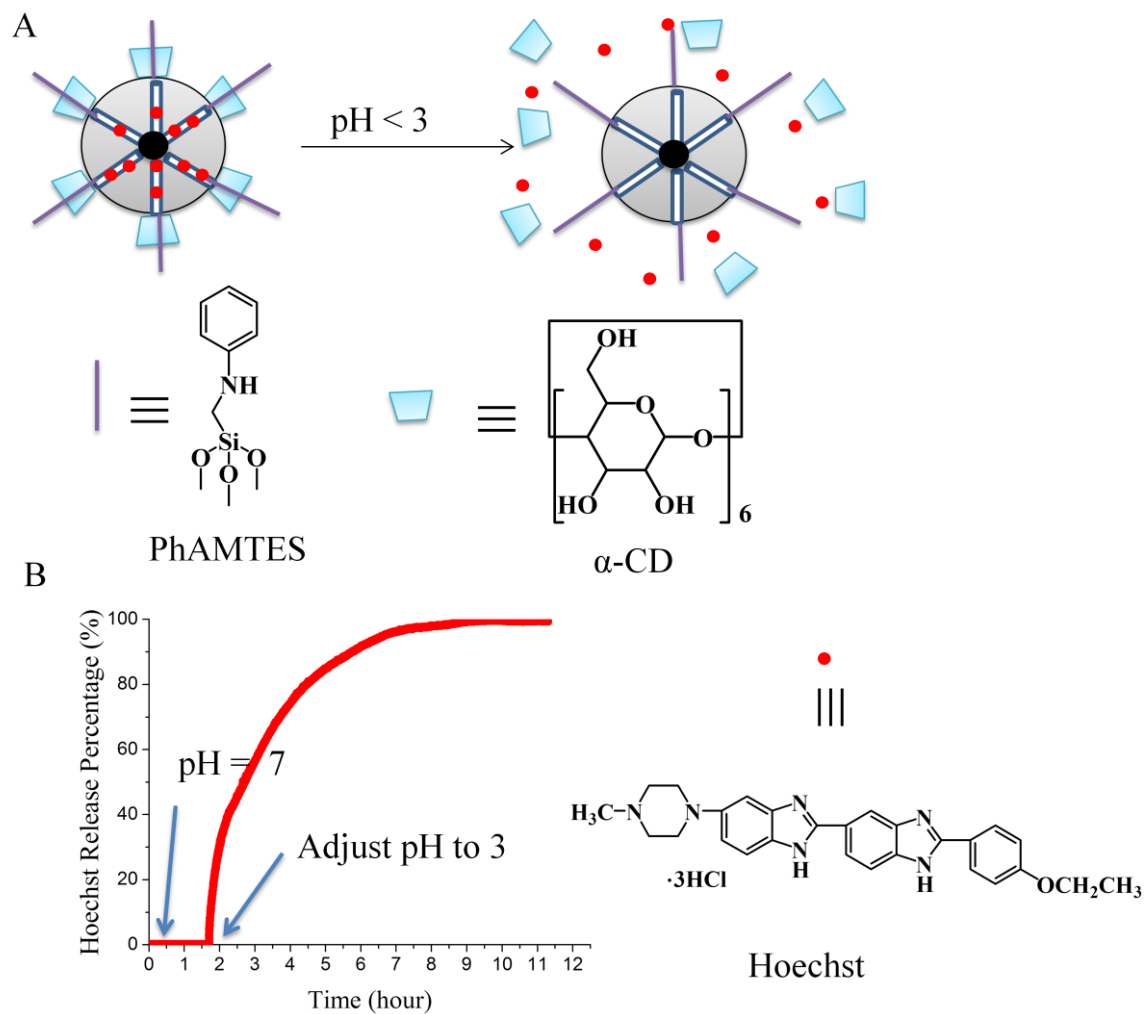


Figure 5.4. A. Structure of mechanized  $\text{Fe}_3\text{O}_4@\text{SiO}_2$  modified with pH-sensitive nanovalve and its working mechanism. The stalk is composed of aniline alkane and the cap is  $\alpha$ -CD. When the pH is lower than 3, the stalk is protonated and the cap dissociates from it. The cargo molecule is Hoechst 33342. B. Release profile of mechanized  $\text{Fe}_3\text{O}_4@\text{SiO}_2$  loaded with Hoechst cargo. The baseline is flat at pH 7, indicating there is no leakage and when decrease pH to 3 there is a dramatic increase of Hoechst fluorescence intensity which is caused by the release of cargo molecule into supernatant solution.

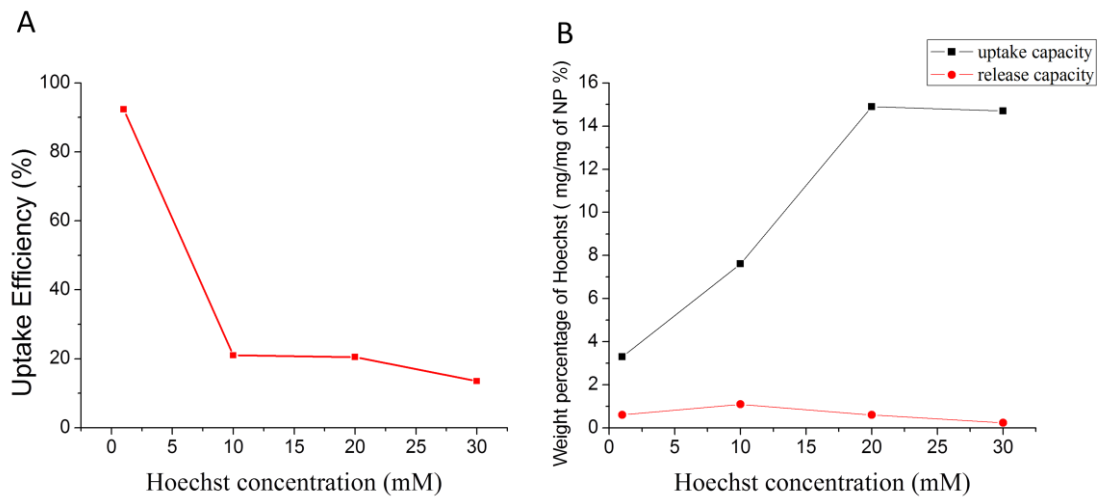


Figure 5.5. A.  $\text{Fe}_3\text{O}_4@\text{SiO}_2$  with pH-sensitive nanove uptake efficiency decreases when increasing the Hoechst loading concentration from 1 mM to 30 mM. B.  $\text{Fe}_3\text{O}_4@\text{SiO}_2$  uptake capacity increases when Hoechst concentration increases from 1 to 20 mM and keeps almost the same at 20 mM and 30 mM Hoechst loading. The release capacity increases at first and reaches highest point at 10 mM Hoechst, and then goes down to the lowest value with 30 mM Hoechst loading.

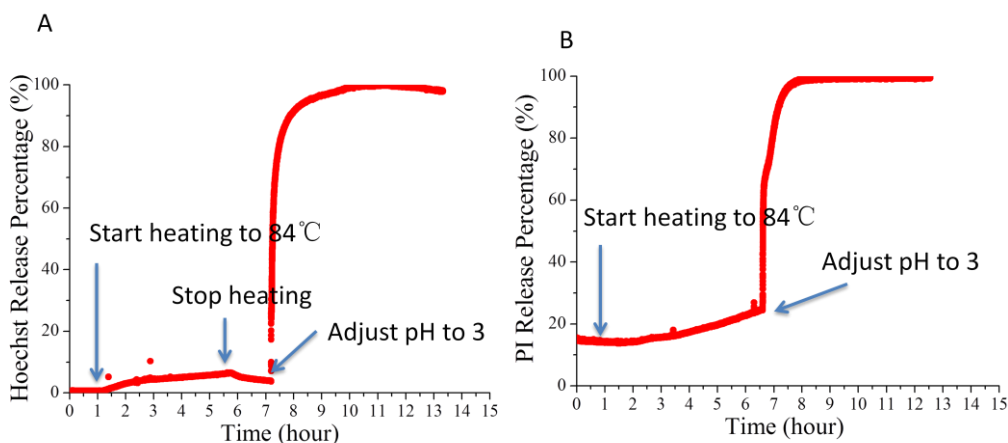


Figure 5.6. A.  $\text{Fe}_3\text{O}_4@\text{SiO}_2$  attached with pH-sensitive nanovlave loaded with

Hoechst was immersed in pH 7 water, and after one hour hotplate was applied to heat up to the bulk solution to 84 °C for 5.5 hours. After stopping external heating to allow the sample solution to cool down to room temperature, HCl was added in to adjust pH to 3. Obviously there was a dramatic increase of released Hoechst in the supernatant. The release profile shows that external heating did not help much Hoechst diffuse out of the pore as we expected and the amount of Hoechst released out is negligible compared adding HCl. Moreover, the Hoechst fluorescence is sensitive to temperature and the release percentage decreased a little when lowering temperature. Detection stopped after 13 hours when the profile reached a plateau. B.  $\text{Fe}_3\text{O}_4@\text{SiO}_2$  attached with pH-sensitive nanovlave and loaded with Propidium Iodide (PI) was immersed in pH 7 water at first. One hour later the solution was heated up to 84 °C for around 6 hours, followed by adding HCl to lower the pH to 3. External heating has no significant effect on PI release compared with lowering pH triggered release.

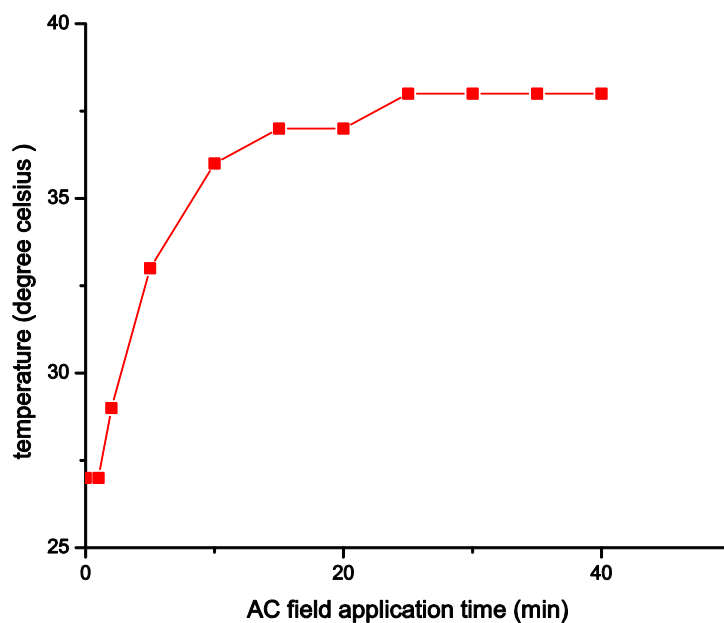


Figure 5.7. Supernatant temperature increase with  $\text{Fe}_3\text{O}_4@\text{SiO}_2$  placed at the bottom of the tube under oscillating magnetic field

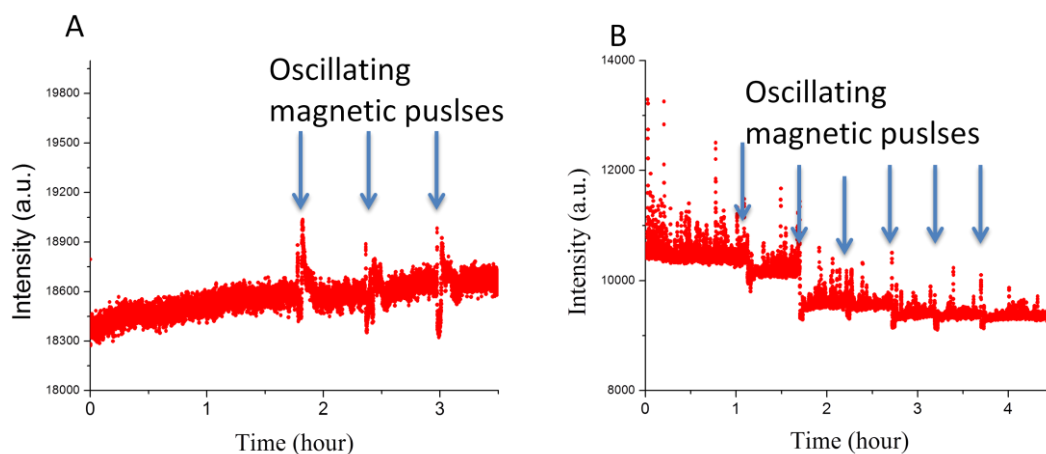


Figure 5.8. A.  $\text{Fe}_3\text{O}_4@\text{SiO}_2$  attached with pH-sensitive nanovlave loaded with Hoechst. Particles were placed in pH 7 water and baseline was collected for 110 minutes. Three oscillating magnetic pulses were applied at an interval of 30 minutes, and each pulse last for 2 minutes. No obvious release was observed. B.  $\text{Fe}_3\text{O}_4@\text{SiO}_2$  attached with pH-sensitive nanovlave loaded with Propidium Iodide.

Particles were placed in pH 7 water and baseline was collected for 75 minutes.. Seven oscillating magnetic pulses of were applied at an interval of 30 minis, and each pulse last for 2 minutes. There is still no obvious release with PI.

Table 5.1. Uptake Efficiency, Weight of Uptake Hoechst, Uptake Capacity and Release Capacity of Fe<sub>3</sub>O<sub>4</sub>@SiO<sub>2</sub> when loaded with 1, 10 , 20 , 30 mM Hoechst aqueous solution

Hoechst Concentration (mM)	Uptake Efficiency (%)	Weight of Hoechst Loaded & Absorbed (mg)	Uptake capacity (wt %)	Release Capacity (wt %)
1	92.3	0.57	3.3 %	0.60 %
10	21.0	1.29	7.61 %	1.09 %
20	20.5	2.52	14.9 %	0.60 %
30	13.5	2.49	15.7 %	0.24 %

## 5.7. References

1. Ho, D.; Sun, X. L.; Sun, S. H. Monodisperse Magnetic Nanoparticles for Theranostic Applications. *Accounts Chem Res* 2011, 44, 875-882.
2. Kim, J.; Kim, H. S.; Lee, N.; Kim, T.; Kim, H.; Yu, T.; Song, I. C.; Moon, W. K.; Hyeon, T. Multifunctional Uniform Nanoparticles Composed of a Magnetite Nanocrystal Core and a Mesoporous Silica Shell for Magnetic Resonance and Fluorescence Imaging and for Drug Delivery. *Angew Chem Int Edit* 2008, 47, 8438-8441.
3. Hergt, R.; Dutz, S.; Muller, R.; Zeisberger, M. Magnetic particle hyperthermia: nanoparticle magnetism and materials development for cancer therapy. *J Phys-Condens Mat* 2006, 18, S2919-S2934.
4. Baeza, A.; Guisasola, E.; Ruiz-Hernandez, E.; Vallet-Regi, M. Magnetically Triggered Multidrug Release by Hybrid Mesoporous Silica Nanoparticles. *Chem Mater* 2012, 24, 517-524.
5. Ye, F.; Laurent, S.; Fornara, A.; Astolfi, L.; Qin, J.; Roch, A.; Martini, A.; Toprak, M. S.; Muller, R. N.; Muhammed, M. Uniform mesoporous silica coated iron oxide nanoparticles as a highly efficient, nontoxic MRI T2 contrast agent with tunable proton relaxivities. *Contrast Media Mol I* 2012, 7, 460-468.
6. Yang, P. P.; Quan, Z. W.; Hou, Z. Y.; Li, C. X.; Kang, X. J.; Cheng, Z. Y.; Lin, J. A magnetic, luminescent and mesoporous core-shell structured composite material as drug carrier. *Biomaterials* 2009, 30, 4786-4795.
7. Jiang, F. Y.; Fu, Y.; Zhu, Y.; Tang, Z. K.; Sheng, P. Fabrication of iron oxide/silica

core-shell nanoparticles and their magnetic characteristics. *J Alloy Compd* 2012, 543, 43-48.

8. Lu, C. W.; Hung, Y.; Hsiao, J. K.; Yao, M.; Chung, T. H.; Lin, Y. S.; Wu, S. H.; Hsu, S. C.; Liu, H. M.; Mou, C. Y.; Yang, C. S.; Huang, D. M.; Chen, Y. C. Bifunctional magnetic silica nanoparticles for highly efficient human stem cell labeling. *Nano Lett* 2007, 7, 149-154.

9. Du, L.; Liao, S. J.; Khatib, H. A.; Stoddart, J. F.; Zink, J. I. Controlled-Access Hollow Mechanized Silica Nanocontainers. *J Am Chem Soc* 2009, 131, 15136-15142.

10. Meng, H. A.; Xue, M.; Xia, T. A.; Zhao, Y. L.; Tamanoi, F.; Stoddart, J. F.; Zink, J. I.; Nel, A. E. Autonomous in Vitro Anticancer Drug Release from Mesoporous Silica Nanoparticles by pH-Sensitive Nanovalves. *J Am Chem Soc* 2010, 132, 12690-12697.

11. Hu, S. H.; Chen, S. Y.; Liu, D. M.; Hsiao, C. S. Core/single-crystal-shell nanospheres for controlled drug release via a magnetically triggered rupturing mechanism. *Adv Mater* 2008, 20, 2690-+.

12. Zhang, M. Q.; Kievit, F. M. Surface engineering of iron oxide nanoparticles for targeted cancer therapy. *Abstr Pap Am Chem S* 2012, 243.

13. Zhu, X. Y.; Gu, J. L.; Li, Y. S.; Zhao, W. R.; Shi, J. L. Magnetic core-mesoporous shell nanocarriers with drug anchorages suspended in mesopore interior for cisplatin delivery. *Micropor Mesopor Mat* 2014, 196, 115-121.

14. Zhang, L. Y.; Wang, T. T.; Li, L.; Wang, C. G.; Su, Z. M.; Li, J. Multifunctional fluorescent-magnetic polyethyleneimine functionalized Fe<sub>3</sub>O<sub>4</sub>-mesoporous silica yolk-shell nanocapsules for siRNA delivery. *Chem Commun* 2012, 48, 8706-8708.

15. Li, Z. X.; Nyalosaso, J. L.; Hwang, A. A.; Ferris, D. P.; Yang, S.; Derrien, G.; Charnay, C.; Durand, J. O.; Zink, J. I. Measurement of Uptake and Release Capacities of Mesoporous Silica Nanoparticles Enabled by Nanovalve Gates. *J Phys Chem C* 2011, 115, 19496-19506.



## Chapter 6

### Application of $\text{Fe}_3\text{O}_4@\text{SiO}_2$ Mesoporous Silica Nanoparticles in Drug Delivery to Biofilms

#### 6.1. Abstract

A biofilm is bacterial community that formed on a biological surface, for example the interface between artificial implants and human tissues. It may cause serious infections which cost lots of extra medical sources, treatment and money. It is always a challenge to deliver antibiotics to those specific sites and kill the bacteria. Herein we developed magnetic  $\text{Fe}_3\text{O}_4@\text{SiO}_2$  particles, which consist of a super paramagnetic iron oxide core and a shell of mesoporous silica, as well as nanovalve to trap and release on-demand different cargos including dyes and antibiotics. We investigated the

distribution and targeting of this system into biofilms and find the particles can effectively penetrate into the biofilm and stay stable with the magnetic forces from rare earth magnet. Moreover, negatively charged particles preferentially absorb in the biofilm in comparison to positively charged particles due to electrostatic interaction. A permalloy micro-pillar substrate amplifying the magnetic forces results in an increase amount of particles embedded in the biofilm when magnetized by the rare earth magnet. We also loaded  $\text{Fe}_3\text{O}_4@\text{SiO}_2$  with Hoechst, and it exhibited tremendous release when adding onto the biofilm. The pH-sensitive release of Hoechst implies the potential application of  $\text{Fe}_3\text{O}_4@\text{SiO}_2$  system to deliver antibiotics and kill bacteria throughout the biofilm.

## **6.2. Introduction**

Biofilms are microbial films formed and attached on the surface of biological or synthetic implants. It is caused by microbial growth and may lead to serious device-induced infections inside the human body. The formation of biofilm was discovered in early 1970's, and it is still a challenge nowadays to eradicate biofilms in medical surgeries.<sup>1</sup> The biofilm we are treating has been found formed at the surface of catheters, one of the most well-known examples of devices-induced biofilms. The catheter associated infections cost extra money and medical sources every year.<sup>2</sup>

Biofilms significantly reduce the bacteria's susceptibility to antibiotics and cannot be eradicated by traditional antibiotic therapy for several reasons. The biofilm itself synthesizes extracellular polymeric substances (EPS), which consist of proteins, nucleic acids, polysaccharides, and lipids as a barrier layer. It is very difficult for free

antibiotics to diffuse through this barrier. Moreover, there are other interactions between the enzymes of outer layers of biofilm and antibiotics that inactivate the free drug or alter its target sites.<sup>1, 3</sup> Researchers have developed various methods to prevent biofilm formation such as synthetic device surface modification, as well as other drug controlled release systems, including liposomes, polymers, microemulsions, and metal nanoparticles.<sup>4-7</sup>

Herein we developed the controlled drug delivery system based on  $\text{Fe}_3\text{O}_4@\text{SiO}_2$  mesoporous silica nanoparticles modified with pH-sensitive nanovalves.<sup>8</sup> Compared with liposome or polymer systems, the  $\text{Fe}_3\text{O}_4@\text{SiO}_2$  with nanovalves can trap the cargo much tighter to prevent premature release and inactivation due to biofilm enzymes. Moreover, with magnetic core  $\text{Fe}_3\text{O}_4$ , the particles can be transported and positioned by a rare earth magnet for targeting.<sup>9</sup> Silica nanoparticles have higher mechanical strength than liposomes or polymers, which makes it easier for them to penetrate through the biofilm to eradicate bacteria and mechanically disrupt the biofilm. Furthermore,  $\text{Fe}_3\text{O}_4@\text{SiO}_2$  has relatively high release capacities for delivering antibiotics and metal ions as reported by our group.<sup>10</sup>

## **6.3. Results and Discussion**

### **6.3.1 Distribution of $\text{Fe}_3\text{O}_4@\text{SiO}_2$ in Biofilms with rare earth magnet**

In order to deliver and release antibiotics to the target site, the particle needs to be able to adhere to and penetrate the biofilms. We investigated the distribution of  $\text{Fe}_3\text{O}_4@\text{SiO}_2$  on biofilms with or without rare earth magnet. As shown in Figure 6.1, a biofilm was grown on a glass slide and red fluorescein labeled  $\text{Fe}_3\text{O}_4@\text{SiO}_2$  was

dispersed on top of the biofilm.  $\text{Fe}_3\text{O}_4@\text{SiO}_2$  has the advantage of being attracted by a magnet and penetrates biofilm EPS layers. In order to determine the influence of magnet, biofilm slides were divided into two groups. In one group, a rare earth magnet was placed underneath the glass slide for 1 minute, followed by removing and adding buffer to wash the biofilm. In the other group, after adding the particles on biofilm, we directly washed the surface without the magnet underneath. The particles, biofilm, and nuclei were labeled with red, green and blue fluorescent dyes respectively, and observed using a fluorescence microscope. The results show that the red fluorescence intensity from particles in the biofilm with the rare earth magnet underneath is much stronger than the group without magnetic attraction. It indicates that most of the  $\text{Fe}_3\text{O}_4@\text{SiO}_2$  particles stay on the surface of the biofilm and are easily washed away by the washing supernatant. When the  $\text{Fe}_3\text{O}_4@\text{SiO}_2$  was attracted by the magnet, they can be forced to enter the biofilm and remain stable after washing several times with buffer. Moreover, the empty space within the EPS network is completely filled with the magnetic particles as shown in the merged figure, thus supplying the platform to release drugs within the biofilm and reach a much higher local concentration than free drug. Therefore external magnetic field attraction significantly helps target the magnetic  $\text{Fe}_3\text{O}_4@\text{SiO}_2$  particles into the pathological site, and this is of great importance in preventing the particles from being removed by circulating fluids in human body.

It is also found that the interaction between magnetic  $\text{Fe}_3\text{O}_4@\text{SiO}_2$  and the rare earth magnet varies with different positions. As shown in Figure 6.2, on one glass

slide, the difference between red fluorescence intensities from particles at the edge and center of rare earth magnet were observed. More particles are attracted and remained in the biofilm at the edge of rare earth magnet than the center. And in terms of the particle distribution at the edge of the magnet, there is an obvious difference of the total amount of particles left in the biofilm with and without rare earth magnet. However, this does not happen to particles at the center of the magnet. The magnetic field at the center is very weak, and this can be explained as the magnetic field at the edge of rare earth magnet has highest magnetic intensity perpendicular to the glass slide to attract magnetic particles, while the magnetic field vector at the center is parallel to the biofilm and has smallest intensity perpendicular to the biofilm to pull down the particles.

### **6.3.2. Distribution of Modified $\text{Fe}_3\text{O}_4@\text{SiO}_2$ in Biofilms**

In order to determine the influence of particle surface modification on its distribution in biofilms, we modified particles with phosphonate groups or amine groups to make it negatively charged or positively charged. Moreover, another group of particles were derivatized with pH-sensitive nanovalve to determine if the organic moiety of stalk has any influence on their interactions with biofilms. Figure 6.3A shows the structure of nanovalve on  $\text{Fe}_3\text{O}_4@\text{SiO}_2$ . The nanovalve consists of a 1-methyl-1-H-benzimidazole (MBI) stalk and  $\beta$ -CD as the cap to trap the cargo. This nanovalve was designed to open and release the cargo when pH is lower than 6. The cargo molecule used here was Hoechst dye, which stains the DNA of cells in the biofilm and emits blue fluorescence under the fluorescence microscope. The

environmental pH of the biofilm varies in different areas and the local pH of some areas are lower than 6,<sup>11</sup> thus opening the nanovalve of the particle and releasing the Hoechst dye. Figure 6.3B and C show that the morphology and size of Fe<sub>3</sub>O<sub>4</sub>@SiO<sub>2</sub> are not affected after attached with the pH-sensitive nanovalve, and the particles preserve their uniform size distribution and dispersion after the whole modification procedures.

Fe<sub>3</sub>O<sub>4</sub>@SiO<sub>2</sub> with different surface modifications were added on top of the biofilm and washed as aforementioned. As shown in Figure 6.4A, compared with the other two groups of particle, there is a much larger number of negatively charged Fe<sub>3</sub>O<sub>4</sub>@SiO<sub>2</sub> absorbed in the biofilm due to electrostatic interaction. The red fluorescence intensity is proportional to the particle concentration. The number of Fe<sub>3</sub>O<sub>4</sub>@SiO<sub>2</sub> attached with pH-sensitive nanovalve in biofilm is lower than negatively charged ones and higher than positively charged particles, because the silica surface was slightly negatively charged. Few of the positively charged Fe<sub>3</sub>O<sub>4</sub>@SiO<sub>2</sub> particles remained in the biofilm even when the concentration was increased to 10<sup>7</sup>/mL. The cationic or anionic property of biofilms is dependent on the type of bacteria and their hydrophobicity/hydrophilicity. In our experiment, the bacterium grown is staphylococcus aureus, which is gram-positve bacteria and its EPS is primarily cationic. Therefore the particles can be modified with positive or negative charge depending on the primary bacteria to obtain maximum uptake by the biofilm.<sup>5</sup> In Figure 6.4B the Fe<sub>3</sub>O<sub>4</sub>@SiO<sub>2</sub> enabled with pH-sensitive nanovalve exhibit on-command release of Hoechst into the biofilm, and the release amount is

proportional to the number of particles remained in the biofilm, indicated by the blue fluorescence in the figures. When the concentration of  $\text{Fe}_3\text{O}_4@\text{SiO}_2$  is  $10^5/\text{mL}$  or  $10^6/\text{mL}$ , the released Hoechst is too little to be detected, and further increase of  $\text{Fe}_3\text{O}_4@\text{SiO}_2$  concentration to  $10^7/\text{mL}$  and  $10^8/\text{mL}$  leads to significant increase of detectable Hoechst fluorescence. These results indicate that the biofilm has a positive net charge, so that it has strong electrostatic attraction to negatively charged particles. Moreover, the biofilm environmental pH is low enough to open the pH-sensitive nanovalve and release the cargo. It also implies the potential usage of this system to delivery antibiotics into the biofilm.

### **6.3.3. Distribution of Modified $\text{Fe}_3\text{O}_4@\text{SiO}_2$ in Biofilms on two different substrates**

A permalloy micro-pillar substrate was fabricated, which consists of 80 % nickel and 20 % Iron. With this magnetic substrate, the magnetic force can be amplified between the  $\text{Fe}_3\text{O}_4@\text{SiO}_2$  and rare earth magnet, which will facilitate the penetration of particles into the biofilm. Figure 6.5A shows the surface structure of the permalloy micro-pillar substrate (magnetic ratcheting array) and bare polystyrene chip in bright-field view. The substrate was immersed in the bacterial medium and inoculated with staphylococcus aureus bacteria, and the biofilm formed on the substrate randomly without pattern. As shown in Figure 6.5B first row, it is found that most of the particles distribute along the permalloy micro-pillar pattern after placing the rare earth magnet beneath the substrate. Moreover, the  $\text{Fe}_3\text{O}_4@\text{SiO}_2$  changed the pattern of biofilm by mechanical disruption indicated by the green fluorescence, which was due

to amplified magnetic force from the permally micro-pillar substrate and the rare earth magnet. In comparison, there is no such change when particles were added to the biofilm inoculated on the polystyrene chip, although both of the samples have rare earth magnet underneath the substrates. Figure 6.5C shows the X and Y cross section of  $\text{Fe}_3\text{O}_4@\text{SiO}_2$  distribution and biofilm itself. In terms of the magnetic ratcheting array, which is the permalloy substrate, both particles and biofilm were rearranged into array patterns as indicated by the cross section fluorescence. The distribution of particles and biofilm on polystyrene substrate is random without specific patterns. Moreover, the X and Y cross section taken using confocal microscope prove that the magnetic particles can penetrate into the biofilm all the way to the bottom of the film, and this in-depth distribution is facilitated with the magnetic ratcheting array.

#### **6.4. Conclusions**

We investigated the distribution of various modified  $\text{Fe}_3\text{O}_4@\text{SiO}_2$  nanoparticles in biofilms grown on different substrates. First, we prove that magnetic force from a rare earth magnet is strong enough to pull the particles into the biofilm that they stay in the biofilm after washing several times. Second, it is shown that negatively charged  $\text{Fe}_3\text{O}_4@\text{SiO}_2$  particles have stronger electrostatic interaction with the biofilm network than positive ones, which ensures that most of the particles penetrate and stay in the biofilm after washing, even without using the rare earth magnet underneath. In terms of  $\text{Fe}_3\text{O}_4@\text{SiO}_2$  derivatized with pH-sensitive nanovalves, a moderate number of particles stay in the biofilm due to the slightly negatively charged silica surface. Moreover, the successful delivery and release of Hoechst from  $\text{Fe}_3\text{O}_4@\text{SiO}_2$



strengthen the possibility of using this magnetic controlled release system for antibiotics to kill the bacteria. Third, we fabricated a permalloy micro-pillar substrate which amplifies the magnetic forces. It is proved that with magnetic ratcheting array, more particles are drawn into the biofilm as observed from the cross section fluorescence. In addition, the amplified magnetic force can be used for mechanical disruption and the biofilm will be rearranged or even peeled off by the magnetic  $\text{Fe}_3\text{O}_4@SiO_2$  movement. This mechanical disruption could provide increased antibiotic efficacy for treatment of biofilm infections on implants such as catheters or prosthetics.

## 6.5. Experimental Section

*Materials:* All chemicals are used as purchased: Cetyltrimethylammonium bromide (CTAB, 95%), tetraorthoethylsilicate (TEOS, 98%), N,N'-dimethylformamide (99.8%),  $\beta$ -cyclodextrin ( $\geq 98\%$ ), Hoechst 33342 ( $\geq 97\%$ ), benzimidazole (98%), tetrabutylammonium iodide (98%), triethylamine ( $\geq 99\%$ ), toluene (99.8%) and rhodamine B isothiocyanate (RITC) were purchased from Sigma (St. Louis, MO). Chloromethyltrimethoxysilane (90%), diethylphosphatoethyltriethoxysilane (95%), and aminopropyltriethoxysilane (APTES) were purchased from Gelest (Morrisville, PA).  $\text{Fe}_3\text{O}_4$  (20 nm, 50 mg) was purchased from Ocean NanoTech (San Diego, CA). Chloroform (99%) was purchased from EMD Millipore (Billerica, MA).

*Synthesis of  $\text{Fe}_3\text{O}_4@SiO_2$ :* A solution of 9 mL water, 60  $\mu\text{L}$  2.0 M NaOH was heated to 70 °C and kept steady while stirring rapidly. Cetyltrimethylammonium bromide (CTAB, 20 mg) was dissolved in 1 mL water, followed by mixing with 500  $\mu\text{L}$  of iron

oxide in chloroform (2.5 mg/mL) Chloroform was boiled off the solution upon heating, and the oil-in-water microemulsion finally became clear brown. This mixture was sonicated for a few minutes to make sure there is no aggregation of iron oxide nanoparticles. The iron oxide solution was added to the base solution and the temperature was steady at 70 °C after 10 minutes. 100 mL of silica precursor tetraethyorthosilicate (TEOS, Aldrich, 98%) and 0.6 mL ethyl acetate were added in sequence into the solution and the mixture was stirred for 3 hours at 70 °C. When the reaction finished, the silica nanoparticles were washed and centrifuged with methanol or ethanol twice or three times. Iron oxide mesoporous silica nanoparticles synthesized with this method is uniformly monodispersed without necking among the nanoparticles. To get negatively charged particles, diethylphosphatoethyltriethoxysilane (10 µL) was mixed with 100 µL TEOS to co-condense the phosphonate groups with silica, and to make positively charged particles, APTES (20 µL) was mixed with the as-synthesized particle (100 mg) in anhydrous ethanol under N<sub>2</sub> and stirred overnight.

*Synthesis of 1-Methyl-1H-benzimidazole (MBI) Nanovalve:* Fe<sub>3</sub>O<sub>4</sub>@SiO<sub>2</sub> (10 mg) was washed and dispersed in anhydrous toluene, mixed with chloromethyltrimethoxysilane (3 µL) and refluxed for 12 hours under N<sub>2</sub>. The modified Fe<sub>3</sub>O<sub>4</sub>@SiO<sub>2</sub> was washed by toluene and dimethyformamide (DMF) and dispersed in 8 ml DMF. Tetrabutylammonium iodide (0.4 mg), benzimidazole (2.4 mg) and triethylamine (30 µL) were added into the solution and the mixture was stirred and heated up to 70 °C under N<sub>2</sub> for 24 hours. As-synthesized nanoparticles were

washed with DMF, methanol and water thoroughly.

*Label of Fe<sub>3</sub>O<sub>4</sub>@SiO<sub>2</sub>:* In a 2 mL centrifuge tube, RITC (1 mg) was mixed with APTES (2.4 μL) in 600μL anhydrous ethanol and rotated for 2 hours. Fe<sub>3</sub>O<sub>4</sub>@SiO<sub>2</sub> attached with MBI stalk (10 mg) was mixed with 30 μL of the RITC and refluxed in toluene for 12 hours. Labeled particles were washed with toluene and methanol.

*Surfactant template extraction:* RITC labeled Fe<sub>3</sub>O<sub>4</sub>@SiO<sub>2</sub> with MBI stalk (10 mg) was dispersed in 10 mL methanol, mixed with 16 mg ammonium nitrate and refluxed under N<sub>2</sub> for 30 minutes. The particles were collected by centrifugation and washed with methanol for twice.

*Loading and Release of Hoechst:* RITC labeled Fe<sub>3</sub>O<sub>4</sub>@SiO<sub>2</sub> (5 mg) with MBI stalk was dispersed in 1 mL Hoechst PBS solution (5 mM) and placed on the rotator for 24 hours. The cap β-CD (20 mg) was added into the loading solution and mixing for another 12 hours. The loaded particles were washed 5 times with PBS buffer and there is no Hoechst fluorescence observed in the supernatant under UV light. In order to completely release the Hoechst from Fe<sub>3</sub>O<sub>4</sub>@SiO<sub>2</sub>, 1 mg of the particles were dispersed in HCl aqueous solution (pH 1) for 12 hours and centrifuged down to measure the supernatant concentration through UV-Vis. The measured release capacity was 19 wt%. Release capacity (wt %) = ( W<sub>released Hoechst</sub> / W<sub>particle</sub> ) × 100 %.

*Physiochemical Characterization of Fe<sub>3</sub>O<sub>4</sub>@SiO<sub>2</sub>:* Transmission electron microscopy (TEM) images of Fe<sub>3</sub>O<sub>4</sub>@SiO<sub>2</sub> were obtained using a JEM1200-EX (JEOL) instrument (JEOL USA, Inc., Peabody, MA). UV-Vis spectra were collected with Carry 5000 UV-Vis-NIP spectrophotometer.

*Fe<sub>3</sub>O<sub>4</sub>@SiO<sub>2</sub> Dispersion in Biofilm:* The glass slide/polystyrene chip/permalloy micro-pillar substrate was immersed in bacterial medium and inoculated with ~1000 *Staphylococcus aureus* bacteria in a 12 well plate, followed by culturing at 37 °C for 3 days. Substrates were removed and placed in fresh well plate with warm bacterial media. RITC labeled Fe<sub>3</sub>O<sub>4</sub>@SiO<sub>2</sub> was added to the bacteria medium with various concentrations (10<sup>5</sup>/mL, 10<sup>6</sup>/mL, 10<sup>7</sup>/mL, and 10<sup>8</sup>/mL). A large 1” square rare earth magnet (Neodymium ferrite, N-52 grade, 0.5T surface field strength) was placed beneath the substrates to draw the particles onto the film for 1 minute. The biofilm was incubated at room temperature for another 1 hour, and then washed with sterile filtered PBS. Bacteria were stained with DAPI nuclear stain (10 µg/mL) and biofilm was stained with lectin binding protein 568. The substrate with biofilm and particles were washed with PBS again and imaging was done with fluorescence microscope.

## **6.6. Figures**

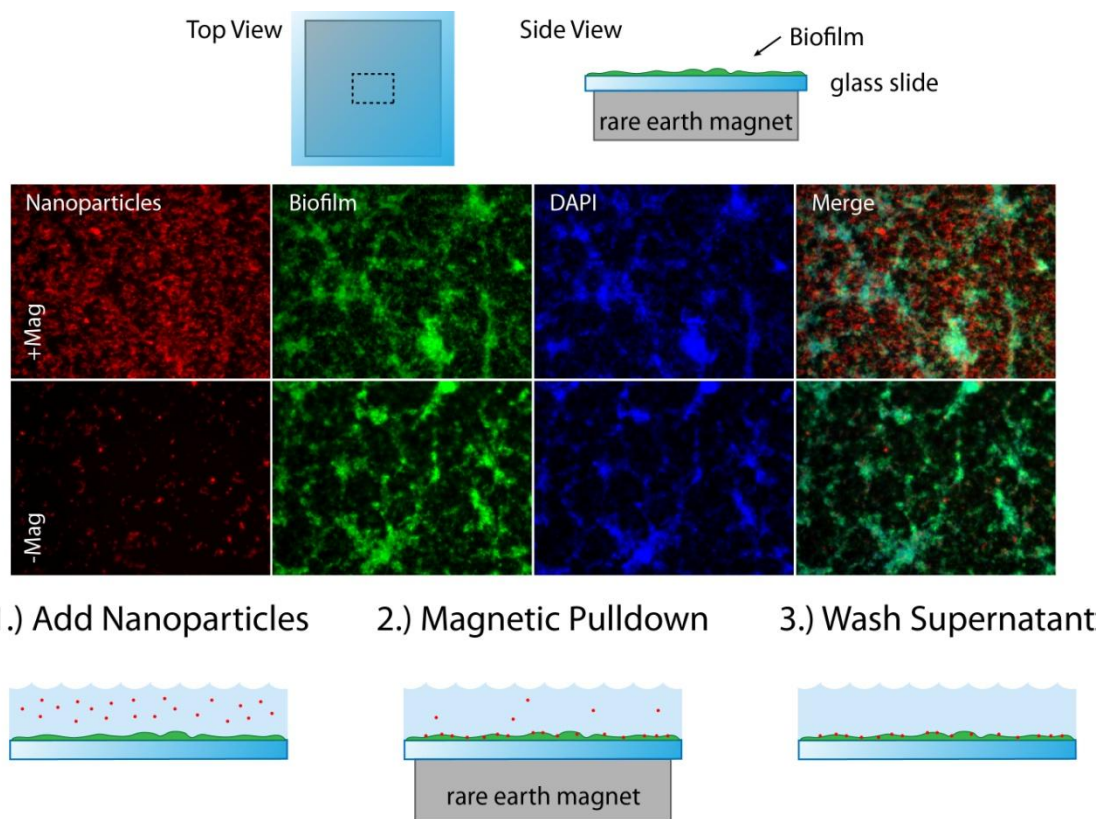


Figure 6.1.  $\text{Fe}_3\text{O}_4@\text{SiO}_2$  was dispersed on the biofilms grown on a glass slide. A rare earth magnet was placed underneath the glass slide of one group of biofilms to target the particles into biofilms, and the other group was not treated with magnet. Both groups of biofilms were washed with buffer to remove free particles on the biofilm.  $\text{Fe}_3\text{O}_4@\text{SiO}_2$  was labeled with red fluorescein and observed under fluorescence scope. The fluorescence from particle shows that the rare earth magnet effectively attract  $\text{Fe}_3\text{O}_4@\text{SiO}_2$  into the biofilm while there are only few particles left in the other group. The merged picture shows that empty space within the matrix is fulfilled with  $\text{Fe}_3\text{O}_4@\text{SiO}_2$  particles enforced by the magnet.

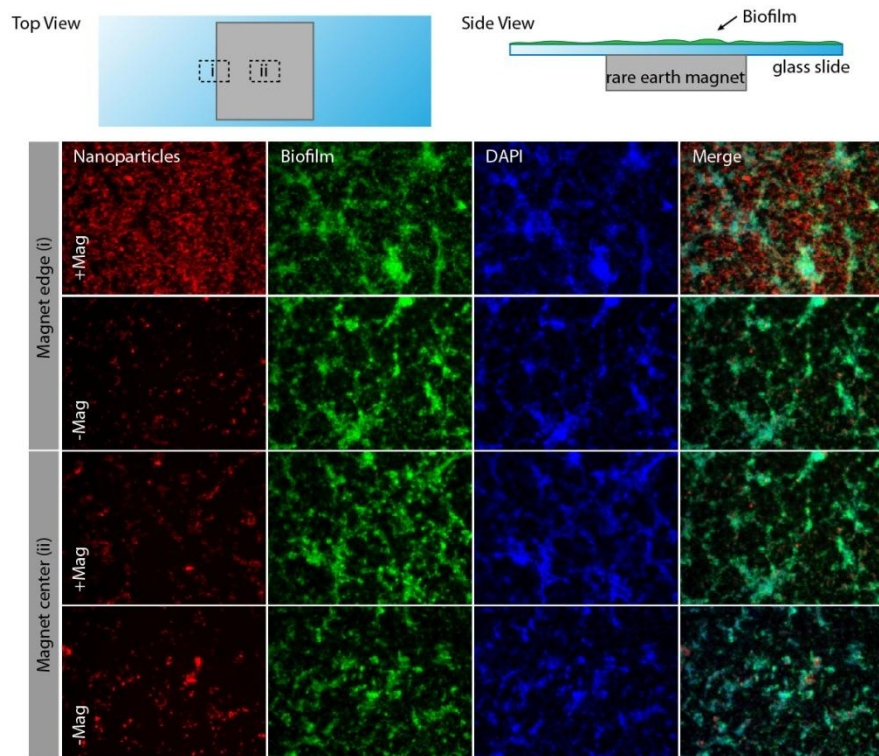


Figure 6.2.  $\text{Fe}_3\text{O}_4@\text{SiO}_2$  was dispersed on the biofilm, attracted by the rare earth magnet and washed by buffer as aforementioned. The particle distributions at two positions above the magnet on the biofilm were observed under fluorescence microscopy: at the edge of magnet and center of magnet. The particles at the edge of magnet were effectively attracted into the biofilm compared with no magnet. And the number of particles at the center magnet area left in biofilms was not higher than that without magnet.

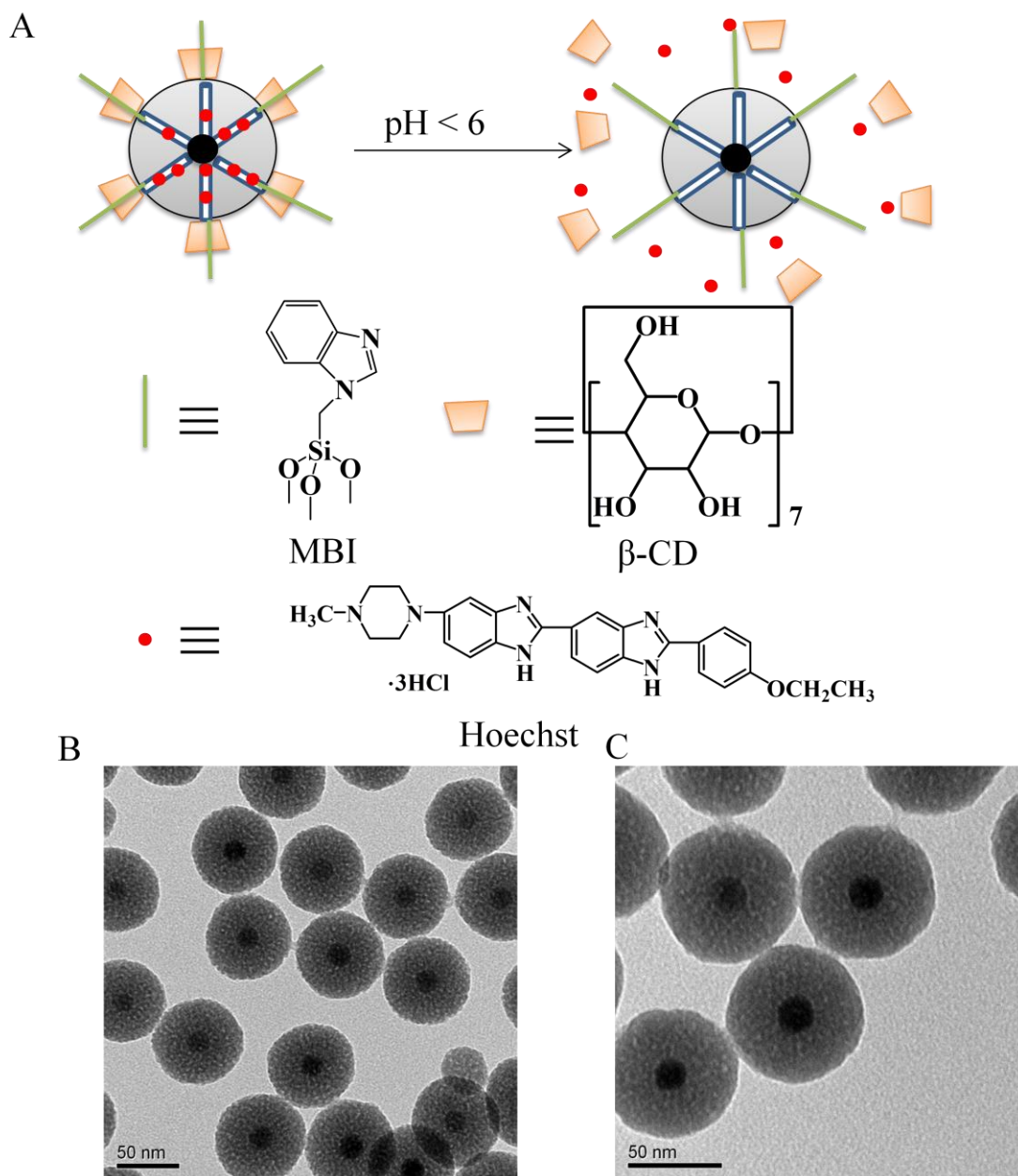


Figure 6.3. A. Structure of  $\text{Fe}_3\text{O}_4@\text{SiO}_2$  modified with pH-sensitive nanovalue and loaded with Hoechst dye. The nanovalue open at pH 6 and the caps dissociate from the stalk, release the cargo from inside mesopores. B. TEM of As-synthesized  $\text{Fe}_3\text{O}_4@\text{SiO}_2$  with uniform size distribution around 50 nm. C.  $\text{Fe}_3\text{O}_4@\text{SiO}_2$  attached with MBI nanovalue stalk preserved the integrity of nanoparticle and uniform distribution.

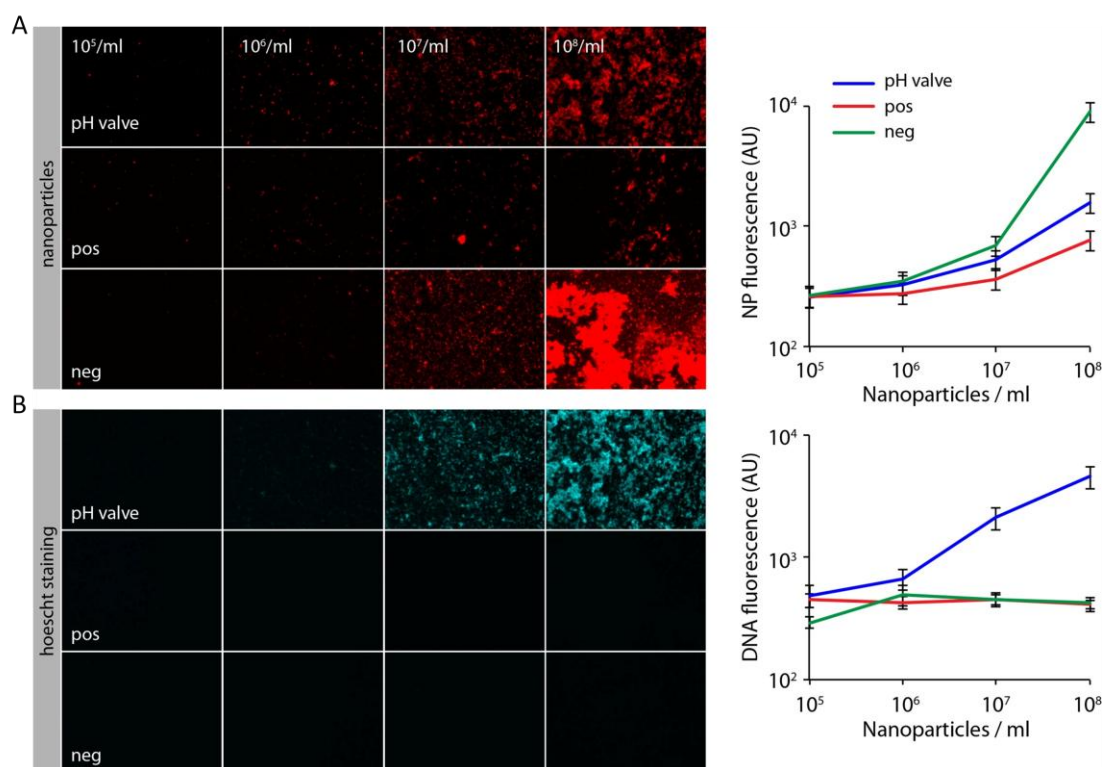


Figure 6.4. A. Distribution of positively charged  $\text{Fe}_3\text{O}_4@\text{SiO}_2$ , negatively charged  $\text{Fe}_3\text{O}_4@\text{SiO}_2$ , and pH-sensitive modified  $\text{Fe}_3\text{O}_4@\text{SiO}_2$  in biofilms with various particle concentrations ( $10^5/\text{mL}$ ,  $10^6/\text{mL}$ ,  $10^7/\text{mL}$ , and  $10^8/\text{mL}$ ). All the samples were washed after adding the particles. The  $\text{Fe}_3\text{O}_4@\text{SiO}_2$  fluorescence intensity was proportional to particle concentration. In terms of the number of particles left in biofilms, positively charged particles had smallest amount left, and negatively charged particles had largest amount, while those modified with pH-sensitive nanovalve was in the middle due to slight negative charge. B. The pH-sensitive nanovalve open in the acidic environment of biofilm as indicated by the fluorescence of Hoechst when particle concentration was above  $10^6/\text{mL}$ . The fluorescence intensity of DNA labeled by Hoechst was proportional to the concentration.



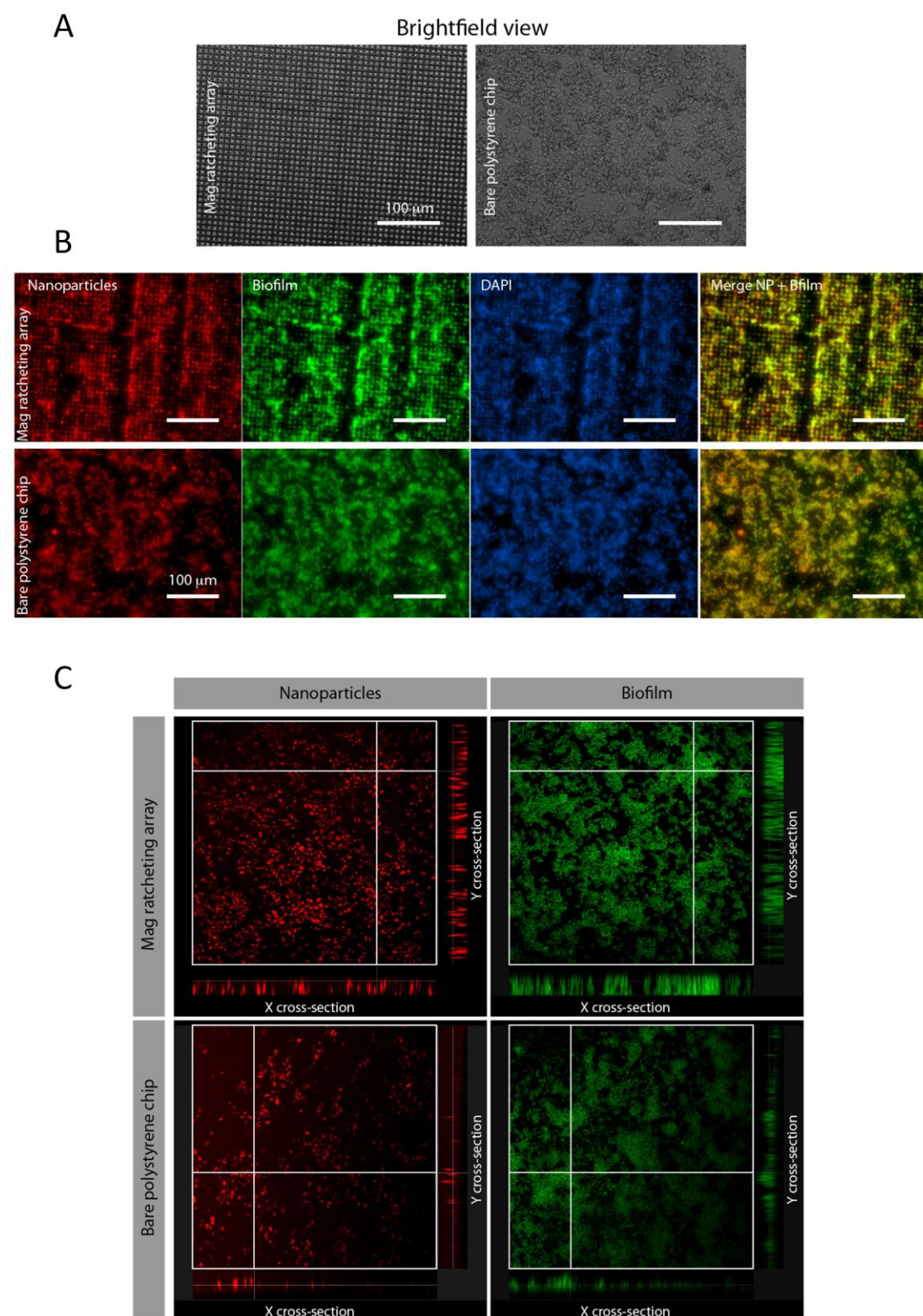


Figure 6.5. A. Bright-field view of the surface of permalloy micro-pillar substrate and polystyrene substrate. B. Red fluorescence is from  $\text{Fe}_3\text{O}_4@\text{SiO}_2$ , green fluorescence is

from biofilm and blue fluorescence is from the bacteria cell nucleus. The merging picture showed the co-localization of particles and biofilm. The upper panel is particles adding to biofilm on permalloy micro-pillar substrate, which attracted the  $\text{Fe}_3\text{O}_4@\text{SiO}_2$  along the micro-pillar pattern. And the lower panel is particles added to the biofilm on polystyrene substrate. C. Top view and XY cross section pictures by confocal microscope showed the more particles penetrated into the biofilm on magnetic ratcheting array than polystyrene substrate, because magnetic ratcheting array amplified the magnetic force to particles when rare earth magnet was placed underneath. The movement of magnetic particles also disrupts the biofilm and changed its pattern along the magnetic ratcheting array.

## 6.7. References

1. Forier, K.; Raemdonck, K.; De Smedt, S. C.; Demeester, J.; Coenye, T.; Braeckmans, K. Lipid and polymer nanoparticles for drug delivery to bacterial biofilms. *J Control Release* 2014, 190, 607-623.
2. Pace, J. L.; Rupp, M. E.; Finch, R. G. *Biofilms, infection, and antimicrobial therapy*. CRC Press: 2005.
3. Donlan, R. M. Biofilms: Microbial life on surfaces. *Emerg Infect Dis* 2002, 8, 881-890.
4. Smith, A. W. Biofilms and antibiotic therapy: Is there a role for combating bacterial resistance by the use of novel drug delivery systems? *Adv Drug Deliver Rev* 2005, 57, 1539-1550.
5. Martin, C.; Low, W. L.; Gupta, A.; Amin, M. C. I. M.; Radecka, I.; Britland, S. T.; Raj, P.; Kenward, K. Strategies for Antimicrobial Drug Delivery to Biofilm. *Curr Pharm Design* 2015, 21, 43-66.
6. Ehlert, N.; Badar, M.; Christel, A.; Lohmeier, S. J.; Luessenhop, T.; Stieve, M.; Lenarz, T.; Mueller, P. P.; Behrens, P. Mesoporous silica coatings for controlled release of the antibiotic ciprofloxacin from implants. *J Mater Chem* 2011, 21, 752-760.
7. Braem, A.; De Cremer, K.; Delattin, N.; De Brucker, K.; Neirinck, B.; Vandamme, K.; Martens, J. A.; Michiels, J.; Vleugels, J.; Cammue, B. P. A.; Thevissen, K. Novel anti-infective implant substrates: Controlled release of antibiofilm compounds from mesoporous silica-containing macroporous titanium. *Colloid Surface B* 2015, 126,

481-488.

8. Meng, H. A.; Xue, M.; Xia, T. A.; Zhao, Y. L.; Tamanoi, F.; Stoddart, J. F.; Zink, J. I.; Nel, A. E. Autonomous in Vitro Anticancer Drug Release from Mesoporous Silica Nanoparticles by pH-Sensitive Nanovalves. *J Am Chem Soc* 2010, 132, 12690-12697.
9. Jang, E. S.; Shin, J. H.; Ren, G.; Park, M. J.; Cheng, K.; Chen, X. Y.; Wu, J. C.; Sunwoo, J. B.; Cheng, Z. The manipulation of natural killer cells to target tumor sites using magnetic nanoparticles. *Biomaterials* 2012, 33, 5584-5592.
10. Tarn, D.; Xue, M.; Zink, J. I. pH-Responsive Dual Cargo Delivery from Mesoporous Silica Nanoparticles with a Metal-Latched Nanogate. *Inorg Chem* 2013, 52, 2044-2049.
11. Vroom, J. M.; De Grauw, K. J.; Gerritsen, H. C.; Bradshaw, D. J.; Marsh, P. D.; Watson, G. K.; Birmingham, J. J.; Allison, C. Depth penetration and detection of pH gradients in biofilms by two-photon excitation microscopy. *Appl Environ Microb* 1999, 65, 3502-3511.